Spectral Analysis of Laser-Driven, Layered X-Ray Backlighter Targets

Spektrale Analyse von lasergetriebenen, mehrlagigen Röntgenquellen
Zur Erlangung des Grades eines Doktors der Naturwissenschaften (Dr. rer. nat.)
Genehmigte Dissertation von Steffen Sander aus Darmstadt
Tag der Einreichung: 14. Februar 2022, Tag der Prüfung: 11. April 2022

1. Gutachten: Prof. Dr. Markus Roth
2. Gutachten: Prof. Dr. Wilfried Nörtershäuser
Darmstadt

TECHNISCHE UNIVERSITÄT DARMSTADT

Physics Department
Institut für Kernphysik
Laser- und Plasmaphysik

Spectral Analysis of Laser-Driven, Layered X-Ray Backlighter Targets
Spektrale Analyse von lasergetriebenen, mehrlagigen Röntgenquellen

Accepted doctoral thesis by Steffen Sander

1. Review: Prof. Dr. Markus Roth
2. Review: Prof. Dr. Wilfried Nörtershäuser

Date of submission: 14. Februar 2022
Date of thesis defense: 11. April 2022

Darmstadt

Bitte zitieren Sie dieses Dokument als:
URN: urn:nbn:de:tuda-tuprints-231227
URL: http://tuprints.ulb.tu-darmstadt.de/23122

Dieses Dokument wird bereitgestellt von tuprints,
E-Publishing-Service der TU Darmstadt
http://tuprints.ulb.tu-darmstadt.de
tuprints@ulb.tu-darmstadt.de

Erklärungen laut Promotionsordnung

§8 Abs. 1 lit. c PromO

Ich versichere hiermit, dass die elektronische Version meiner Dissertation mit der schriftlichen Version übereinstimmt.

§8 Abs. 1 lit. d PromO

Ich versichere hiermit, dass zu einem vorherigen Zeitpunkt noch keine Promotion versucht wurde. In diesem Fall sind nähere Angaben über Zeitpunkt, Hochschule, Dissertationsthema und Ergebnis dieses Versuchs mitzuteilen.

§9 Abs. 1 PromO

Ich versichere hiermit, dass die vorliegende Dissertation selbstständig und nur unter Verwendung der angegebenen Quellen verfasst wurde.

§9 Abs. 2 PromO

Die Arbeit hat bisher noch nicht zu Prüfungszwecken gedient.

Darmstadt, 14. Februar 2022

S. Sander

Zusammenfassung

Im Rahmen der vorliegenden Arbeit wird eine mehrschichtige Festkörperprobe, im folgenden Target genannt, als Röntgenquelle mit frontseitigen Modifikationen für eine optimale Laser-Target-Kopplung entwickelt. Die Erprobung dieses neuartigen Targets erfolgte am Lasersystem PHELIX am GSI Helmholtzzentrum für Schwerionenforschung GmbH in Darmstadt. Durchgeführt wurde diese Dissertation in der Arbeitsgruppe Laser- und Plasmaphysik des Instituts für Kernphysik der Technischen Universität Darmstadt.

Röntgenstrahlung ist ein unschätzbares Werkzeug für die Diagnose von Zuständen hoher Energiedichte (high energy density (HED)). Intensive Röntgenemission kann unter anderem durch die Bestrahlung von Targets mit hochenergetischen Kurzpulslasern mit Intensitäten über $10^{18}\,\mathrm{W\,cm^{-2}}$ erzeugt werden. Der resultierende Photonenfluss liegt in der Größenordnung von 10^{10} - $10^{11}\,\mathrm{ph\,J^{-1}}$ innerhalb einer engen spektralen Bandbreite. Zu den möglichen Anwendungen einer solchen Quelle gehören Radiographie und Streustudien an dichten Plasmen, um wichtige thermodynamische Größen wie Temperatur oder Dichte zu bestimmen. Hauptsächlich werden zwei Arten von lasergetriebenen Strahlungsquellen verwendet, die sich durch den Ionisierungsgrad des emittierenden Materials unterscheiden lassen. Bei schwacher Ionisierung ist das Spektrum dem der charakteristischen Röntgenstrahlung sehr ähnlich und wird als $K\alpha$ Strahlung bezeichnet. Mit zunehmender Ionisierung steigt auch die Energie der Röntgenstrahlung, was bei stark ionisierten Quellen zu thermischer Linienemission führt. Bei Photonenenergien jenseits von $10\,\mathrm{keV}$ kann die thermische Linienemission mit laserbetriebenen Quellen jedoch nicht effizient erzeugt werden, da für schwerere Elemente immer mehr Elektronen ionisiert werden müssen. Daher wird für die Emission hochenergetischer Linien eine lasergetriebene $K\alpha$ Quelle bevorzugt.

Im Rahmen dieser Arbeit wurde eine neuartige lasergetriebene $K\alpha$ Quelle entwickelt und erfolgreich getestet. Zwei Ziele wurden für diese Arbeit definiert. In erster Linie sollte eine Verbesserung des Energietransfers vom Laser zum Target erreicht werden, um die Anzahl der emittierten $K\alpha$ Photonen zu erhöhen. Zu diesem Zweck wurden frontseitige Modifikationen in Form von kegelförmigen Mikrostrukturen eingesetzt. Zweitens sollte eine thermische Isolierung des emittierenden Materials von der Wechselwirkungsregion des Laserplasmas erreicht werden. Dadurch wird ein sauberes Spektrum ohne zusätzliche thermische Linienemission erzeugt. Dies wurde durch den Aufbau des Targets aus zwei Schichten erreicht, nämlich die bereits erwähnte Modifikation auf der Vorderseite und eine Rückseitenschicht aus einem anderen Material für die Strahlungsemission.

Die Leistungsfähigkeit des entwickelten Targets wurde in einem Experiment mit dem Lasersystem PHELIX untersucht. Die beobachteten Spektren des Targets zeigten eine erfolgreiche Unterdrückung der thermischen Linienemission, was auf eine effektive thermische Isolierung hindeutet. Dieses Ergebnis wird durch eine spektroskopische Analyse der Linienform zur Bestimmung der mittleren Elektronentemperatur innerhalb des emittierenden Materials unterstützt. Es wurden Temperaturen im Bereich von 31 - $42\,\mathrm{eV}$ festgestellt, was auf eine schwache Ionisierung ohne Beteiligung der beiden innersten Elektronenschalen hinweist.

Die Gesamtzahl der $K\alpha$ Photonen wurde in der Größenordnung von $10^{10}\,\mathrm{ph\,J^{-1}}$ gemessen. Es wurde eine deutliche Zunahme der $K\alpha$ Photonen um den Faktor 2 - 3 aufgrund der Mikrostrukturen auf der

Vorderseite nachgewiesen. Die Quellgröße der Targets wurde auf 140 - $200\,\mu\mathrm{m}$ bestimmt. Die Ausrichtung der kegelförmigen Mikrostrukturen in Bezug auf den Laser wurde ebenfalls variiert und zeigte einen deutlichen Einfluss auf die $K\alpha$ Ausbeute und Quellengröße. Bei einer parallelen Ausrichtung wurde die höchste Photonendichte von $3.9 \times 10^{11}\,\mathrm{ph\,J^{-1}\,mm^{-2}}$ gemessen. Atomare Strahlungssimulationen wurden erfolgreich genutzt um die Elektronentemperatur in der Rückseitenschicht auf 31 - $42\,\mathrm{eV}$ zu bestimmen.

Ein weiteres einzigartiges Merkmal des mehrschichtigen Targets ist die Möglichkeit, die Größe der Quelle durch die Formung der Rückseitenschicht zu beeinflussen. Für kreisförmige Rückseitenschichten mit einem Durchmesser von $100\,\mu\mathrm{m}$ konnte die Quellgröße erfolgreich auf ebendieses Maß reduziert werden. Mit diese Targets konnte ebenfalls gezeigt werden, dass es möglich ist zwei räumlich getrennte, unterschiedliche Quellen mit einem Target zu erzeugen.

Abstract

In this thesis, a layered X-ray backlighter target with front side modifications for optimal laser target coupling is developed. The testing of this novel target design was done at the PHELIX laser system, located at the GSI Helmholtzzentrum für Schwerionenforschung GmbH in Darmstadt. This dissertation was carried out within the laser and plasma physics group of the Institut für Kernphysik at the Technische Universität Darmstadt.

X-ray radiation is an invaluable tool for the diagnosis of high energy density (HED) experiments. Strong X-ray emission can be generated, among other things, through the irradiation of solid-state targets by high-energy short-pulse lasers with intensities above $10^{18}\,\mathrm{W\,cm^{-2}}$. The resulting photon flux is in the order of 10^{10} - $10^{11}\,\mathrm{ph\,J^{-1}}$ within a narrow spectral bandwidth. The possible applications of such a source include radiography and scattering studies of dense plasmas in order to determine key thermodynamic variables like temperature or density. Two types of X-ray backlighter sources are commonly used, which can be differentiated by the degree of ionization of the emitting material. For weak ionization, the spectrum is very similar to the characteristic X-ray line emission and is called $K\alpha$ radiation. With rising ionization the energy of the X-rays increases as well, leading to thermal line emission for highly ionized sources. However, thermal line emission cannot be produced efficiently with laser driven backlighters for photon energies beyond $10\,\mathrm{keV}$, as more and more electrons have to be ionized from the heavier elements. Therefore, for high energy line emission, a laser-driven $K\alpha$ source is preferred.

Within the scope of this thesis, a novel laser driven $K\alpha$ source was developed and successfully tested. The goal was two-fold. Primarily, an improvement of the energy transfer from laser into target to increase the number of emitted $K\alpha$ photons should be achieved. In order to fulfil this goal, front side modifications in form of cone-like microstructures were used. Secondly, a thermal isolation of the emitting material from the laser plasma interaction region should be achieved. This produces a clean spectrum without any additional thermal line emission. This was done by constructing the target from two layers, namely the aforementioned front side modifications and a back side layer of different material for the X-ray emission.

The performance of the developed target was studied in an experiment with the PHELIX laser system. The observed spectra from the layered target displayed a successful suppression of thermal line emission, displaying the effective thermal isolation. This result is further supported with a spectroscopic line shape analysis to determine the mean electron temperature within the emitting material. Temperatures of 31 - $42\,\mathrm{eV}$ were found, indicating a weak ionization without involvement of the two inner-most electron shells.

The total number of $K\alpha$ photons were measured to be in the order of $10^{10}\,\mathrm{ph\,J^{-1}}$. A clear increase of factor 2 - 3 in $K\alpha$ photons due to the microstructures on the front side was demonstrated. The source size of the targets were determined to be 140 - $200\,\mu\mathrm{m}$. The orientation of the cone-like microstructures with respect to the laser were varied as well and displayed a clear influence on the $K\alpha$ yield and source size. For a parallel alignment, the highest photon flux of $3.9 \times 10^{11}\,\mathrm{ph\,J^{-1}\,mm^{-2}}$ was found. Atomic radiative simulations were successfully used to determine the electron temperature in the backside layer to 31 - $42\,\mathrm{eV}$.

Another unique feature of the layered target design is the possibility to influence the source size through the shape of the back side layer. The source size was successfully reduced to $100\,\mu\mathrm{m}$ using a circular shaped back side layers of the same dimensions. With these targets it was also possible to demonstrate the possibility of generating two spatially separated, distinct sources from one target.

Contents

Abbreviations **xv**

1 Introduction **1**
1.1 Thesis structure . . . 3

2 Laser matter interaction **5**
2.1 Relativistic electron motion in a laser field . . . 5
2.2 Laser propagation in a plasma . . . 7
2.3 Absorption mechanisms . . . 8
2.4 Electron transport . . . 10
2.4.1 Charge neutrality . . . 10
2.4.2 Stopping power . . . 11
2.4.3 Refluxing . . . 12

3 X-ray radiation **13**
3.1 X-ray generation . . . 13
3.1.1 Characteristic X-ray radiation . . . 14
3.1.2 Line width . . . 16
3.1.3 X-ray scattering and absorption . . . 19
3.1.4 Thermal line emission . . . 21
3.1.5 Conversion efficiencies . . . 22
3.2 Atomic radiative simulations . . . 23
3.2.1 Collisional-radiative model . . . 23
3.2.2 Spectrum generation . . . 26
3.3 X-ray spectrometer . . . 27
3.3.1 Crystals . . . 28
3.3.2 Spectrometer layouts . . . 31
3.3.3 X-ray detection . . . 35

4 Target design and fabrication **39**
4.1 Overview of X-ray backlighter concepts . . . 39
4.1.1 Layered targets . . . 40
4.2 Fabrication . . . 41
4.3 Overview of finished targets . . . 43

5 Experimental methods **47**
5.1 Experimental setup . . . 47
5.2 The PHELIX laser system . . . 49

5.3 X-ray spectrometers . . . 50
5.3.1 HOPG spectrometers . . . 52
5.3.2 Ge spectrometers . . . 53
5.3.3 Image plate calibration . . . 54

6 Experimental results **59**
6.1 Spectral emissivity of layered targets . . . 59
6.1.1 Calibration of the spectrometers . . . 59
6.1.2 Results from pure Cu foil target . . . 60
6.1.3 Results from flat layered target . . . 62
6.1.4 Results from microstructured layered target . . . 64
6.2 Target performance . . . 65
6.2.1 Source size measurements . . . 66
6.2.2 Conversion efficiencies . . . 67
6.2.3 Influence of ASE contrast . . . 69
6.2.4 Source size limited targets . . . 70
6.3 Atomic radiative simulations . . . 73
6.3.1 Set-up of the simulation . . . 73
6.3.2 Temperature of the $K\alpha$ source . . . 75

7 Conclusion and Outlook **83**
7.1 Outlook . . . 84

List of Figures

2.1 Movement of an electron in an inhomogeneous, relativistic laser pulse. 7
2.2 Stopping power for Cu. 11

3.1 Cross sections for electron-ion interactions in Cu. 15
3.2 Principle of characteristic $K\alpha$ emission and level scheme of bound levels in Cu 16
3.3 Comparison of different peak profiles with the same FWHM. 18
3.4 Attenuation of X-rays in $BaFBr_{0.85}I_{0.15}$ 20
3.5 Mean free path of X-ray photons in copper (Cu) for various temperatures. 20
3.6 Principle schema for satellite line emission and dielectronic recombination. 21
3.7 Crystal planes of a diamond cubic lattice. 28
3.8 Schematic of the Bragg diffraction. 29
3.9 Rocking curve for three differently shaped crystals. 30
3.10 Schematic of the reflection principle for a mosaic crystal. 31
3.11 Layout of a flat crystal spectrometer with the resulting spectral range and resolution over F. 32
3.12 Layout of a *von Hamos* spectrometer. 33
3.13 Schematic of a *Johann* type spectrometer layout with two additional cases of different source positions. 34
3.14 Schematic of an imaging spectrometer layout. The spectral dispersion follows the principle of a *Johann* type spectrometer. 35
3.15 Schematic of an IP and the PSL process. 37

4.1 Schematic of the thermal evaporation process. 42
4.2 SEM image of Si microstructures and relevant sizes of the microstructured layered target. . 44
4.3 Target schematic front and back with image of final target. 45
4.4 SEM image of tilted needles and microscope image of Cu dots. 45

5.1 Overview over the experimental setup. 48
5.2 Recorded image of the laser focus. 49
5.3 ASE contrast of the PHELIX laser for three different settings of the uOPA. 51
5.4 Schematic of the IP housing and debris shield. 51
5.5 Estimated PSF for the employed spectrometers. 53
5.6 Fading characteristic of an IP. 55
5.7 Response functions of the employed IPs. 57

6.1 Spectrum calibration process. 60
6.2 Spectral emissivity of the pure Cu target. 61
6.3 Spectral emissivity of the flat layered target. 62
6.4 Simple refluxing model to estimate the energy loss in the Si layer of the target. 64
6.5 Spectral emissivity of the $15°$ microstructured layered target. 65

6.6 Source size for all layered target types. 66
6.7 CE over target type for all spectrometer. 67
6.8 CE normalised to source size for the various layered targets. 69
6.9 CE for varying levels of ASE contrast of the PHELIX laser. 70
6.10 Source sizes for varying levels of ASE contrast of the PHELIX laser. 71
6.11 Measured CE for the dot targets. 72
6.12 Spatially resolved spectrum of a dot target together with the horizontal summation of the $K\alpha_2$ and $K\alpha_1$ peaks. 72
6.13 Influence of layer thickness and hot electron fraction on the resulting $K\alpha$ spectrum. 74
6.14 Effect of instrumental PSF on simulated spectrum. 75
6.15 Comparison of spectra generated with FLYCHK and SCFLY together with experimental spectrum. 76
6.16 Spectral emission and position of dominant K-shell emission with varying bulk electron temperature. 77
6.17 Values of the merit function over bulk electron temperature and comparison of best fitting simulated spectrum to experimental measurement. 77
6.18 Relative ion population and spectral shape of a composite model. 78
6.19 Relative ion population and spectral shape of a narrower $K\alpha$ line. 79
6.20 Bulk electron temperature for the investigated target types. 80
6.21 Bulk electron temperatures for limited Cu volume targets. 81
6.22 Bulk electron temperature over amplified spontaneous emission (ASE) contrast for three target types. 82

List of Tables

3.1 Rate coefficients of the atomic processes relevant to an atomic level change. 24

5.1 Overview of spectral characteristics of the used spectrometer setups. 50
5.2 Geometric parameters of the used Ge crystals. 54
5.3 Values of the used fading function. 56

Abbreviations

ASE	amplified spontaneous emission
BAS	biological analysis system
BAS SR	biological analysis system super resolution
BAS TR	biological analysis system tritium
BBO	barium borate
bcc	body-centered cubic
CCD	charge-coupled device
CE	conversion efficiency
CPA	chirped pulse amplification
CR	collisional-radiative
CSDA	continuous slowing down approximation
DHS	Dirac-Hartree-Slater
EMP	electromagnetic pulse
FAIR	Facility for Antiproton and Ion Research
fcc	face-centered cubic
FLT	flat layered target
FWHM	full width at half maximum
HED	high energy density
HOPG	highly oriented pyrolytic graphite
ICF	inertial confinement fusion
IP	image plate
IPD	ionization potential depression
KAP	potassium acid phthalate
LIPSS	laser induced periodic surface structures
LTE	local thermal equilibrium
MCP	multi-channel plate
MLT	microstructured layered target
nhelix	Nanosecond High Energy Laser for Heavy Ion Experiments

OAP	off-axis parabola
PET	polyethylene terephthalate
PHELIX	Petawatt High Energy Laser for Heavy Ion Experiments
PIC	particle-in-cell
PMT	photo multiplier tube
PSF	point spread function
PSL	photo-stimulated luminescence
RCF	radiochromatic film
SEM	scanning electron microscope
SRXRS	stimulated resonant electronic X-ray Raman scattering
STA	super-configuration transition array
uOPA	ultrafast optical parametric amplifier
UTA	unresolved transition array
XANES	X-ray absorption near-edge spectroscopy
XES	X-ray emission spectroscopy
XFEL	X-ray free electron laser
XRTS	X-ray Thomson scattering

1 Introduction

X-ray radiation has been and remains a vital diagnostic tool in many fields of research since its discovery in 1895 by C. W. Röntgen [Rön95; Rön96; Rön97]. One such field is the investigation of high energy density (HED) physics, that studies radiation and matter at energy densities in excess of about $10^5\,\mathrm{J\,cm^{-3}}$ [Dra18]. This research includes laboratory astrophysics, such as the measurement of equations of state relevant for planetary and stellar interiors, as well as experiments regarding inertial confinement fusion (ICF).

HED states can be achieved through several experimental schemes. Small volumes, with dimensions of a few $\mu\mathrm{m}^3$, can be heated through the interaction of a solid-state target with high-power, short-pulse lasers [Dra18]. Large volumes of a few mm^3 can be heated with intensive ion beams that penetrate much deeper into the target [For+96]. This so-called volumetric heating will, for example, be possible at the Facility for Antiproton and Ion Research (FAIR) currently being build in Darmstadt, Germany [Sel20].

All experiments within this field have in common, that the sample has a high opacity, in particular in the visible regime, and a strong background of self-emitted radiation. The tool of choice to measure relevant quantities such as temperature, density and ionisation state remains the X-ray radiation. Many different diagnostics on the basis of X-ray radiation have been developed. These include the spectral analysis of the self-emission (X-ray emission spectroscopy (XES)) [Don+04], the direct radiography of the probe [Le +10; Mor+14], the X-ray absorption near-edge spectroscopy (XANES) [Dor+15a], the Talbot-Lau X-ray interferometry [Bou+20], stimulated resonant electronic X-ray Raman scattering (SRXRS) [Wen+13] and X-ray Thomson scattering (XRTS) [GR09]. With the exception of the XES, all of these diagnostics rely on powerful X-ray sources that provide the necessary photon flux to probe the HED sample.

X-ray free electron lasers (XFELs) can provide large X-ray photon fluxes in short pulses, producing an ideal source for many of the mentioned diagnostics. However, only a few XFELs are available around the world and access is limited. The generation of X-ray radiation with high-power lasers is another approach to produce this emission. The high-energy short-pulse laser is focused on a solid-state target. Electrons are

[Rön95] Röntgen (1895), *Über eine neue Art von Strahlen - Vorläufige Mittheilung*.
[Rön96] Röntgen (1896), *Über eine neue Art von Strahlen - Fortsetzung*.
[Rön97] Röntgen (1897), *Weitere Beobachtungen über die Eigenschaften der X-Strahlen*.
[Dra18] Drake (2018), *High-Energy-Density Physics*.
[For+96] Fortov et al. (1996), "Intense shock waves in hot dense matter generated by high-power light ion beams".
[Sel20] Selyuzhenkov (2020), "Status of the FAIR facility in Darmstadt".
[Don+04] Dong et al. (2004), "Electronic structure of nanostructured ZnO from x-ray absorption and emission spectroscopy and the local density approximation".
[Le +10] Le Pape et al. (2010), "X-ray radiography and scattering diagnosis of dense shock-compressed matter".
[Mor+14] Morace et al. (2014), "Development of x-ray radiography for high energy density physics".
[Dor+15a] Dorchies et al. (2015), "X-ray absorption K edge as a diagnostic of the electronic temperature in warm dense aluminum".
[Bou+20] Bouffetier et al. (2020), "Proof-of-concept Talbot–Lau x-ray interferometry with a high-intensity, high-repetition-rate, laser-driven K-alpha source".
[Wen+13] Weninger et al. (2013), "Stimulated Electronic X-Ray Raman Scattering".
[GR09] Glenzer and Redmer (2009), "X-ray Thomson scattering in high energy density plasmas".

accelerated during this interaction, causing the emission of bremsstrahlung and characteristic radiation. The target is also transferred to a plasma state. Depending on the mean ionisation of the target, this radiation can have multiple distinct energies. For weak ionisation, involving only the outer shells of the atom, the energy is close to the classical characteristic radiation of a singly, K-shell ionised atom and called $K\alpha$ radiation. For highly-ionised atoms, the atomic charge is less screened and the released energy increases. This is typically referred to as thermal line emission or depending on the mean ionisation as Heα or Lyα radiation.

In the past the majority of laser-driven X-ray backlighters have been relying on this thermal line emission, specifically the Heα line emission. These sources are however limited with respect to the X-ray photon energy to $\lesssim 10\,\mathrm{keV}$ [Par+06; GR09]. Therefore, the interest in backlighter sources specifically optimised for $K\alpha$ emission has increased over the last two decades. One requirement for efficient $K\alpha$ production is a relativistic intensity ($\geq 10^{18}\,\mathrm{W\,cm^{-2}}$) of the laser, which is routinely reached by multiple PW laser systems around the world. The interest is motivated mainly due to the following characteristics of a $K\alpha$ backlighter. Primarily, a near independence of the conversion efficiency (CE) from laser light to X-ray photon flux for different target materials, and therefore $K\alpha$ energies, is observed [Par+06; Nil+08]. This allows for powerful line emission with energies of a few $10\,\mathrm{keV}$. Furthermore, the peak shape is much more favourable for scattering diagnostics, such as collective XRTS, because no emission with energies below the main line is possible [GR09]. This is in contrast to thermal line emission, that has typically a much wider bandwidth including the emission of multiple ionisation states. Lastly, the observed pulse length of the $K\alpha$ emission is typically much shorter due to the pulse length of the driving laser, which is in the sub-ps to ps range [Ye +13].

One key aspect of a high CE backlighter target is the amount of laser energy that is transferred into the target. Studies have investigated various concepts to increase this laser target coupling, including pre-pulses [Gir16], foam and aerogel targets [Pér+14; WLC18], nanostructured velvet targets [Kul+00; Ye +13; Hab+16; Sam+18] and microstructured targets [Kli+11; Jia+14; Bla+17; Ebe+20]. In particular, the latter show great promise with respect to multi-$100\,\mathrm{J}$ laser pulses [Ebe+20]. The microstructures, that are manufactured from silicon (Si), have a cone-like shape with a base width and cone height of a few $\mu\mathrm{m}$ and can be produced homogeneously over a large surface [Ebe+17; Ebe+21]. So far, these microstructures

[Par+06] Park et al. (2006), "High-energy Kα radiography using high-intensity, short-pulse lasers".
[Nil+08] Nilson et al. (2008), "High-intensity laser-plasma interactions in the refluxing limit".
[Ye +13] Ye Tian et al. (2013), "Experimental study of K-shell X-ray emission generated from nanowire target irradiated by relativistic laser pulses".
[Gir16] Girard (2016), "Review of laser produced multi-keV X-ray sources from metallic foils, cylinders with liner, and low density aerogels".
[Pér+14] Pérez et al. (2014), "Bright x-ray sources from laser irradiation of foams with high concentration of Ti".
[WLC18] Wang et al. (2018), "High conversion efficiency and small spot size of Kα X-ray generated from nano-foam Cu targets irradiated by femtosecond laser pulses".
[Kul+00] Kulcsár et al. (2000), "Intense Picosecond X-Ray Pulses from Laser Plasmas by Use of Nanostructured "Velvet" Targets".
[Hab+16] Habara et al. (2016), "Efficient energy absorption of intense ps-laser pulse into nanowire target".
[Sam+18] Samsonova et al. (2018), "Hard X-ray Generation from ZnO Nanowire Targets in a Non-Relativistic Regime of Laser-Solid Interactions".
[Kli+11] Klimo et al. (2011), "Short pulse laser interaction with micro-structured targets: Simulations of laser absorption and ion acceleration".
[Jia+14] Jiang et al. (2014), "Effects of front-surface target structures on properties of relativistic laser-plasma electrons".
[Bla+17] Blanco et al. (2017), "Table-top laser-based proton acceleration in nanostructured targets".
[Ebe+20] Ebert et al. (2020), "Enhanced brightness of a laser-driven x-ray and particle source by microstructured surfaces of silicon targets".
[Ebe+17] Ebert et al. (2017), "Laser-induced microstructures on silicon for laser-driven acceleration experiments".
[Ebe+21] Ebert et al. (2021), "Targets with cone-shaped microstructures from various materials for enhanced high-intensity laser-matter interaction".

have been used with a high amplified spontaneous emission (ASE) contrast of the laser ($>10^{11}$). Such a high contrast decreases the intensity of the ASE plateau below the damaging threshold and the formation of a pre-plasma is suppressed [Wag+14; Ebe+20]. However, many of the kJ laser systems around the world have an ASE contrast of $\leq 10^{10}$ [DNH14; Din+21; Dor+15b]. Therefore, the survivability of these microstructures with lower ASE contrasts needs to be investigated.

In this work, a novel laser-driven X-ray source for $K\alpha$ emission is developed. It is investigated if a layered target can combine the positive emission characteristics of $K\alpha$ sources with the increased laser target coupling of front side microstructures. In addition, thermal isolation of the X-ray generation from the laser target interaction is sought in order to provide a clean spectrum for applications. The survivability of the front side microstructures for varying levels of ASE contrast is examined.

1.1 Thesis structure

In chapter 2, the general interaction of a high power laser with a solid state target is discussed. In particular the electron acceleration for relativistic intensities and the transport of these electrons into the target are the focus of this chapter.

The following chapter 3 discusses the basics of X-ray radiation. In section 3.1, the fundamental understanding of X-ray emission and the interaction of this radiation with matter is explained. The following section 3.2 briefly describes the models of atomic radiative codes that can be used to calculate emission spectra of plasmas. The chapter concludes with an overview over X-ray diagnostic methods.

The microstructured layered target (MLT) developed in this thesis is introduced in chapter 4. In the first section, the design process is described. The following sections explain the fabrication process and the characterisation of the finished targets.

The last two chapters present the experimental setup and findings of the conducted experiment at the PHELIX laser. The spectrometers used to diagnose the X-ray emission are presented in section 5.3. The spectra, measured with these spectrometers are analysed with respect to general spectral shape in section 6.1. A quantitative analysis of the observed radiation is done in section 6.2. The analysis is complemented with a derivation of bulk electron temperatures through atomic radiative simulations in section 6.3.

In chapter 7, the findings are summarised and an outlook on future possibilities with the MLTs is given.

[Wag+14] Wagner et al. (2014), “Pre-plasma formation in experiments using petawatt lasers”.
[DNH14] Danson et al. (2014), “Pulse fidelity in ultra-high-power (petawatt class) laser systems”.
[Din+21] Ding et al. (2021), “Universal nanosecond range pulse contrast measurement for a kJ-class petawatt laser”.
[Dor+15b] Dorrer et al. (2015), “OPCPA front end and contrast optimization for the OMEGA EP kilojoule, picosecond laser”.

2 Laser matter interaction

This chapter explains the fundamentals of how a high-power, short-pulse laser interacts with a solid target. The foundation of these lasers is the chirped pulse amplification (CPA), which was introduced by D. Strickland and G. Mourou in 1985 [SM85] and is the rational of the 2018 Nobel Prize in Physics. With CPA, it is possible to generate powerful laser pulses of sub-ps duration and with energies of a few $100\,\mathrm{J}$. In combination with a tight focus to a few $\mu\mathrm{m}$, *relativistic* intensities above $10^{18}\,\mathrm{W\,cm^{-2}}$ are easily reached. These intensities show great promise for the production of efficient $K\alpha$ emission.

When a solid-state target is irradiated with a laser beam of such intensity, ionisation of the irradiated material and the formation of a plasma occurs. This initial plasma formation and the propagation of the laser pulse within the plasma are discussed in Sec. 2.2. In order to understand this interaction, the movement of a single electron within the strong fields of a laser is considered in section 2.1. The various processes of generating energetic electrons are covered in section 2.3. The transport of these electrons through the target are the topic of the last section 2.4.

2.1 Relativistic electron motion in a laser field

If one considers a free electron in the electric field of a laser, a motion following the electric field oscillation can be observed. This motion is due to the Lorentz force acting on the electron. Taking, for simplicity, a linearly polarised, electromagnetic wave propagating in z-direction and assuming that it is uniform in space and only slowly varying in time, the exerted force on the electron of mass m_e, velocity $\vec{v}$ and charge e is

$$\frac{\mathrm{d}\vec{p}}{\mathrm{d}t} = -e\left(\vec{E} + \vec{v}\times\vec{B}\right) = -e\left[E + \vec{v}\times\left(\frac{1}{c}\vec{e}_z\times\vec{E}\right]\right) \quad \text{with} \tag{2.1}$$

$$\vec{p} \quad = \gamma m_\mathrm{e}\vec{v}, \quad \gamma = \frac{1}{\sqrt{1-\frac{v^2}{c^2}}} \quad \text{the relativistic factor} \quad \text{and} \tag{2.2}$$

$$c\vec{B} = \vec{e}_z \times \vec{E} \tag{2.3}$$

following Maxwells third equation $\vec{\nabla}\times\vec{E} = -\partial\vec{B}/\partial t$. The varying electric field $\vec{E} = \vec{E}_0\cos(\omega_\mathrm{L}t)$ is described by the amplitude $\vec{E}_0$ and frequency ω_L of the laser. The magnetic field can be neglected, if $v \ll c$ holds. The resulting velocity of the oscillating electron is then calculated using

$$v_\text{osc.} = \frac{eE_0}{m_\mathrm{e}\omega_L}, \tag{2.4}$$

called the *quiver velocity*.

[SM85] Strickland and Mourou (1985), "Compression of amplified chirped optical pulses".

The assumption of $v \ll c$ is invalidated at the very least for intensities $I_0 > 1.37 \times 10^{18}\,\mathrm{W\,cm^{-2}}$ of the laser [Gib05]. This limit of the non-relativistic treatment of the electron movement is best shown with the *electric field amplitude* a_0, which is derived by normalizing the momentum of the oscillating electron $p_{\text{osc.}}$ with the factor $m_\mathrm{e}c$. From equation (2.4) follows, that

$$a_0 \equiv \frac{p_{\text{osc.}}}{m_\mathrm{e}c} = \frac{eE_0}{m_\mathrm{e}\omega_L c} = \sqrt{\frac{I_0\left[\mathrm{W\,cm^{-2}}\right] \cdot \lambda_\mathrm{L}^2\left[\mu\mathrm{m}^2\right]}{1.37 \times 10^{18}\,\mathrm{W\,cm^{-2}\,\mu m^2}}} \tag{2.5}$$

with λ_L being the wavelength of the laser. The condition $v \ll c$ then translates with (2.5) into $a_0 \ll 1$. For $a_0 \geq 1$, the quiver velocity approaches c and the laser pulse itself is called relativistic. For a linearly polarised wave, the relation

$$\bar{\gamma} = \sqrt{1 + \frac{a_0^2}{2}} \tag{2.6}$$

holds when averaging over one oscillation of the laser.

In this work, the laser pulses reach intensities of a few $10^{20}\,\mathrm{W\,cm^{-2}}$, resulting in $a_0 \gtrsim 9$. The magnetic field can thus not be neglected in (2.1). As a result, an additional force $F = qvB \propto E \cdot E/c \propto a_0^2$ acts on the electron, pushing it in forward direction of the laser. The velocity of this drift is

$$v_{\mathrm{D},z} = \frac{a_0^2}{4 + a_0^2}c. \tag{2.7}$$

For a derivation of (2.7) in case of a relativistic laser pulse, the reader is referred to [Gib05].

However, the velocities $v_{\text{osc.}}$ and $v_{\mathrm{D},z}$ only appear as long as the electron is influenced by the electromagnetic field. After the interaction, the electron is again at rest and while the electron might have changed its position due to $v_{\mathrm{D},z}$, no energy has been transferred. This fact is known as the Lawson-Woodward theorem [ESK95].

In order to circumvent this limitation, one need to consider a more complex electromagnetic wave. Luckily, any high-power laser pulse invalidates the above assumption of a uniform, slowly varying plane wave. The short pulse length in the regime of a few hundred fs to a few ten ps and the tight focus down to a few $\mu\mathrm{m}$ results in strong temporal and spatial gradients. This inhomogeneous electric field gives rise to a force that pushes the electrons away from the region of highest intensity, the *ponderomotive force* $\vec{F}_\mathrm{P}$. Assuming again a non-relativistic pulse and averaging over one oscillation cycle yields

$$\vec{F}_\mathrm{P} = -\frac{e^2}{4m_\mathrm{e}\omega_\mathrm{L}^2}\vec{\nabla}\left(\vec{E}\cdot\vec{E}\right) \tag{2.8}$$

To illustrate the implications of this, consider the following example. If the spatial profiler of a laser pulse is Gaussian shaped, there is a gradient perpendicular to the laser axis. Thus, the electron will be pushed away from this axis, i.e. out of the focus of the laser.

Going back to laser pulses with $a_0 \geq 1$, the fully relativistic ponderomotive force has been derived by Bauer *et al.* [BMS95]

$$\vec{F}_\mathrm{p} = -\frac{c^2}{\gamma}\left(\vec{\nabla}m_\mathrm{eff} + \frac{\gamma - 1}{v_0^2}\left(\vec{v}_0 \cdot \vec{\nabla}m_\mathrm{eff}\right)\vec{v}_0\right), \tag{2.9}$$

[Gib05] Gibbon (2005), *Short Pulse Laser Interactions with Matter*.
[ESK95] Esarey et al. (1995), "Laser acceleration of electrons in vacuum".
[BMS95] Bauer et al. (1995), "Relativistic Ponderomotive Force, Uphill Acceleration, and Transition to Chaos".

with $m_{\text{eff}} = \sqrt{1 + a_0/2}$ the space- and time-dependent effective mass. This now leads to a more complete picture, as is displayed in Fig. 2.1. The electron oscillates due to the changing electric field, experiences a drift in forward direction due to the magnetic field and is pushed away from the region of highest intensity due to the ponderomotive force.

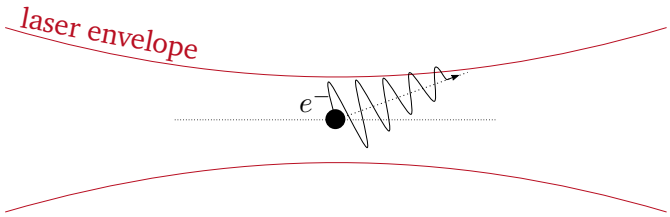

Figure 2.1: Movement of an electron in an inhomogeneous, relativistic laser pulse. Reproduced after [Gib05].

2.2 Laser propagation in a plasma

While the discussion in the previous section does provide some basic understanding, the more relevant case for this work is the interaction of the laser with an initially solid target. Starting from intensities of $I \approx 10^9\,\mathrm{W\,cm^{-2}}$, a laser will create a plasma on the surface of such a solid target. Multiple mechanisms have been proposed to describe this initial ionisation. These include avalanche ionisation for 10^9 - $10^{12}\,\mathrm{W\,cm^{-2}}$ and multiphoton ionisation for intensities above $10^{12}\,\mathrm{W\,cm^{-2}}$ [Boy20]. In particular, in non-metallic materials, where no highly mobile electrons are available, the question of the first electron is still topic of much debate. Material defects leading to unbound electrons could be a source for this first electron. Nevertheless, the formation of a plasma is always observed. This plasma expands into the vacuum in front of the target with the speed of sound

$$c_\mathrm{s} = \sqrt{k_\mathrm{B} \frac{Z_\mathrm{i} T_\mathrm{e} + T_\mathrm{i}}{m_\mathrm{i}}}, \tag{2.10}$$

k_B the Boltzmann constant, $T_{\mathrm{e,\,i}}$ the electron and ion temperature and m_i the mass of the ion. This produces a density gradient on the target surface.

A plasma is defined as *a quasineutral gas of charged and neutral particles which exhibits collective behaviour* [Che16]. The charged particles in the plasma interact with the laser, similar to the discussion in the previous section. The heavier ions can be considered a static background, as the quiver velocity $v_{\text{osc.}}$ of the particles scales with $\propto 1/m$ (see equation (2.4)). The movement of the electrons relative to this static ion background creates an electric field that forces the electrons to oscillate. The frequency of this oscillation is

$$\omega_{\mathrm{p,e}} = \sqrt{\frac{n_\mathrm{e} e^2}{\gamma \epsilon_0 m_\mathrm{e}}}, \tag{2.11}$$

the so-called *electron plasma frequency*.

Comparing the laser frequency ω_L to $\omega_{\mathrm{p,e}}$ gives insights into the interaction between laser and plasma. The electric field of the laser can be thought of as a perturbation which can be expressed with the dispersion

[Boy20] Boyd (2020), "Chapter 12 - Optically Induced Damage and Multiphoton Absorption".
[Che16] Chen (2016), *Introduction to Plasma Physics and Controlled Fusion*.

relation

$$\omega_{\mathrm{L}}^2 = \omega_{\mathrm{p,e}}^2 + c^2|\vec{k}|^2, \tag{2.12}$$

$\vec{k}$ being the wave vector of the laser. As long as $\omega_{\mathrm{L}} > \omega_{\mathrm{p,e}}$ holds, $\vec{k}$ is real and the laser propagates through the plasma. For $\omega_{\mathrm{L}} = \omega_{\mathrm{p,e}}$, the wave vector vanishes and the laser cannot propagate further. The density connected to this equality is the *critical density*

$$n_{\mathrm{cr}} = \frac{\bar{\gamma}\epsilon_0 m_{\mathrm{e}}\omega_{\mathrm{L}}^2}{e^2} \approx 1.1 \times 10^{21} \left(\frac{\bar{\gamma}}{\lambda_{\mathrm{L}}^2}\right) \mathrm{cm}^{-3}. \tag{2.13}$$

For higher plasma frequencies with $\omega_{\mathrm{L}} < \omega_{\mathrm{p,e}}$, the plasma is called overdense. In this case, the wave vector $\vec{k}$ is imaginary and the electromagnetic field of the laser is exponentially attenuated. The length that the laser can penetrate into an overdense plasma is known as the specific skin depth δ. From (2.12) follows

$$\delta = \frac{c}{\sqrt{\omega_{\mathrm{p,e}}^2 - \omega_{\mathrm{L}}^2}}. \tag{2.14}$$

How the interaction of laser and plasma now enables the acceleration of electrons, i.e. explicitly the energy transfer from the electromagnetic wave to the plasma electrons, is discussed in the following section.

2.3 Absorption mechanisms

The mechanism that dominates the transfer of energy from the laser to the plasma electrons is highly reliant on the intensity $I\lambda^2$. Depending on this value as well as the pulse duration, there are multiple regimes of absorption mechanisms. These are the here called *low* intensities for $I\lambda^2 \leq 10^{16}\,\mathrm{W\,cm^{-2}\,\mu m^2}$, the *medium* intensity regime with $I\lambda^2 > 10^{15}\,\mathrm{W\,cm^{-2}\,\mu m^2}$ and a *high* intensity is characterised by $I\lambda^2 \geq 10^{18}\,\mathrm{W\,cm^{-2}\,\mu m^2}$. The used pulses in this thesis exceed $10^{20}\,\mathrm{W\,cm^{-2}\,\mu m^2}$ and are thus of high intensity. However, as the influence of laser contrast is studied and thus ns pulses with intensities up to $10^{13}\,\mathrm{W\,cm^{-2}\,\mu m^2}$ interact with the target, a brief overview over all three regimes is given.

For low intensities, the primary absorption mechanism is *collisional absorption*, also called *inverse bremsstrahlung* [MB10]. This process can only occur during the collision of an electron with an ion or another electron, at which point the energy from the electromagnetic wave can be transferred. The momentum exchange of two electrons with nearly identical velocities $v_{\mathrm{osc.}}$, occurring with frequency ν_{ee}, only leads to a thermalization of the distribution function [MB10]. For that reason, only electron-ion collisions with frequency ν_{ei} are considered. The effectiveness of this process is reliant on the time between collisions $\tau_{\mathrm{ei}} = \nu_{\mathrm{ei}}^{-1}$, where $\tau_{\mathrm{ei}} \propto T_{\mathrm{e}}^{3/2}/n_{\mathrm{e}}$ holds and T_{e} being the electron temperature. Due to the linear dependence of ν_{ei} and n_{e}, the effectiveness of the collisional absorption increases up to n_{cr}. However, T_{E} also rises with increasing intensity, explaining the decreasing effectiveness of this process for intensities $I > 10^{15}\,\mathrm{W\,cm^{-2}}$.

For collisional absorption, the ion provides an additional electric field in order to violate the Lawson-Woodward theorem and transfer the energy. For medium and high intensities such a collision is very rare and other means of irreversibility are necessary to explain the transfer of energy. These processes are often summarised under the topic of *collisionless absorption*. In case of the non-relativistic, medium intensity, this process is the *resonant absorption*. A p-polarised laser, which is incident on a target surface with angle

[MB10] Mulser and Bauer (2010), *High Power Laser-Matter Interaction*.

$\Theta \neq 0°$ with respect to the target normal, has an electric field component parallel to the density gradient of the expanding plasma. The laser propagates through the underdense plasma until it is reflected at n_{cr}. Here, the parallel component resonantly drives an electron plasma wave, hence the name resonant absorption. The actual energy transfer then occurs due to a damping of this wave, either through electron-ion collisions, Landau damping or wave breaking [MB10]. A key feature of the resonant absorption is the generation of relativistic, so-called *hot* electrons. Only a small portion of the plasma electrons actually interact with the laser, in contrast to collisional absorption, which interacts with most of the electrons. The effectiveness of resonant absorption depends on the angle of incidence, which is optimal for angles around $25°$, depending on the intensity.

Now relativistic intensities and plasmas with steep gradients, i.e. small scale lengths $l_{\mathrm{s}} = c_{\mathrm{s}}t$, are considered. For $l_{\mathrm{s}} < \lambda$ can the electron layer closest to n_{cr} interact directly with the laser field. Again, an incident laser with a parallel component to this steep gradient is assumed. During the first half cycle of this laser, the electrons are pulled into the vacuum in front of the critical surface and accelerated back into the overdense region in the second half cycle. There, the electric field of the laser is exponentially attenuated over the skin depth δ and the electrons see only a weaker electric field. The accelerated electron therefore propagates out of the interaction region practically undisturbed. This process, first described by [Bru87] as *not so resonant, resonant absorption*, is nowadays often referred to as *Brunel heating*.

If the assumption of $l_{\mathrm{s}} < \lambda$ does not hold, the process of *stochastic heating* can lead to electron acceleration. This process has been investigated by Chopineau *et al.* [Cho+19]. An electron in the underdense plasma in front of n_{cr} can be influenced by both the incident and reflected laser beam. Due to the presence of two electric fields, the Lawson-Woodward theorem can be ignored and the electrons gain energy in the standing wave of the superimposed beams through stimulated multiphoton Compton scattering [Cho+19].

Another mechanism is the so-called *j×B heating*, with $\vec{j} = en_{\mathrm{e}}\vec{v}$ [KE85]. Assuming a plasma scale length of $l_{\mathrm{s}} \approx \lambda$, and relativistic intensities of $a_0 > 1$, one finds an oscillating ponderomotive force in accordance with equation (2.9). This force accelerates electrons in the laser propagation direction with a frequency of $2\omega_{\mathrm{L}}$ due to the magnetic component of the Lorentz force. As this mechanism relies on a magnetic field component that is perpendicular to the movement of the electrons, a condition which is always fulfilled for a linearly polarised wave, it also works for s-polarised or target normal laser incidence.

Besides the already mentioned absorption mechanisms, a multitude of other processes have been proposed [CM77; Yan+95; Mac+01; Ums03]. Overall, it is assumed that in a typical laser generated plasma, multiple mechanisms work in parallel, depending on time scales, intensity and extent of pre-plasma formation, that is the plasma scale length. In general, all collisionless absorption mechanisms have in common that they produce a distribution of *hot* electrons. The distribution of these hot electrons can be described in the relativistic case with a Maxwell-Jüttner distribution

$$f(\gamma) = N_{\mathrm{h}} \frac{\gamma^2 \beta}{\frac{k_{\mathrm{B}}T_{\mathrm{h}}}{m_{\mathrm{e}}c^2} K_2(m_{\mathrm{e}}c^2/k_{\mathrm{B}}T_{\mathrm{h}})} \exp\left(-\frac{\gamma m_{\mathrm{e}}c^2}{k_{\mathrm{B}}T_{\mathrm{h}}}\right), \tag{2.15}$$

[Bru87] Brunel (1987), "Not-so-resonant, resonant absorption".
[Cho+19] Chopineau et al. (2019), "Identification of Coupling Mechanisms between Ultraintense Laser Light and Dense Plasmas".
[KE85] Kruer and Estabrook (1985), "J×B heating by very intense laser light".
[CM77] Catto and More (1977), "Sheath inverse bremsstrahlung in laser produced plasmas".
[Yan+95] Yang et al. (1995), "Absorption of laser light in overdense plasmas by sheath inverse bremsstrahlung".
[Mac+01] Macchi et al. (2001), "Surface Oscillations in Overdense Plasmas Irradiated by Ultrashort Laser Pulses".
[Ums03] Umstadter (2003), "Relativistic laser plasma interactions".

with $\beta = v/c$, T_h and N_h being the temperature and total number of the hot electrons, and K_2 being the second order Bessel function [McK+13]. The last missing piece is then a scaling of the hot electron temperature T_h with the intensity. Various models have been proposed, however the ponderomotive j×B scaling by Wilks *et al.* [Wil+92] appears as a good approximation for relativistic intensities. The scaling law is

$$k_\mathrm{B} T_\mathrm{h} = m_\mathrm{e} c^2 \left(\sqrt{1 + \frac{a_0^2}{2}} - 1 \right). \tag{2.16}$$

For the used laser pulses in this thesis of about $10^{20}\,\mathrm{W\,cm^{-2}}$, the expected hot electron temperature is approx. $2\text{-}3\,\mathrm{MeV}$.

2.4 Electron transport

After acceleration, the hot electrons penetrate deep into the still cold target. This propagation is discussed in the following sections. The concept of charge neutrality is explored in Sec. 2.4.1. The recirculation of hot electrons within a target is the topic of Sec. 2.4.3. In the last Sec. 2.4.2 deals with the energy loss within the target.

2.4.1 Charge neutrality

The hot electrons that penetrate the target carry a considerable charge. This large current is causal for large electric and magnetic fields. In particular the magnetic fields act against the propagation of the electrons. The limit of a current in a conductor due to the self-generated fields is described by [Alf39; DAV06] and has the following form

$$I_\mathrm{A} = \beta\gamma \frac{4\pi m_\mathrm{e} c}{\mu_0 e} = \beta\gamma \cdot 1.7 \times 10^4\,\mathrm{A}. \tag{2.17}$$

To illustrate (2.17), consider the following example from McKenna *et al.* [McK+13]. The current generated by hot electrons, which in turn are the result of a $100\,\mathrm{J}$, $1\,\mathrm{ps}$ laser pulse, is in the order of $10\,\mathrm{MA}$. The maximum current according to the Alfvén limit on the other hand is $65\,\mathrm{kA}$. This difference of almost three orders of magnitude would prohibit any propagation of the hot electrons into the target. The solution to this problem is a larger return current of slow electrons. The process is as follows: due to the acceleration of hot electrons out of the focus region of the laser, a strongly positively charged region is generated there. The background electrons within the target see the increasing electric field and are pulled to the front surface. This current then generates in turn electric and magnetic fields that act opposite to those of the hot electrons. It follows

$$\vec{j}_\mathrm{h} + \vec{j}_\mathrm{r} = 0, \tag{2.18}$$

with $\vec{j}_\mathrm{h,r}$ the hot electron and return current, respectively. The time t it takes to achieve charge neutrality is given by the mobility of the electrons with

$$t = \frac{2\pi}{\omega_\mathrm{p,e}}. \tag{2.19}$$

[McK+13] McKenna et al. (2013), *Laser-Plasma Interactions and Applications*.
[Wil+92] Wilks et al. (1992), "Absorption of ultra-intense laser pulses".
[Alf39] Alfvén (1939), "On the Motion of Cosmic Rays in Interstellar Space".
[DAV06] DAVIES (2006), "The Alfvén limit revisited and its relevance to laser-plasma interactions".

Assuming an electron density of approx. $10^{23}\,\mathrm{cm}^{-3}$, charge neutrality is reached after about $0.9\,\mathrm{fs}$ in a copper (Cu) target, a much shorter time than the pulse length of $500\,\mathrm{fs}$ of the Petawatt High Energy Laser for Heavy Ion Experiments (PHELIX) laser. The time is slightly longer for non-conductors, where the mobility of the electrons is greatly reduced.

2.4.2 Stopping power

Assuming that an adequate charge neutrality is achieved the hot electrons propagate through the target. Multiple processes lead to a loss of energy during this propagation. These include elastic and inelastic collisions, leading to excitation, ionisation or recombination with target atoms and radiative losses in the form of bremsstrahlung. A measure of the energy loss is the *stopping power*

$$\left(\frac{\mathrm{d}E}{\mathrm{d}s}\right)_{\mathrm{total}} = \left(\frac{\mathrm{d}E}{\mathrm{d}s}\right)_{\mathrm{col}} + \left(\frac{\mathrm{d}E}{\mathrm{d}s}\right)_{\mathrm{rad}}, \tag{2.20}$$

In Fig. 2.2, the stopping power of electrons in Cu is shown. The typical energy regime of hot electrons lies between 0.5 - $20\,\mathrm{MeV}$, the radiative stopping power S_{rad} of Cu is lower than the stopping power through collisions S_{col}. The total stopping power displays a minimum around $1\,\mathrm{MeV}$ and the collisional stopping power is nearly constant for higher energies. The line density to stop such an $1\,\mathrm{MeV}$ electron in a Cu foil is $0.6367\,\mathrm{g\,cm}^{-2}$, corresponding to a maximum range of $710\,\mu\mathrm{m}$ [Ber+]. In comparison to the hot electrons, the stopping power for lower energy electrons is much higher. The majority of target heating is thus due to already slowed down electrons.

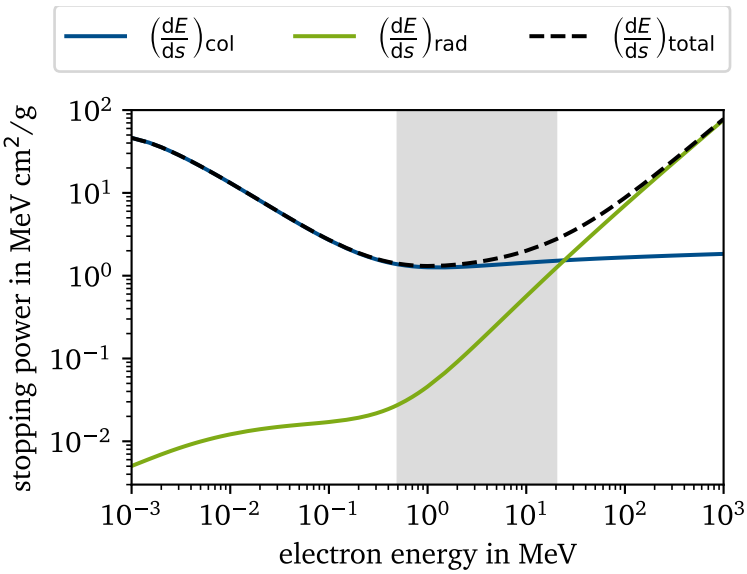

Figure 2.2: Stopping power for Cu. For electron energies below $20\,\mathrm{MeV}$ the collisional stopping power dominates over radiative losses. The typical energies of hot electrons produced by a relativistic laser pulse is indicated with a gray box. The data was obtained from [Ber+]

[Ber+] Berger et al., *ESTAR*.

2.4.3 Refluxing

Of the accelerated electrons a small fraction will escape the target on the back side. A quasi-electrostatic space-charge sheath field forms at the back side, that reflects the majority of the remaining hot electrons back towards the front surface. A similar process occurs on the front side, such that the hot electrons are trapped between these two surfaces and start to recirculate (or *reflux*) between them. A limit for this refluxing is the target thickness, which corresponds to the above described maximum range of the electrons. If the electrons lose too much energy during each pass of the target, no effective refluxing can occur. Following the example above, a Cu target should not be thicker than a fraction of the maximum range of $710\,\mu\mathrm{m}$ to allow for multiple passes through the target. The in this work investigated targets are therefore well below this limit with thicknesses in the range of $20\text{-}30\,\mu\mathrm{m}$ (see Chapter 4). Refluxing hot electrons have been shown to play a vital role in the effective generation of $K\alpha$ emission within a target [Neu+10]. The reason for this is further discussed in Sec. 3.1.1.

Another effect of the recirculation is a lateral transport of the electrons. As discussed in Sec. 2.1, the electrons experience a transversal acceleration due to the ponderomotive force. This beam divergence leads to a further spread upon reflection at either surface. Simulations have shown a near conservation of the transversal momentum upon reflection, leading to a much larger volume that is populated with hot electrons [McK+13].

[Neu+10] Neumayer et al. (2010), "The role of hot electron refluxing in laser-generated K-alpha sources".

3 X-ray radiation

The emphasis of this thesis is the analysis of X-ray spectra, emitted from laser-driven solid state targets. Therefore, the fundamental physics of this radiation, originally discovered by Wilhelm Conrad Röntgen in 1895 and rationale for the first Nobel Prize in Physics in 1901, will be the topic of this chapter [Rön95; Rön96; Rön97].

In the first section 3.1, the generation of X-ray generation is covered, including the emission of strongly ionised states (see section 3.1.4) and the advantages of $K\alpha$ emission over thermal line emission (see section 3.1.5). Atomic radiative codes, used to generate emission spectra from plasmas, are introduced in section 3.2. In order to derive the ionisation population distribution from the thermodynamic variables temperature and density, a collisional-radiative model is used, which is explained in further detail in section 3.2.1. The generation of an emission spectrum on the basis of the calculated ionisation population distribution is discussed in section 3.2.2. The chapter closes with an overview over various X-ray diagnostics schemes. Multiple crystal spectrometer layouts are presented in section 3.3.2. The final detection of the X-rays with the help of image plates (IPs) is the topic of section 3.3.3.

3.1 X-ray generation

In the previous chapter 2, the production of hot electrons during the interaction of a relativistic laser pulse with a solid target has been discussed. These electrons then propagate into the target and interact with the electrons and nuclei of the target matter, as described in section 2.4. There are three main channels of interaction between the electrons and the target which result in the emission of electromagnetic radiation. If the electron is deflected in the Coulomb field of a nucleus, it experiences a deceleration and the energy difference is emitted as a photon. This so called *bremsstrahlung* is also known as free-free radiation, as the electron is not bound before and after the interaction. The electron can also collide with a bound electron, thereby exciting or ionising the atom. This produces a vacancy, which if filled by a higher lying bound electron, releases the binding energy difference in form of a photon. The energy difference is characteristic for each element, from which the name *characteristic X-ray radiation* is derived. It is also sometimes called bound-bound emission. The last interaction is more relevant in the context of a plasma, as it requires a pre-existing vacancy. This vacancy can be filled through electron-capture, releasing the energy difference $E_{\text{kin}} + E_{\text{B}}$. This energy is then emitted as a photon in a process called *radiative recombination*. It can also be transferred to a second electron, which is excited and later relaxes with the emission of a photon (dielectronic recombination). As the primary electron is bound after the interaction, this channel is sometimes called the free-bound emission [Dem16].

While the above mentioned interactions all result in the emission of X-ray radiation, for the sake of completion it should be mentioned that there are rivalling interactions that do not. For example, in the case

[Dem16] Demtröder (2016), *Experimentalphysik 3*.

of the bound-bound and free-bound transitions, the released energy can be transferred to a third electron in processes called the Auger effect and the three-body recombination, respectively. As more energy is shifted from the hot electrons towards the bulk matter, the target is heated.

Of the three channels of X-ray production, both the free-free and the free-bound transitions emit a continuous spectrum. In contrast, the bound-bound transition occurs with a well defined energy difference of the two binding energies E_1 and E_2 for the lower and higher bound states, respectively. This produces a line emission, which is not only dependent on the involved bound states but also of the atomic number Z, leading to the name characteristic radiation. The properties of the characteristic radiation will be discussed in the following section.

3.1.1 Characteristic X-ray radiation

Fundamental to the understanding of the characteristic line emission is the knowledge about the energy states a bound electron can occupy before and after the transition. A bound state is defined by the principal quantum number n, which denotes the occupied electron shell. Furthermore, the electrons orbital l and the spin s describe the electrons sub-shell position. Together with the number of electrons in a specific orbital h, the electron configuration of an element is described by $(nl)^h$. The orbital of an electron l is here typically denoted by a lower case letter (s$=0$, p$=1$, d$=2$, f$=3$). As an example, the electron configuration of a neutral copper (Cu) atom is $(1s)^2(2s)^2(2p)^6(3s)^2(3p)^6(3d)^{10}(4s)^1$.

For multi-electron atoms, the various electron states are combined. The orbital quantum number L and the total spin S can be derived from the electron configuration. In light atoms ($Z \leq 30$), the orbital and spin angular momenta L and S couple to form a total angular momentum $J = L + S$. Together with the spin multiplicity $2S + 1$, the atom is completely defined by the term symbol

$$^{(2S+1)}L_J. \tag{3.1}$$

In the case of the ground state Cu atom, the term symbol is $^2S_{1/2}$, which can be derived from the highest not completely filled shell. In this case this is the 4s electron, which corresponds to $l = L = 0$ and $s = S = 1/2$. The multiplicity 2 indicates, that the spin orientation of the unpaired 4s electron is not defined and can be $+1/2$ and $-1/2$. Such a state is called a doublet, while multiplicities of 1 and 3 are called singlet and triplet states, respectively.

The energy level of a specific electron is furthermore influenced by the spin-orbit interaction. This is a result of the interaction between the electron's magnetic dipole, its orbital motion and the electrostatic field of the positive nucleus. The corresponding total angular momentum quantum number is $j = l + s$. For example, the possible states of an electron in the 2p sub-shell split into $l = 1, s = +1/2, j = 3/2$ and $l = 1, s = -1/2, j = 1/2$. The specific spin-orbit coupling is denoted by a subscript j, i.e. $2p_{3/2}$. The projection of the total angular momentum j along a specific axis, i.e. z is then $j_z = -j, -j+1, ..., j-1, j$, such that $2j + 1$ electrons can be placed into the specific energy level.

As discussed in section 2.4, hot electrons reflux through the target. During collisions with bound electrons, part of the kinetic energy is transferred. If this energy is larger than the binding energy of the bound electron, the atom is ionised. The cross section for *K*-shell and *L*-shell ionisation in Cu is plotted in figure 3.1. It sharply rises above the binding energy up to a maximum around four to five times the binding energy of $8979\,\mathrm{eV}$ and $932.7\,\mathrm{eV}$ for the *K*-shell and *L*-shell of Cu, respectively. This produces a vacancy, which can be filled by an electron bound in a higher shell, thereby freeing the energy difference of the bound levels. This energy is then released as a photon. Depending on the involved levels of the electron, it is

common to refer to the emitted radiation as K-shell or L-shell radiation, depending on the lower level. For a transition between two neighbouring shells, it is customary to add an α, while a β refers to $\Delta n = 2$. Furthermore, if the observed spectrum is highly resolved, a further splitting of the emission due to the spin-orbit coupling can be observed. The resulting, slightly varying energies, are numbered from highest emission probability with a 1 to lowest emission probability. The relative emission probability can be calculated from the degeneracy of the spin-orbit coupled sub-shells. For example, 4 electrons can be placed in the $2\mathrm{p}_{3/2}$ energy level, while only 2 fit into the $2\mathrm{p}_{1/2}$, resulting in a relative intensity between $K\alpha_1$ to $K\alpha_2$ of 2:1. In figure 3.2, the principle emission of a $K\alpha$ photon in Cu, as well as the fine structure splitting into $K\alpha_1$ and $K\alpha_2$ is depicted. The available energy can also be transferred to a secondary bound electron, which in turn is ionised (Auger electron) and does not contribute to the emission of X-ray radiation. The ratio of emitted photons over Auger electrons is called the *fluorescence yield*, which steadily increases with Z. For Cu, the fluorescence yield is roughly $40\,\%$.

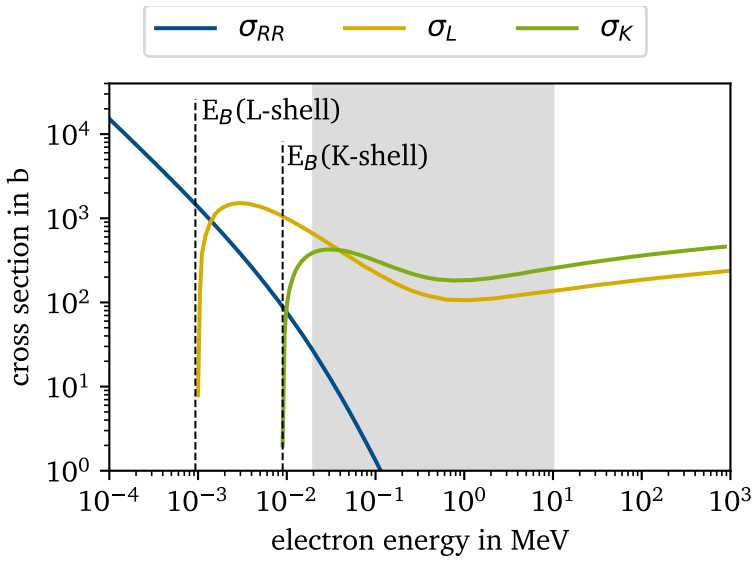

Figure 3.1: Cross sections for electron-ion interactions in Cu. For low energies, the radiative recombination (blue) prevails. The cross sections for L-shell (orange) and K-shell (green) ionisation rises sharply above the respective binding energy E_B. For the relevant regime of $0.02\text{-}10\,\mathrm{MeV}$, the ionisation of K-shell electrons is more likely than L-shell electrons. The ionisation cross sections are taken from [Llo+14], the radiative recombination cross section is found in [IE00].

Not every possible transition between the energy levels is observed. As photons are bosons and the angular momentum must be conserved, only transitions with $\Delta l = \pm 1$ are allowed. In addition, the value of the total spin should not change ($\Delta S = 0$), while the total angular momentum of the atom can change ($\Delta J = 0, \pm 1$) and must change in the case of $J = 0$ [Dem16]. For heavy elements, the spin-orbit coupling increases. This somewhat softens the rule $\Delta S = 0$ and the multiplicity can change, resulting in so-called intercombination lines.

The energy of a characteristic X-ray photon is well defined, as the electrons are bound on discreet energy levels. If the spin-orbit coupling is disregarded, the frequency ν_{21} of the emitted photon for a transition

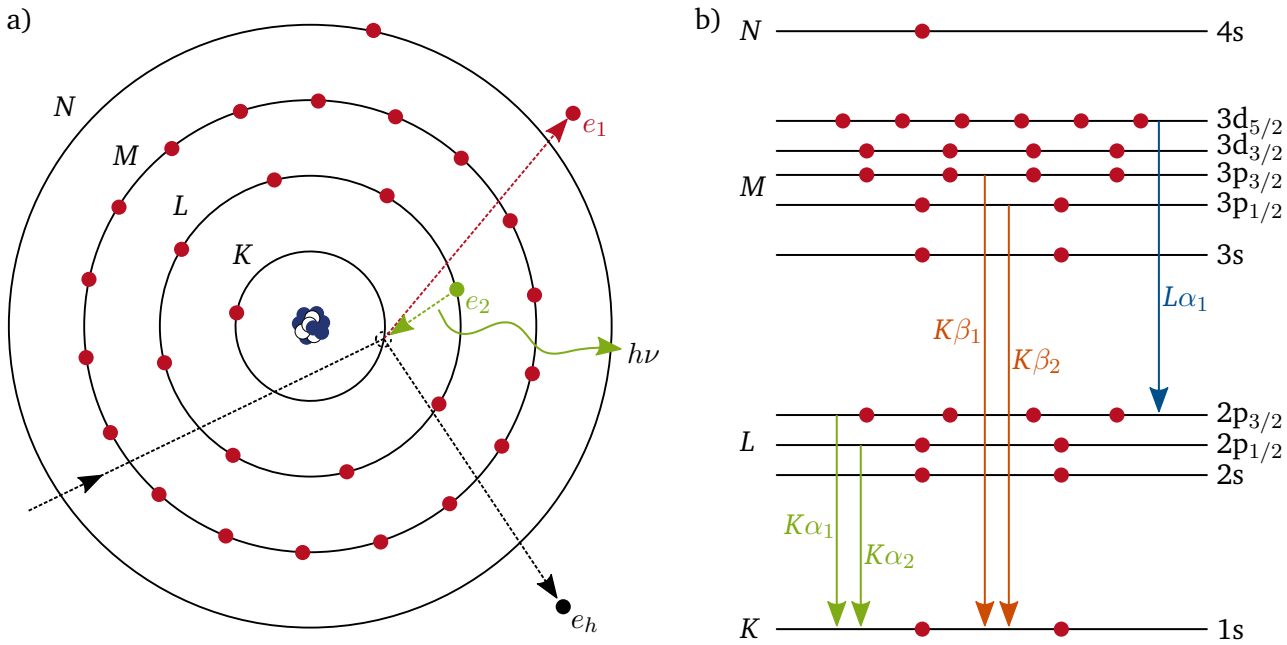

Figure 3.2: Principle of characteristic $K\alpha$ emission a) and level scheme of bound levels b) in Cu. An energetic electron e_h collides with a bound *K*-shell electron e_1, transferring enough energy for an ionisation. The vacancy on the *K*-shell gets filled by a *L*-shell electron e_2 and the energy difference of the bound levels is emitted as a photon with energy $\Delta E = E_{\mathrm{B},K} - E_{\mathrm{B},L} = h\nu$. As a convention, the lower shell provides the radiation name, while the greek letter indicates the shell difference. The energy levels of a specific shell split due to the spin-orbit coupling. A subscript number indicates the specific subshell.

from state n_2 to state n_1 can be calculated as follows:

$$\nu_{21} = \frac{c}{\lambda_{21}} = f_{\mathrm{R}} Z_{\mathrm{eff}}^2 \left(\frac{1}{n_1^2} - \frac{1}{n_2^2} \right) \quad \text{with} \tag{3.2}$$

$$f_{\mathrm{R}} = c R_\infty \frac{1}{1 + \frac{m_e}{M}} \quad \text{and} \tag{3.3}$$

$$Z_{\mathrm{eff}} = Z - S. \tag{3.4}$$

Here, c is the speed of light, f_{R} is the Rydberg frequency, derived from the Rydberg constant R_∞ and adjusted with the nuclear mass M of the element+[Dem16]. The frequency is further decreased through the screening of the bound electrons, expressed through the screening constant S, leading to an effective atomic number Z_{eff}. In the case of a $K\alpha$ emission, equation (3.2) simplifies to the known Moseley law:

$$\nu_{K\alpha} = c/\lambda_{K\alpha} = \frac{3}{4} f_{\mathrm{R}} \left(Z - 1\right)^2 . \tag{3.5}$$

3.1.2 Line width

While equations 3.2 and 3.5 indicate, that the observed radiation should be monochromatic, this is not the case. In practice, the observed transition is always represented by a distribution of the spectral power

density P_ν around the frequency ν. This distribution is the result of multiple effects. These include the natural line width, the Doppler broadening and the pressure broadening.

The most basic line broadening is the *natural line width*, which arises due to the finite life time of the excited states of an atom. This results in a finite energy width $\delta E = \hbar/\tau_i$ and in turn to a corresponding frequency spread. The spectral density of the natural line width is a Lorentzian distribution [Dem16] of the following form

$$P_\mathrm{n}(\nu) = P_0 \frac{\gamma/(2\pi)}{4 * \pi^2 (\nu - \nu_0)^2 + (\gamma/2)^2}. \tag{3.6}$$

Here, ν_0 is the central transition frequency and P_0 is the total emitted power. The parameter γ can be thought of as a damping coefficient correlated to the finite life time of the excited state $\tau = 1/\gamma$. A defining value of such a distribution is its full width at half maximum (FWHM). Derived from 3.6, the natural line width is

$$\Delta\nu_\mathrm{n} = \gamma/2\pi = \frac{1}{2\pi\tau_i} \tag{3.7}$$

While the typical natural line width of transitions in the visible electromagnetic spectrum is very small, the short life time of *K*-shell vacancies leads to a non negligible broadening. For example, the natural line width of the Cu $K\alpha_1$ at $8047\,\mathrm{eV}$ is $2.11\,\mathrm{eV}$, corresponding to a lifetime of the *K*-shell vacancy of $0.31\,\mathrm{fs}$ [KO79].

If the excited atom is disturbed by a collision, the life time can be influenced and substantially shortened. Due to the reciprocal relation between life time and γ, this results in a higher line width. In principle, the reduced life time can be estimated by the mean free path between two collisions [Dem16]. One finds the line width $\Delta\nu_\mathrm{p}$ due to collisions is approximately

$$\Delta\nu_\mathrm{p} = \frac{1}{2\pi} n\sigma \sqrt{\frac{8k_\mathrm{B}T}{\pi\mu}}, \tag{3.8}$$

with n denoting the particle density of the colliding projectiles, σ the cross section for such a collision and μ the reduced mass of the two colliding particles [Dem16]. It is observed, that $\Delta\nu_\mathrm{p}$ increases linearly with n, that is the pressure exerted by these particles on the emitting atom. As such, this process is called *pressure broadening*. If both collision partners belong to the same species, this leads to a self-broadening of the line simply due to the pressure of the emitting material. The resulting spectral density is again of Lorentzian shape. The collisions can also lead to a shift of the central frequency ν_0. During the collision, the binding potentials of the two collision partner can influence each other and temporarily shift the binding energy, leading to a changed frequency ν_0. Typically, this broadening and shifting process can be neglected when dealing with solids, and is only of relevance in high-density, low temperature plasmas. As an example, for solid density Cu penetrated by an energetic electron distribution, the line width increase is only $3\,\mathrm{meV}$ and negligible.

Of more importance in the context of a plasma is the *Stark broadening*. This process is in principle a pressure broadening due to the electronic microfields generated by the charged particles. A theoretical description of this mechanism is complicated and will be omitted for the scope of this thesis. For singly charged ions, the Stark width depends linearly on the electron density n_e [MW06; Zme+10]. As such, if the temperature of the emitting plasma is well characterised, a Stark width analysis can be a powerful tool to determine the electron density. A review of the current models has been compiled by Gigosos [Gig14].

[KO79] Krause and Oliver (1979), "Natural width of atomic K and L level Kα X-ray lines and several KLL Auger lines."
[MW06] Martin and Wiese (2006), "Atomic Spectroscopy".
[Zme+10] Zmerli et al. (2010), "Stark broadening calculations of neutral copper spectral lines and temperature dependence".
[Gig14] Gigosos (2014), "Stark broadening models for plasma diagnostics".

The last line broadening mechanism is due to the thermal motion of the emitting atoms. The velocity of the atoms leads to a Doppler shift during the emission, resulting in a varying emission frequency. For this reason, this broadening is often called the *Doppler broadening*. Assuming a Maxwellian velocity distribution with a thermal velocity v_{therm} of the atoms and the central transition frequency ν_0, the spectral power density can be calculated by

$$P_{\text{D}}(\nu) = P_0 * \exp^{-[c(\nu-\nu_0)/(\nu_0 * v_{\text{therm}})]^2} \qquad \text{with} \tag{3.9}$$

$$v_{\text{therm}} = (2k_{\text{B}}T/m_{\text{e}})^{1/2}, \tag{3.10}$$

k_{B} being the Boltzmann constant and m_{e} the electron mass. The corresponding FWHM of this Gaussian distribution is calculated as follows:

$$\delta\nu_{\text{D}} = \frac{2\nu_0}{c} * \sqrt{(2k_{\text{B}}T/m_{\text{e}}) * \ln 2}. \tag{3.11}$$

Using equation 3.11, the broadening of the $K\alpha_1$ of Cu with a temperature of $200\,\text{eV}$ is expected to be $1.1\,\text{eV}$ and in a similar order of magnitude as the natural line width. As the Doppler width depends on the temperature with $\sqrt{T}$, it can be a useful tool to determine the temperature of the emitting material.

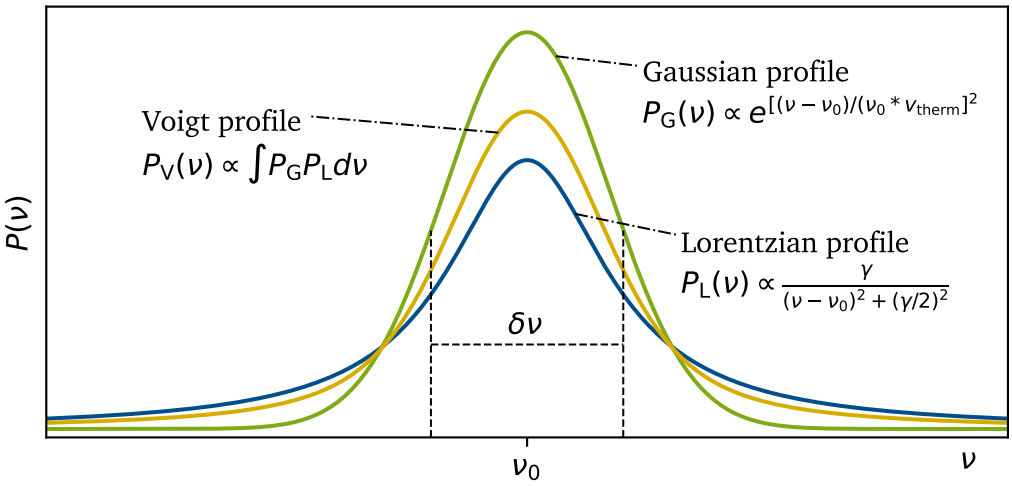

Figure 3.3: Comparison of different peak profiles with the same FWHM. The Lorentzian profile describes broadening mechanisms such as the natural line width or pressure broadening. The Gaussian profile is usually associated with the Doppler broadening. The folding of a Gaussian and Lorentzian profile leads to a Voigt profile. The profile approaches a Gaussian shape around the central frequency ν_0, while the wings correspond more closely to the Lorentzian profile.

In practice, the observed line is influenced to a different degree by all broadening mechanisms. The resulting line shape is a convolution of the above mentioned spectral power densities. The folding of a Lorentzian and a Gaussian results in a Voigt profile, the typically observed line shape. All three profiles are displayed in figure 3.3. Whenever an X-ray spectrum is measured, the instrument imposes an additional broadening onto the observed lines. The reason for this additional broadening can be found by studying the Rocking curve and is discussed in section 3.3.1. For the instruments used in this work, the expected broadening ranged between 1 - $20\,\text{eV}$, depending on the used crystal.

The described line shape only holds, if the radiation can escape the emitting material. If the mean free path of a photon is much smaller than the size of the emitting volume, the energy can be absorbed and

re-emitted multiple times. Such a line is called optically thick and experience further broadening, called the opacity broadening. The next section will discuss the scattering and absorption mechanisms of X-ray photons in a plasma to better gauge, which lines are optically thick.

3.1.3 X-ray scattering and absorption

As X-ray radiation passes through matter, the radiation is attenuated. Causal for this attenuation are multiple processes. The photon can be scattered coherently, also referred to as *elastic scattering*. The cross section for coherent scattering is proportional to ν^4 [Dem16]. Therefore, X-ray radiation is much more strongly scattered than visible light. Furthermore, the photons can be incoherently scattered (*Compton scattering*). Part of the energy is here transferred to a lightly bound electron in an outer shell ($E_\mathrm{B} \ll h\nu$), which can be excited or ejected. As the energy of the photon is decreased, the probability of a complete absorption increases. During the so-called *photoelectric absorption*, the energy is transferred to a tightly bound electron, like an *L*-shell or a *K*-shell electron, thereby ionising it. In order for photoelectric absorption to occur, the energy $h\nu$ must be larger than the binding energy of the electron E_B. For much larger energies, the energy can also be transformed into an electron-positron pair. This pair production only occurs in the vicinity of the electric field of a nucleus. The cross section of these processes are connected to the linear attenuation coefficient α and the mass attenuation coefficient μ with

$$\mu = \frac{\alpha}{\rho} = \frac{n\sigma}{\rho}, \tag{3.12}$$

where n is the particle density and ρ the mass density of the attenuating material.

The mass attenuation coefficients in Cu of the here mentioned processes are plotted in figure 3.4. For energies above $10\,\mathrm{MeV}$, pair production dominates the attenuation. As the energy decreases, Compton scattering μ_incoh starts to occur. This process is the main fraction of the attenuation between 250 - $10\,000\,\mathrm{keV}$. For photon energies below $250\,\mathrm{keV}$, the photoelectric effect μ_ph is strongest. At $9.979\,\mathrm{keV}$, a sharp drop in the photoelectric attenuation indicates, that the photon energy is too low to ionise *K*-shell electrons. Therefore, this edge is called the *K* edge, and similar feature can be observed for every major energy level.

To assess the optical thickness of a line, one can calculate the *mean free path* l of a photon with energy $h\nu$ as follows

$$l = \frac{1}{\mu_\mathrm{tot}(h\nu)\rho}. \tag{3.13}$$

The mean free path of X-ray photons in Cu for the relevant range of *K*-shell emission between 8 - $9\,\mathrm{keV}$ is plotted in figure 3.5. The *K* edge is clearly visible, decreasing the mean free path for energies above the *K*-shell ionisation threshold. This sudden drop of l, which corresponds to a reduced transmission, can be useful tool to filter specific parts of a spectrum and block energies above the *K* edge. For photons with energies below the *K* edge, the mean free path in Cu is between 20 - $30\,\mathrm{\mu m}$ [HGD93]. As a consequence, one can assume that a Cu foil of thickness $d \ll 20\,\mathrm{\mu m}$ and at room temperature is optically thin for the main *K*-shell emission and the lines are not further influenced by self-absorption.

Strong heating of the emitting material increases the mean ionisation and substantially changes the cross sections for scattering and absorption processes. As an example, the mean free path in solid Cu heated to various temperatures is displayed in figure 3.5 as well. For a lower temperature of $10\,\mathrm{eV}$, l deviates

[HGD93] Henke et al. (1993), "X-ray interactions: photoabsorption, scattering, transmission, and reflection at E=50-30000 eV, Z=1-92".

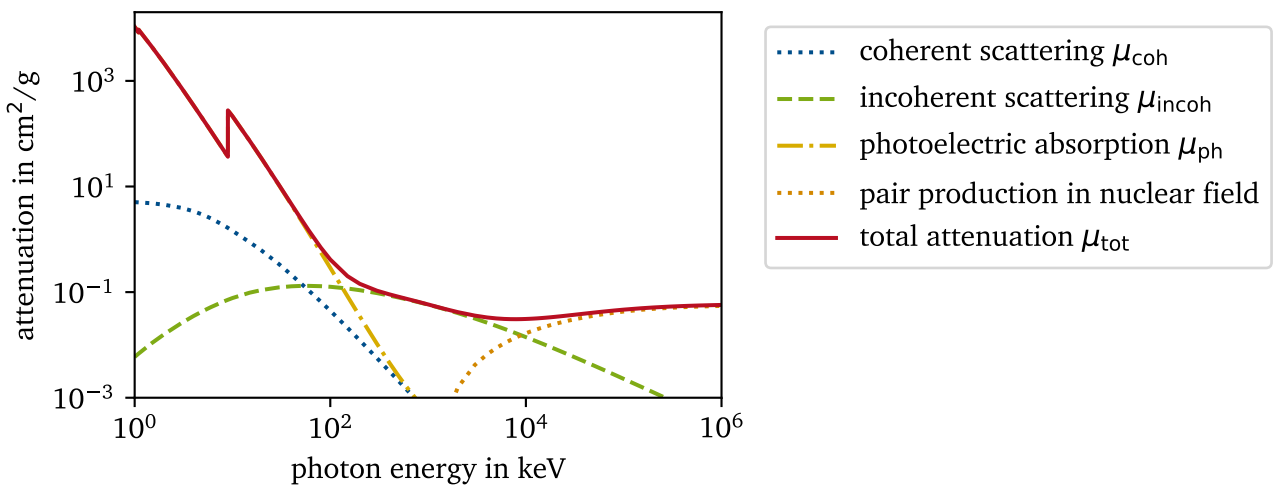

Figure 3.4: Attenuation of X-rays in $BaFBr_{0.85}I_{0.15}$. For photon energies below $10\,\mathrm{keV}$, the total attenuation μ_{tot} is dominated by photoelectric absorption (orange, dash-dot). For larger energies, incoherent scattering is more likely, up to an energy of about $10^4\,\mathrm{keV}$. Beyond that energy, the attenuation is mainly due to pair production in the nuclear field. The presented data is obtained from [BH87].

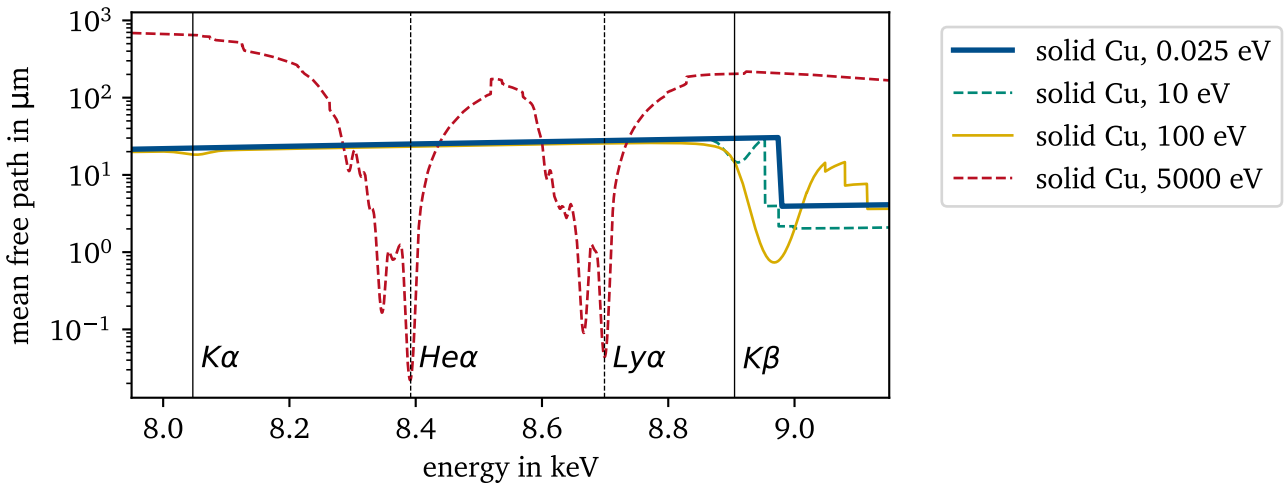

Figure 3.5: Mean free path of X-ray photons in Cu for various temperatures. The cold case (blue) displays a clear decrease beyond the *K* edge. With increasing electron temperature, the mean free path around the *K* edge decreases further and the ionisation of the *M*-shell leads to a more likely absorption of $K\beta$ radiation. At $100\,\mathrm{eV}$, even a slight decrease due to $K\alpha$ absorption can be seen. For very high temperatures of $5\,\mathrm{keV}$, the absorption changes massively. The plasma is virtually transparent for the cold lines $K\alpha$ and $K\beta$, while high absorption for the thermal lines is observed (see section 3.1.4). For room temperature, the data is obtained from [HGD93], for the other temperatures, the mean free path was determined with the atomic radiative code FLYCHK [Chu+05].

mainly around the $K\beta$ line from the cold case. The decreased mean free path here indicates, that there are vacancies on the M-shell available, such that photons can be absorbed while exciting a K-shell electron to the M-shell. One can also observe a larger line width for absorption, which is the result of an increased Doppler broadening with higher temperature (see section 3.1.2). Increasing the temperature further to $100\,\mathrm{eV}$, this effect is much more developed, even decreasing l below the K edge level. The central frequency is also shifted towards higher energies. This is the above mentioned frequency shift due to pressure broadening. The ionisation has also reached the L-shell, indicated by the small decrease of l around the $K\alpha$ line. A very different situation is observed at much higher temperatures of $5000\,\mathrm{eV}$. Here, the material is almost completely ionised, and only a few atoms have one or two remaining bound electrons. The emission and absorption behaviour of these few electron states will be discussed in the following section.

3.1.4 Thermal line emission

As the plasma is heated due to collisions of the return current and the relativistic electrons, the ionisation of the material increases, drastically shifting the energy levels. This gives rise to multiple additional observed lines, so-called X-ray satellites. The electronic screening of the nucleus charge decreases with each removed electron. In particular, electrons initially bound in the same or lower shells as the observed transition shells contribute the most to the energy shift. For example, only a slight energy shift is observed for the $K\alpha$ line, if electrons from the M-shell are removed. On the other hand, a stronger energy shift can be measured as soon as electrons from the L-shell are missing. For differentiation from the main $K\alpha$ line it is customary to label these ionisation states after the element corresponding to the remaining electron number, i.e. the ion with 3 remaining electrons would be called Li-like. These ionised states can then be excited and de-excited as discussed in section 3.1.1 and follow the same nomenclature. A transition of 1s2p $^1P_1 \rightarrow$1s^2 $^1S_0$ would for example be called a Heα_1 line.

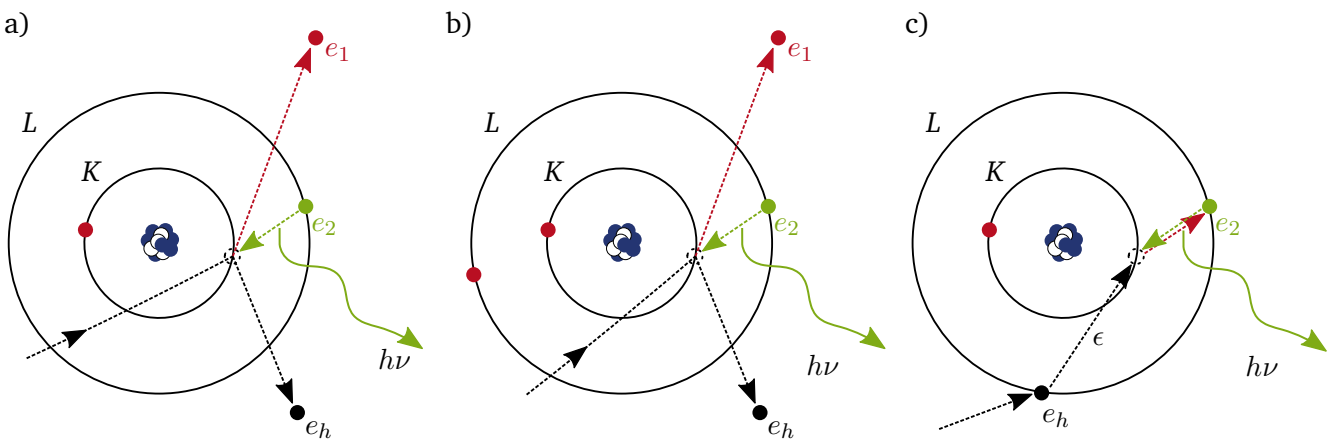

Figure 3.6: Principle schema for satellite line emission and dielectronic recombination. The emission of a Heα photon is sketched in a). Initially, only three bound electrons remain. One of the K-shell electrons e_1 is ionised through the collision with a hot electron e_h. The L-shell electron e_2 then fills the vacancy, thereby emitting the Heα photon. For the lithium (Li)-like satellite (b), the interaction is very similar, however an additional L-shell electron is present. In c), a hot electron is captured in the L-shell, transferring the energy ϵ to a bound K-shell electron e_2. This electron is lifted into the L-shell before falling back again, thereby releasing a photon with energy similar to the satellite line emission.

As the K-shell electrons are much more tightly bound than L-shell electrons, the population of He-like ions is very stable in typical laser plasmas. For this reason, the term *resonance line* is often found in literature for a 2p→1s transition in He-like or H-like atoms, the latter often denoted as Lyα. Besides these two transitions, a multitude of excited states can be found, where one spectator electron further influences the energy levels. For example, a transition of the type 1s2pnl'→2snl' with n≥ 2 produces additional satellites to the Heα transition line. The transitions resulting in a Heα resonance emission and Liα satellite emission are displayed in figure 3.6.

In addition to the above described shifted transitions, electron capture can also lead to shifted line emission. The so-called dielectronic recombination can be described as follows. A free electron is caught in a bound level and the released energy excites a second electron. This electron is then again de-excited, emitting a photon that has again a lower energy than the resonant energy transition (see figure 3.6).

3.1.5 Conversion efficiencies

The amount of emitted X-ray radiation from a laser-driven backlighter is an important parameter. Often, the conversion efficiency (CE) η, defined as the ratio of the total X-ray energy E_{X} in 4π to the laser energy E_{L}, is used to estimate the viability of a backlighter for a specific experiment. In the range of a few keV, the Heα and Lyα lines discussed in the previous section have been shown to be a very efficient mechanism for laser to X-ray energy conversion [GR09]. High CEs between 10^{-2} - 10^{-4} have been reported. In addition to the high CEs, Heα sources provide many desirable features, such as a temporal duration in the order of the laser duration, a small source size and a high total photon yield. A typical source is for example a Ti foil with a Heα transition at $4.75\,\mathrm{keV}$, driven with $100\,\mathrm{ps}$ to $1\,\mathrm{ns}$ laser pulses and intensities between 10^{14} - $10^{17}\,\mathrm{W\,cm^{-2}}$. However, He$\alpha$ sources are less efficient when realised with higher Z materials, such as Ag, that would lead to an increased energy of the Heα transition. This is due to the increased energy expenditure needed to ionise a bigger number of bound electrons of the higher Z materials to reach a He-like state. The result is that a decrease in CE is observed with increasing Z, making line emission with for example Ag (E_{ph} ~$22.6\,\mathrm{keV}$) very inefficient. Increasing the laser energy to compensate for the higher ionisation energy also does not help. The onset of laser-plasma instabilities at higher intensities decreases the laser coupling, resulting again in lower CEs [GR09]. Thus for line emission of high X-ray photon energy with a short pulse duration, $K\alpha$ sources are much more promising and will be described in the following.

Targets driven with fs to ps pulses can be used to efficiently excite $K\alpha$ emission without strong ionisation. In comparison with Heα sources, $K\alpha$ sources provide many favourable characteristics. First and foremost, the CEs are constant with increasing Z, leading to much higher photon energies when using the $K\alpha$ transition of for example Ag or Au [Par+06]. Secondly, the CEs are nearly constant with laser intensities above $10^{18}\,\mathrm{W\,cm^{-2}}$ [Par+06]. Both these characteristics are explained by the changed excitation mechanism, relying on the efficient generation of a hot electron distribution with high intensities. The hot electrons reflux multiple times through the target, interacting repeatedly with the atoms before they are stopped. While the hot electron temperature steadily increases with intensity, the hot electron losses also increases, limiting the increase of CEs beyond $10^{18}\,\mathrm{W\,cm^{-2}}$ [Neu+10]. The hot electrons also have energies much larger than the typical binding energy of K-shell electrons. Thus, the actual binding energy, which increases with Z, does not matter much and the CEs stay constant [Par+06]. The emission duration is strongly linked with the relaxation time of the hot electrons and in the range of 1 - $20\,\mathrm{ps}$ [Che+07], much shorter than typical Heα sources. Furthermore, a $K\alpha$ source lacks additional emission lines on the low energy side, as are observed with Heα sources. This decreased peak width has advantages, when doing scattering

[Che+07] Chen et al. (2007), "Fast-electron-relaxation measurement for laser-solid interaction at relativistic laser intensities".

experiments that rely on the observation of very small broadening or shifts of the photon energy towards lower energy [GR09]. While all these characteristics make $K\alpha$ sources favourable in many aspects, the overall yield is much smaller, reaching CEs of $10^{-5} \lesssim \eta \lesssim 10^{-4}$ [Par+06]. With the development of higher energy short pulse laser systems, this issue can be remedied somewhat. However, the laser-target coupling can also increase the efficiency. This is one aspect that is investigated in this thesis with the development of the targets described in chapter 4.

3.2 Atomic radiative simulations

With a basic understanding of the physics of X-ray generation, a tool to calculate a synthetic emission spectrum is described in the following. The goal is to reproduce the emission spectrum for a given plasma state which is defined by the thermodynamic parameters bulk electron temperature T_e and density n_e. Multiple components are needed to simulate this emission spectrum. As a brief overview, first the plasma state has to be defined and the atomic level population distribution derived from it. With this, the transition probabilities and energies can be determined. Using these quantities, finally the emissivity and opacity of the plasma is calculated, with which a synthetic spectrum is generated. The above-mentioned steps are discussed on the basis of the code FLYCHK [Chu+05]. For an in-depth discussion of the FLYCHK code, the reader is referenced to its manual [Chu+08].

The choice of a model is closely associated with the thermodynamic conditions. For low temperature with high densities, the radiative interaction can be neglected and a *local thermal equilibrium* (LTE) model might be sufficient. When the electron density is low but the temperature high, such as is the case in the corona region of the sun, a *coronal model* can be applied. In the case of a highly non-uniform laser plasma, which produces strong gradients, a *collisional-radiative* (CR) model offers the most general approach. This model is summarised in section 3.2.1. Once the atomic level population distribution has been calculated, it is used to generate the synthetic emission spectrum. How this is done is briefly sketched in section 3.2.2.

3.2.1 Collisional-radiative model

The state of a plasma is the result of the collisional and radiative processes occurring within it. The result of these processes can be expressed with rate equations, which rely on the knowledge of the probabilities for collisional and radiative interactions. The latter can only be determined if the radiation field is known. Thus, a radiation transport equation is needed as well. However, this radiation transport equation is dependent on the atomic level population. Therefore these equations need to be solved self-consistently. These two components of the CR model are described in the following sections.

In addition to the two major components, the CR model has some further capabilities. The inherent electric field of the plasma changes the ionisation potential and thus the level population. In particular can higher-lying energy levels be suppressed, leading to the so-called ionization potential depression (IPD). States that are determined to be suppressed are then excluded from the rate equation calculations. Furthermore, in many laboratory plasmas, the electron distribution function $f_e(E)$ is reasonably well approximated with a Maxwellian distribution. This is definitely not the case for plasmas produced during

[Chu+05] Chung et al. (2005), "FLYCHK: Generalized population kinetics and spectral model for rapid spectroscopic analysis for all elements".
[Chu+08] Chung et al. (2008), *FLYCHK Manual*.

the interaction with a high-power laser. To that end, the effects of non-thermal electrons on the population distributions are included in the model.

Rate equation

The processes which lead to a change of the atomic level are discussed in detail above and in the previous chapter (2 and 3). The change in density n_i of a specific atomic level i is calculated with

$$\frac{dn_i}{dt} = -n_i \sum_{i \neq j}^{N_L} W_{ij} + \sum_{j \neq i}^{N_L} n_j W_{ji} \qquad 1 \leq i \leq N_L, \tag{3.14}$$

where W_{ij} and W_{ji} are the probabilities for transitions into and out of the atomic level i, respectively. Each probability is simply the summation over all probabilities for each individual process. For clarity, W_{ij} is split into upward ($i < j$) and downward ($i > j$) transitions. Together with the electron density n_e and the frequency-averaged mean intensity relevant for the transition $\overline{J}$, W_{ij} is

$$\begin{aligned} W_{ij} &= W_{ij,i<j} + W_{ij,i>j} && \text{with} \\ W_{ij,i<j} &= B_{ij}\overline{J}_{ij} + n_e C_{ij} + \beta_{ij} + n_e \gamma_{ij} + \sigma_{ij} + I_{ij} && \text{and} \qquad (3.15) \\ W_{ij,i>j} &= A_{ji} + B_{ji}\overline{J}_{ji} + n_e D_{ji} + n_e \alpha_{ji}^{RR} + n_e \iota_{ji}^{EC} + n_e^2 \delta_{ji}. && \qquad (3.16) \end{aligned}$$

The rate coefficients are summarised in Tab. 3.1. In order to calculate the rate coefficients listed in Tab. 3.1, various models are implemented in FLYCHK [Chu+08]. Finally, the number of levels included in the calculation N_L has to be set. The highest level that should be considered is the highest still bound energy level. This can be estimated with, for example, continuum lowering models for each charge state [Cro14].

Table 3.1: Rate coefficients of the atomic processes relevant to an atomic level change.

charge state unchanged	charge state changed
A_{ji} spontaneous emission	α_{ji} radiative recombination
B_{ij} stimulated absorption ($i < j$) or emission ($i > j$)	β_{ij} photoionisation plus stimulated recombination
C_{ij} collisional excitation	γ_{ij} collisional ionisation
D_{ji} collisional deexcitation	δ_{ji} collisional recombination
I_{ij} beam and non-thermal electron collisions	ι_{ji} electron capture
	σ_{ij} autoionisation

It is however infeasible to solve the rate equation (3.14) for each energy level of each charge state of the investigated atom while it is influenced by the surrounding plasma. Rather, a small set of atomic term energy levels is used to estimate the rates of atomic processes that affect the level population as closely as possible. Such a set is constructed with tabulated values for ground states and computationally fast approximations for excited, inner-shell excited and doubly-excited states [Chu+08].

Radiation transport equation

Relevant for the formulation of the above-discussed rate equation is the frequency-averaged mean intensity $\overline{J}$. This intensity is dependent on the specific intensity $I(\vec{r}, \vec{n}, \nu, t)$ at position $\vec{r}$ in direction $\vec{n}$, which is

[Cro14] Crowley (2014), "Continuum lowering – A new perspective".

averaged over all solid angles and over the line profiler $\phi(\nu)$. $\overline{J}$ can then be written as

$$J(\vec{r},\nu,t) = \frac{1}{4\pi}\oint I(\vec{r},\vec{n},\nu,t)d\Omega \tag{3.17}$$

$$\overline{J}(z,\nu,t) = \int I(z,\nu,t)\phi(\nu)d\nu. \tag{3.18}$$

The radiation transport equation is used to determine this specific intensity $I(\vec{r},\vec{n},\nu,t)$. For simplicity, a one-dimensional, planar geometry along z is assumed and the time-dependence is neglected. The intensity $I(z,\nu)$ is only increased by the emissivity $\epsilon(z,\nu)$ and decreased by the absorption coefficient $\kappa(z,\nu)$, also called opacity. Therefore, the *radiation transport equation* is

$$\mu\frac{dI(z,\nu)}{dz} = \epsilon(z,\nu) - \kappa(z,\nu)I(z,\nu), \tag{3.19}$$

with $\mu = \cos(\Theta) = n_z$ the z-component of the direction $\vec{n}$. Both coefficients $\epsilon(z,\nu)$ and $\kappa(z,\nu)$ can be written as functions of the absorption coefficient for bound-bound, bound-free and free-free transitions. For a complete formulation, the reader is referred to the FLYCHK manual [Chu+08].

The radiation transport equation can be simplified with the definition of the *optical depth* $\tau(z,\nu)$. For a photon of frequency ν travelling along a line from z to z_{max}, $\tau(z,\nu)$ is the number of mean-free paths. Thus, $\tau(z,\nu)$ is

$$\tau(z,\nu) = \int_z^{z_{\text{max}}} \kappa(z',\nu)dz'. \tag{3.20}$$

As mentioned previously, if $\tau(z,\nu) \ll 1$ holds, the plasma is considered optically thin and the photon can escape. If $\tau(z,\nu) \gg 1$ holds, the plasma is optically thick and the photon would be reabsorbed. It is also useful to define the *source function* $S(z,\nu)$, which is the ratio of emissivity to opacity

$$S(z,\nu) = \frac{\epsilon(z,\nu)}{\kappa(z,\nu)}. \tag{3.21}$$

It can be understood as the intensity emitted over the length of one mean free path of the photon. With these two definitions, then radiation transport equation then reads in the optical depth scale

$$\mu\frac{dI(z,\nu)}{d\tau(z,\nu)} = S(z,\nu) - I(z,\nu). \tag{3.22}$$

Assuming for a moment that $S(z) = const.$, the solution to equation (3.22) is

$$I(\nu) = I_0 \exp^{-\tau(\nu)} + S(\nu)(1 - \exp^{-\tau(\nu)}). \tag{3.23}$$

This demonstrates, that for sufficient optical depth, the intensity $I(\nu)$ is only determined by the source function S. In general, this assumption cannot be made and the solution of equations (3.14) and (3.22) can only be done iteratively and with high computational cost.

To decrease this computational cost, a more efficient angle-averaged and frequency-averaged escape probability model is used [Mac93]. Instead of calculating a mean radiation field, the probability of a photon emitted in zone e to be absorbed in zone a is approximated. This probability, also called the zone coupling coefficient Q^{ea}, can be calculated from the angle-averaged and frequency-averaged escape probability $\bar{P}_e(\tau)$. This escape probability can be simplified to various analytical functions, depending on

[Mac93] MacFarlane (1993), *Collisional-Radiative Equilibrium (CRE) Model for the CONRAD Radiation-Hydrodynamics Code.*

the line shape (Gaussian, Lorentz or Voigt), and can even be extended to continuum radiation. Assuming an analytical representation of $\bar{P}_e(\tau)$, the zone coupling coefficient Q^{ea} is defined as

$$Q^{ea} = \frac{1}{2\tau_e} \int_0^{\tau_e} \left[\overline{P_e\left(\tau_b + \tau\right)} - \overline{P_e\left(\tau_b + \tau_a + \tau\right)} \right] d\tau. \tag{3.24}$$

Here, τ_e, τ_a and τ_b are the optical depths in the emitting zone e, absorption zone a and an intermediate zone b, through which the photon travels. The first term of the integral represents the probability of a photon emitted in zone e to reach zone a without being absorbed, while the second term represents the probability of a photon being absorbed before exiting zone a. The difference then is the probability of a photo exiting zone a.

With Q^{ea}, the stimulated absorption B_{ij} and emission coefficients B_{ji} from equations (3.15) and (3.16) can be expressed as

$$n_j^a B_{ji} \bar{J}_{ij} - n_i^a B_{ij} \bar{J}_{ij} = \begin{cases} -A_{ji} \sum_{e=1}^{N_D} n_j^e Q_{ji}^{ea} & (i < j) \\ A_{ij} \sum_{e=1}^{N_D} n_i^e Q_{ij}^{ea} & (i > j), \end{cases} \tag{3.25}$$

with n_i the population density of level i and N_D the number of spatial zones. This shifts the requirement of solving the radiation transfer equation to calculating the zone coupling coefficients, which can be done with analytical approximations and thus is computationally much faster.

3.2.2 Spectrum generation

Having solved the rate equations for a set of atomic levels, the atomic data and the population distribution is passed on to the code FLYSPEC. While the atomic data and in particular the radiative transition approximations are reasonably good to solve the rate equations, the same cannot be said when trying to generate the actual spectrum. Thus, a second iteration to generate a set of atomic data with relativistic configuration and more sophisticated oscillator strengths is deployed. This set is approximated with a Dirac-Hartree-Slater (DHS) atomic physics code, and the by FLYCHK calculated level population distribution is mapped onto the DHS configuration population distribution [Chu+05; Hua+76].

The next step is to calculate the emissivity $\epsilon(\nu)$ and the opacity $\kappa(\nu)$. These values are calculated as mentioned above for bound-bound, bound-free and free transitions, in dependence of the level populations and a line profile function $\phi(\nu)$. For the latter, a Voigt profile is used (see also section 3.1.2). The analytical expressions of these parameters are omitted here and can be found in the FLYCHK manual [Chu+08]. With $\epsilon(\nu)$ and $\kappa(\nu)$ the emitted radiation of a plasma slab of thickness L and with uniform temperature and density is estimated with equation (3.23). Assuming no external radiation field ($I(0) = 0$), the emitted intensity is

$$I(\nu) = S(\nu)\left(1 - \exp\left(-\tau_\nu\right)\right) \quad \text{with} \tag{3.26}$$

$$\tau(\nu) = \kappa(\nu) L. \tag{3.27}$$

One major limitation of the spectrum generation is the limitations of the atomic data. In order to keep the computational cost of such a code manageable, only a decreased subset of the atomic configurations is calculated. This can lead to incorrect calculations of line positions and intensities. In particular for

[Hua+76] Huang et al. (1976), "Neutral-atom electron binding energies from relaxed-orbital relativistic Hartree-Fock-Slater calculations for Z between 2 and 106".

weakly ionised atoms, the amount of possible electron configurations quickly exceeds the amount that can reasonably be calculated.

An example from the FLYCHK manual is here reproduced for clarity [Chu+08]. For ions with 4 or more bound electrons, the calculated transitions are based on a super-configuration model. A super-configuration describes all possible configurations of a given distribution of the electrons into atomic shells. The super-configuration transition array (STA) model then collects all possible transitions between those configurations [Bar+89]. As an example, for an transition from $K_2L_2M_1$ to K_2L_3, the STA describes the 6 possible lines: 3s$\rightarrow$ 2p$^-$, 3s$\rightarrow$ 2p$^+$, 3p$^+$ $\rightarrow$ 2s, 3p$^-$ $\rightarrow$ 2s, 3d$^+$ $\rightarrow$ 2p$^-$ and 3d$^-$ $\rightarrow$ 2p$^+$. Each of these lines can then be further split by relativistic configurations, which take into account the remaining electrons, in case of the above example the two *K*-shell and two *L*-shell electrons. This is called the unresolved transition array (UTA) [BBK88], and the corresponding UTA line centers and widths are calculated in FLYCHK with the JJATOM code [Che+79]. For the spectrum generation, the STA lines are listed for super-configurations up to n$=6$. For n>6, there are too many UTA lines to compute and the STA line itself is used to estimate the emission. Overall, this approach shows good agreement with measured data. It can however lead to uncertainties with respect to line position, width and intensity when configurations are neglected, in particular in weakly ionised, heavy ions. The STA model also only includes natural and Doppler broadening, but no Stark broadening, which can lead to false line widths.

With the here described models, an emission spectrum can be calculated for a given electron temperature T_e and density n_e. A collection of spectra for varying T_e and n_e can be used to analyse experimentally obtained spectra. Such an analysis can be done by for example comparing the shapes of the spectra or the ratio of specific lines. The method used in this thesis is described in section 6.3.1. How an experimental spectrum is obtained is discussed in the now following section.

3.3 X-ray spectrometer

The measurement of X-ray radiation in the harsh environment of a short pulse laser-plasma interaction poses a special challenge. To study the experimentally achieved conditions, high-resolution X-ray spectra are needed, which can resolve shifts and broadening of the observed characteristic line emission. Additionally, this line emission from bound-bound states is overlapped with the free-free and free-bound continuum, as well as scattered and fluorescence radiation and further background from the reaction of accelerated particles. As such, a high collection efficiency of the spectrometer is of equal importance. These two requirements for a high-quality X-ray spectrum can be achieved with crystal spectrometers.

In principle, this type of spectrometer relies on the constructive interference of the X-ray radiation from different lattice planes in a high-quality crystal. Using different crystals, a large energy range ΔE of about 0.25 - $100\,\mathrm{keV}$ can be covered, depending on the lattice plane used for the diffraction and the corresponding lattice spacing d. In the following section 3.3.1, the basic characteristics of the diffraction from a single crystal, the influence of shaping a crystal to non-planar surfaces and the characteristics of a mosaic crystal will be discussed. Various concepts with different crystals, crystal shapes and positions have been

[Bar+89] Bar-Shalom et al. (1989), "Super-transition-arrays: A model for the spectral analysis of hot, dense plasma".
[BBK88] Bauche et al. (1988), "Unresolved transition arrays".
[Che+79] Chen et al. (1979), "Relativistic L-shell Auger and Coster-Kronig rates and fluorescence yields".

studied [Sto+04; Leg+09; Gam+11; Yua+11; Hol+17] and an overview over the main layouts will be given in section 3.3.2. The last section 3.3.3 will discuss different methods of X-ray detection, with a focus on the IP used during this thesis.

3.3.1 Crystals

A crystal is defined by its unit cell, which describes the repeating pattern of atomic positions in the lattice. The principle shape of the unit cell can be described by the length of basis vectors $\vec{a_1}$, $\vec{a_2}$ and $\vec{a_3}$ and the corresponding angles α, β and γ between them. There are 14 different lattice types, called Bravais lattices. The most basic is the cubic lattice ($a_1 = a_2 = a_3$ and $\alpha = \beta = \gamma = 90°$, called primitive cubic), which can have additional atoms at each cubic face (face-centered cubic (fcc)) or at the cubic center (body-centered cubic (bcc)). A macroscopic crystal is then constructed from periodic repetition of these unit cells in all spatial directions. As an example, germanium (Ge) has a diamond cubic lattice, characterised by two fcc unit cells, with one cell shifted by $1/4$ in each direction. Such a diamond cubic lattice is displayed in figure 3.7.

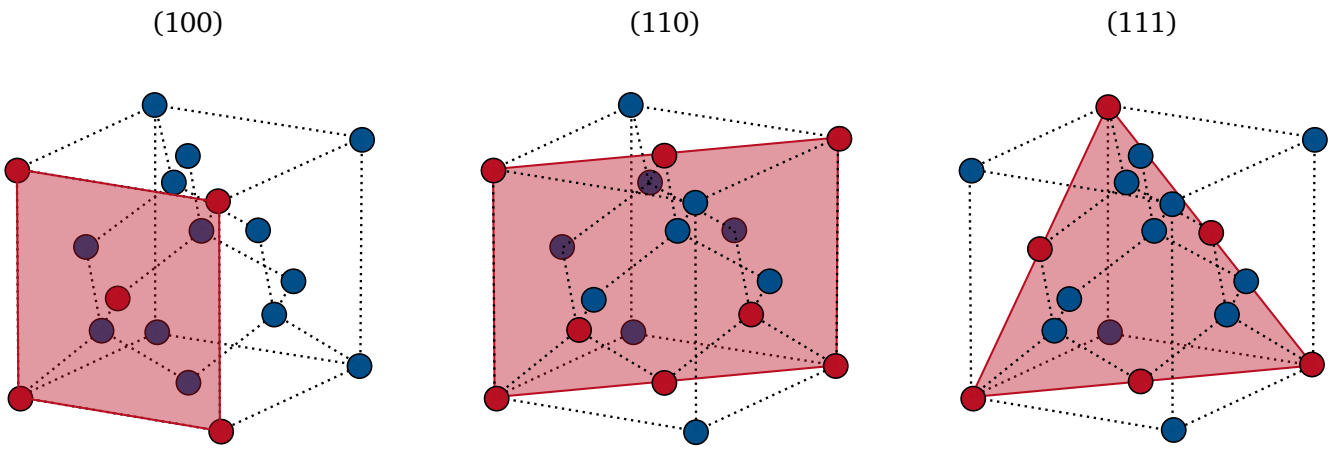

Figure 3.7: Crystal planes of a diamond cubic lattice.

Each crystal lattice possesses crystal planes. These planes are described by the Miller indices h, k and l with $h\vec{b_1} + k\vec{b_2} + l\vec{b_3}$, where $\vec{b_i}$ are the basis vectors of the reciprocal lattice. Converted to the direct lattice $\vec{a_i}$ introduced above, the indices can be understood as inverse intercepts along $\vec{a_i}$. Three exemplary planes are shown in figure 3.7 for a cubic lattice, in which case the Miller indices can also be interpreted as the planes normal vector. Owing to the periodic nature of a crystal, planes with the same Miller indices exist with a spacing d_{hkl}, forming a group of planes denoted by (hkl). For a cubic lattice, this spacing can be described by the lattice constant a with

$$d_{hkl} = \frac{a}{\sqrt{h^2 + k^2 + l^2}}. \tag{3.28}$$

[Sto+04] Stoeckl et al. (2004), "Operation of a single-photon–counting x-ray charge-coupled device camera spectrometer in a petawatt environment".
[Leg+09] Legall et al. (2009), "An efficient X-ray spectrometer based on thin mosaic crystal films and its application in various fields of X-ray spectroscopy".
[Gam+11] Gamboa et al. (2011), "Imaging X-ray crystal spectrometer for laser-produced plasmas".
[Yua+11] Yuan et al. (2011), "Spatially resolved X-ray spectroscopy using a flat HOPG crystal".
[Hol+17] Holden et al. (2017), "A compact dispersive refocusing Rowland circle X-ray emission spectrometer for laboratory, synchrotron, and XFEL applications".

While it is common to write the Miller indices in lowest terms, higher numbers are sometimes used to indicate crystal planes with a higher periodicity, even if not all planes are equally occupied. In the case of a Ge crystal, the lattice constant has been found to be $a_{\mathrm{Ge}} = (5.657\,35 \pm 0.000\,05)\,\text{Å}$ [Mac58]. With this, the spacing of planes along the (220) direction can be calculated to be $2.00\,\text{Å}$.

The diffraction of radiation from a crystal lattice can be thought of as the reflection from a crystal plane, if the wavelength of the radiation is of the order of the crystal spacing d. This is the case for X-ray radiation. Parallel X-ray radiation, impinging on a crystal plane, is diffracted from the electronic shell of the atoms, with each atom emitting a secondary wave. Following the principle of Huygens, these secondary waves result in the reflected wave. As only a small part of the radiation is absorbed over the distance d, the same behaviour is found at the following crystal planes, each generating a reflected wave [Dem16]. The reflected waves interfere constructive, if the phase shift matches 2π. The condition for constructive interference is described by Bragg's law:

$$n\lambda = 2d\sin\left(\Theta_{\mathrm{B}}\right). \tag{3.29}$$

This can easily be explained with figure 3.8. For parallel radiation with wavelength λ, impinging on a lattice with spacing d, a diffraction maximum occurs if the path length difference $2d\sin\left(\Theta_{\mathrm{B}}\right)$ is equal to an integer multiple of the wavelength. The corresponding angle is known as the Bragg angle Θ_{B}. In the case of a Ge crystal cut along the (220) plane, this corresponds to a Bragg angle at $E = 8.05\,\mathrm{keV}$ of $\Theta_{\mathrm{B}} = 22.65°$.

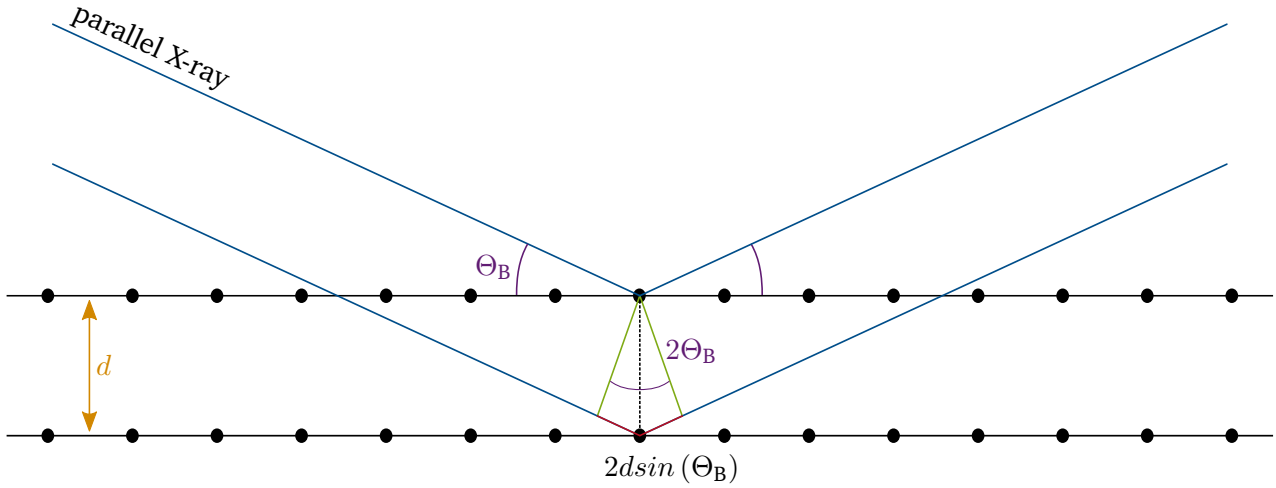

Figure 3.8: Schematic of the Bragg diffraction. Parallel radiation impinges on the crystal plane under angle Θ_{B}. This leads to a phase shift of $2d\sin\left(\Theta_{\mathrm{B}}\right)$ between the reflected rays.

In principle, the diffraction of a monochromatic X-ray beam should be a δ-function. In practice, X-rays do not strictly follow Bragg's law. Owing to crystal composition, defects and macroscopic shape, X-rays with a given energy are diffracted from a small range of angles around Θ_{B}. This behaviour of a crystal is studied by diffracting a monochromatic X-ray beam with intensity I_0 and observing the reflected intensity I for different angles. As the crystal is rotated around Θ_{B} in a rocking motion during the measurement, the resulting reflection behaviour I/I_0 is called a *rocking curve*. For a specific crystal, it depends not only on the wavelength of the diffracted radiation but also on the incident polarisation and the quality of the crystal. It is also changed when the crystal is bent [HWF98]. In figure 3.9, the dependence of the rocking

[Mac58] Mack (1958), "Präzisionsmessung der Gitterkonstante an Germanium-Einkristallen nach Kossel und van Bergen".
[HWF98] Hölzer et al. (1998), "Characterization of Flat and Bent Crystals for X-ray Spectroscopy and Imaging".

curve on the geometric shape of the crystal is displayed. A flat crystal exhibits the expected narrow peak. Integrating over the peak is a measure of the crystals performance, called the integrated reflectivity R_{int} for a specific energy. Bending the crystal out of its flat shape distorts the crystal lattice and leads to a change in the reflection behaviour. As an example, bending a crystal onto a sphere decreases the peak intensity while increasing the peak width, resulting in a larger R_{int}. Furthermore, if the crystal is strongly bend to a smaller radius, these effects also increase, leading to a very wide angular range with a small intensity. The R_{int} however stays roughly the same between the two bent cases. Overall, typical values for R_{int} range between 1 - $100\,\mu\text{rad}$ [HWF98; ZF14].

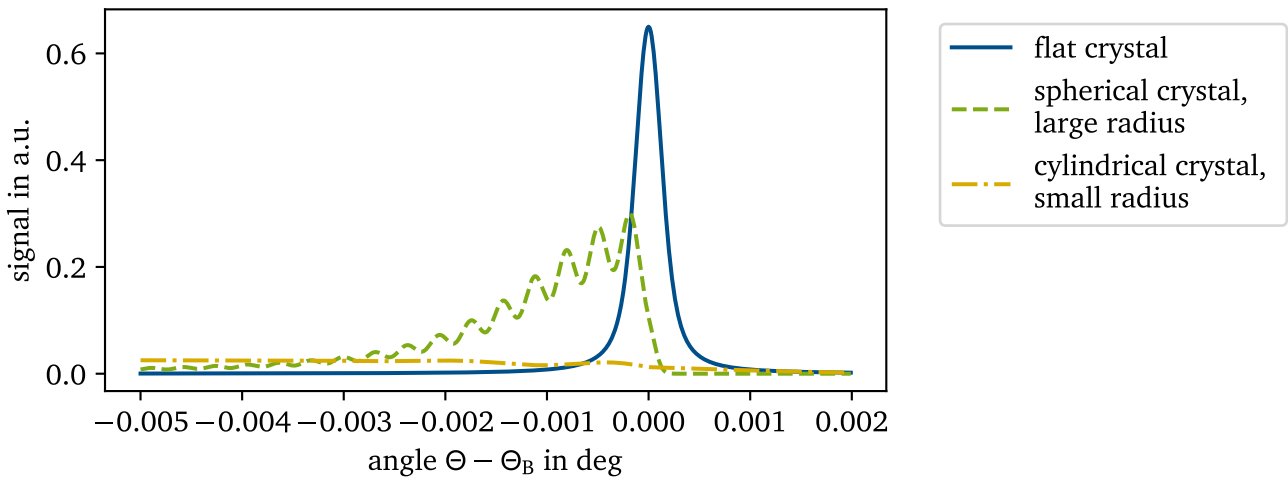

Figure 3.9: Rocking curve for three differently shaped crystals. For a flat crystal, the rocking curve can be estimated with a Voigt function. The influence of bending crystals into spherical and cylindrical shapes is sketched. The angular spread increases due to crystal defects, introduced during the bending. For smaller bending radii, the effect is developed stronger.

Much larger R_{int}, albeit with a smaller spectral resolution, can be achieved with *mosaic* crystals. These crystals exhibit a higher degree of imperfection and can be thought of a small crystallites oriented along different axes. Bragg's law can be met for many different incident angles on the macroscopic crystal surface from these randomly oriented crystallites. A measure for the spread of alignment of these crystallites is the mosaicity of the crystal, which is usually much higher than the width of the rocking curve for a single crystal. This results in an increase of R_{int}, which can be orders of magnitude larger. Furthermore, if the source and detector are positioned at the same distance from the crystal, an effect called mosaic focusing (or parafocusing) can be observed [San+98; Leg+09]. This effect is displayed in figure 3.10. For radiation emitted at a source point S, positioned at a distance $F = d_{\text{SC}}$ from the crystal, rays with different angles can be reflected with the same Bragg angle if the crystallites are oriented along a circle with radius $r_{\text{RC}} = F cos\,(\Theta_{\text{B}})$. The reflected rays are focused at a point D, if the distance between source to crystal d_{SC} and crystal to detector d_{CD} are equal. The enclosing circle is called the Rowland circle. It should also be mentioned that the angular spread of the crystallites lead to a defocus in non-dispersive direction, limiting the applications of mosaic crystal for imaging spectrometer as described in the following section 3.3.2 [San+98].

[ZF14] Zastrau and Förster (2014), "Integrated reflectivity measurements of hydrogen phthalate crystals for high-resolution soft x-ray spectroscopy".
[San+98] Sanchez del Rio et al. (1998), "Focusing properties of mosaic crystals".

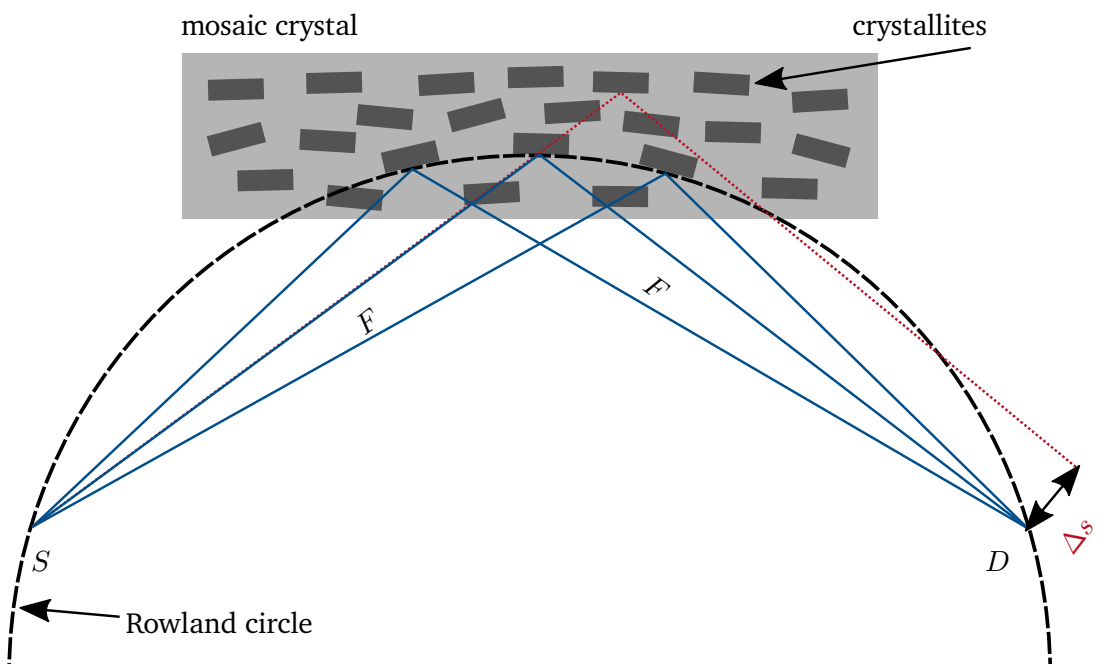

Figure 3.10: Schematic of the reflection principle for a mosaic crystal. The radiation is reflected from small crystallites, that are distribution in the mosaic crystal with some angular spread. Due to this spread, crystallites aligned along the Rowland circle lead to the same reflection angle and thus the same energy. This radiation is focused back onto the Rowland circle at point D. Reflections from crystallites not on the Rowland circle are the main reason for the relatively wide point spread function (PSF) of mosaic crystals (see section 5.3).

Another advantage of a mosaic crystal is the fact, that bending does not influence the small crystallites much. As such, almost arbitrary shapes can be realised with similar reflection properties. One commonly used mosaic crystal is the highly oriented pyrolytic graphite (HOPG), first developed in the 1960s [BU64]. Pyrolytic graphite is a synthetic material, which forms small crystallites with varying degrees of rotation. Through high temperature annealing of pyrolytic graphite at 3000 - $3300\,\mathrm{K}$, the crystallites can be oriented, producing a well defined mosaicity between 0.4 - $3.5°$.

3.3.2 Spectrometer layouts

The geometrically simplest crystal spectrometer can be realised with a flat diffraction crystal. The principle setup is displayed in figure 3.11, where the reflection follows Bragg's law. The spectrometer is then defined by the distance F from a point-like source S to the crystal center C. This distance determines the angular spread achievable for a crystal with a given length l. As a trade-off, a larger angular spread increases the spectral range, while decreasing the spectral resolution. As an example, these two values are plotted in figure 3.11 over F for a crystal with length $l = 50\,\mathrm{mm}$. As the rocking curve of a flat single crystal is very

[BU64] Blackman and Ubbelohde (1964), "Stress recrystallization of pyrolytic graphite".

narrow, this type of spectrometer offers a very limited collection efficiency. Furthermore, each energy is represented on the detector by a line in non-dispersive direction, which is limited either by the crystal or detector width, but gives no indication of the spatial extend of the source. Quite the contrary, a large source produces a larger angular spread than the rocking curve, decreasing the spectral resolution further. Attention should also be paid to the crystal homogeneity. Different reflection efficiencies over the surface area lead to varying signal strengths, an effect called flat fielding, which can produce inhomogeneous line profiles and false line ratios. A special case is a flat mosaic crystal, which can increase the collection efficiency and spectral resolution through mosaic focusing as described in the previous section. This constrains the spectrometer to have the same distances between source-crystal and crystal-detector.

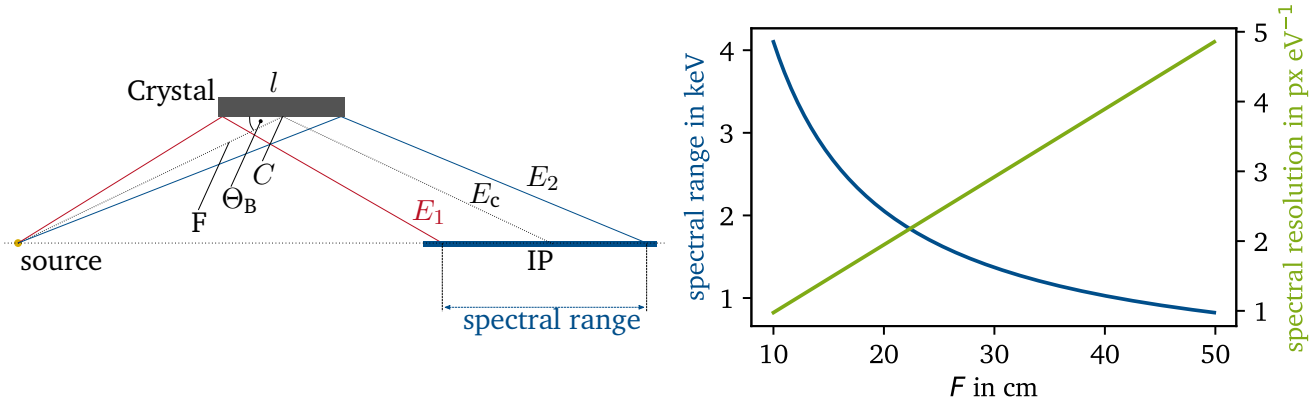

Figure 3.11: Layout of a flat crystal spectrometer (left) with the resulting spectral range and resolution over F (right). The spectrometer is defined by the distance $F = d_{\mathrm{SC}} = d_{\mathrm{CD}}$, measured to the center C of the crystal, together with the angle Θ_{B}. The length l of the crystal then determines the spectral range, that can be achieved. Assuming a constant vertical distance, the spectral range in dependence of F is plotted in blue. For smaller spectral ranges, the resolution of the spectrometer increases (green).

Much higher collection efficiencies can be achieved with 1D bent crystals, with a common setup for cylindrically bent crystals being the *von Hamos* spectrometer (see figure 3.12). The crystal is positioned such, that the source and detector lie on the central axis of curvature. Radiation emitted from the source is then diffracted from a circular arc on the cylindrical surface and focused back onto the axis at a distance $x = 2r_{\mathrm{RoC}}/\tan(\Theta_{\mathrm{B}})$, where r_{RoC} is the radius of curvature. The focusing in spatial direction greatly increases the signal-to-noise ratio on the detector, allowing for the observation of fainter transition lines. Mosaic crystals are commonly used for this type of spectrometer. The crystals can be shaped almost arbitrarily without effects on the rocking curve. Furthermore, the condition for mosaic focussing is automatically met with fulfilling the conditions of the von Hamos setup. The drawback of using a mosaic crystal is a limited spatial resolution, due to the mosaic spread in spatial direction.

As the detector is placed along the central axis of the cylinder of curvature, the diffracted radiation impinges on the detector under the Bragg angle Θ_{B}. This angle can be very shallow (in the case of a HOPG crystal, $\Theta_{\mathrm{B}} = 13.72°$ for the Cu $K\alpha$), requiring a long detector area. As a trade-off, the detector can be rotated to normal incident for one energy E_0. This can be done if the investigated spectral range is small, considerably decreasing the required detector length but energies $E \neq E_0$ are increasingly out of focus [Leg+09]. One can also use conically shaped crystals, which use the continuously changing radius to focus multiple energies onto a plane perpendicular to the cone surface. This type of spectrometer is commonly used when the active detector area is strongly limited.

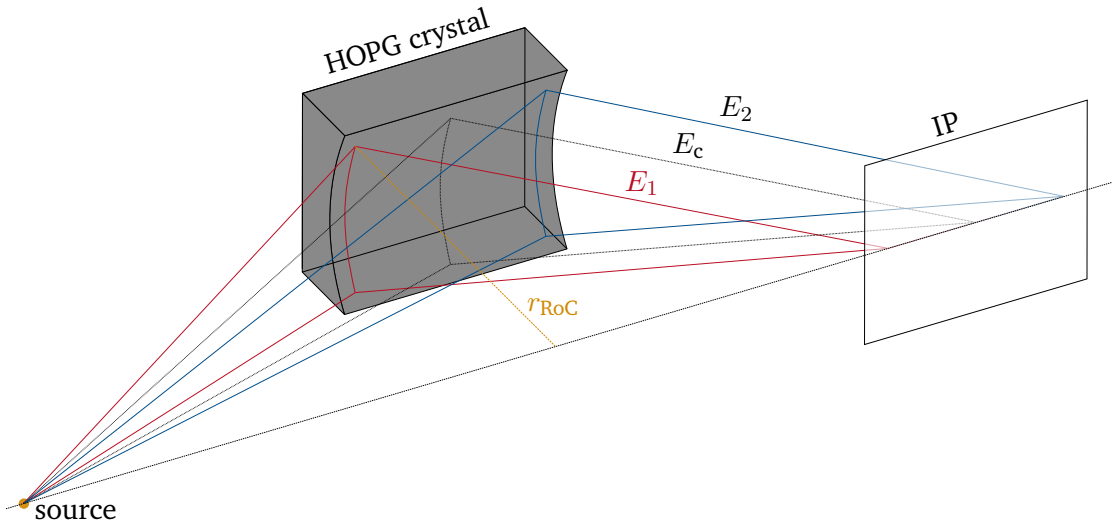

Figure 3.12: Layout of a *von Hamos* spectrometer. The setup is defined by the radius of curvature R of the cylindrical crystal. The source and the detector are placed on the central axis of this cylinder. As a result, the reflected rays are focus back onto the central axis, resulting in a much higher signal to noise ratio on the detector.

The alternative setup for a 1D bent crystal is the *Johann* spectrometer [Joh31]. Here, the curvature of the crystal follows the dispersive direction. The diffraction properties can then be explained with the help of the Rowland circle, as displayed in figure 3.13. The radius r_{RC} of the Rowland circle is here half the radius of curvature r_{RoC} of the crystal. Rays emitted from a point-like, monochromatic source positioned on the circle on point S are focused back onto the circle at point D. A small astigmatism occurs in this setup, as the curvature of the crystal does not follow the curvature of the Rowland circle, called the Johann error. This has been addressed with a modified crystal shape, which is first bent to some r_{RoC} and then ground down to the corresponding r_{RC} [Joh33]. In theory, this should remedy the astigmatism. In practice however, additional damages of the crystal are produced during the grinding process, resulting in further focusing errors.
Besides the Johann error, a crystal set up in the described way would work as a monochromator, diffracting only one energy. For a polychromatic setup, moving the source away from the Rowland circle is required. Two cases emerge, which are displayed in figure 3.13 [Hol+17]. For a source inside of the Rowland circle and a detector tangent to point D, the observed diffraction is very similar to that of a flat crystal described above. Positioning the source outside of the Rowland circle also enables a polychromatic dispersion. The diffracted rays cross over inside the Rowland circle at the meridional focus. A slit at this point can greatly reduce background radiation. Again, a detector tangent to point D allows for the observation of the spectrum.

The last family of spectrometers that should be mentioned here are *imaging* spectrometer. These use 2D bent crystals and can be set up either in monochromatic mode to image the source in 2 dimensions or to combine a spectral dispersion with a 1D spatial resolution. This second type of spectrometer for simultaneous spectral and spatial resolution can be understood from figure 3.14. The crystal is defined by

[Joh31] Johann (1931), "Die Erzeugung lichtstarker Röntgenspektren mit Hilfe von Konkavkristallen".
[Joh33] Johansson (1933), "Über ein neuartiges, genau fokussierendes Röntgenspektrometer - Erste Mitteilung".

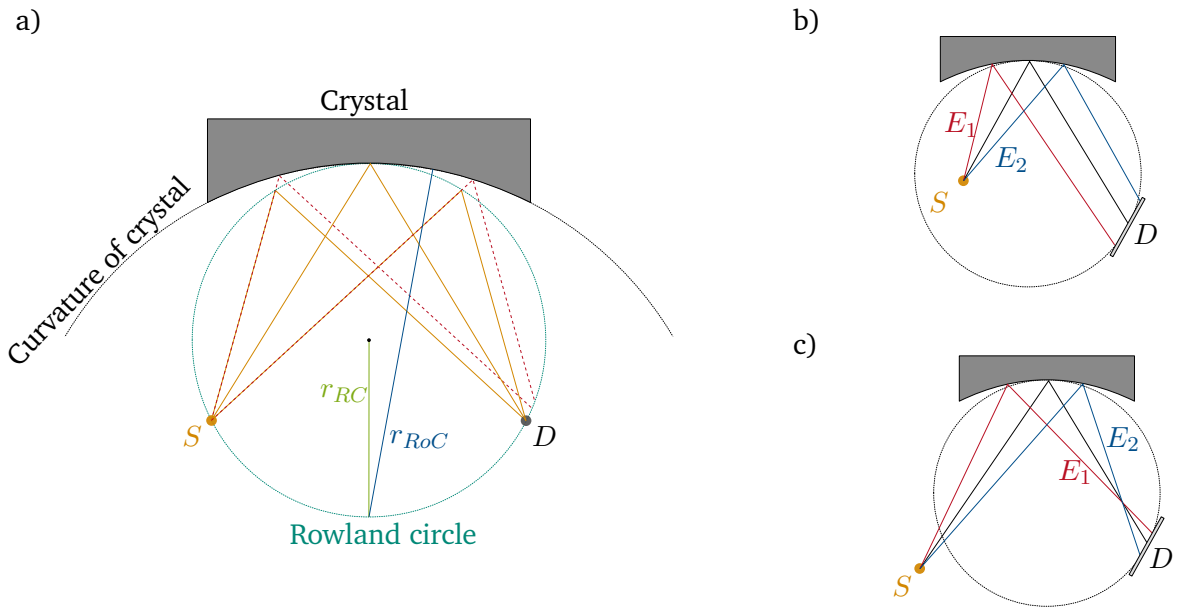

Figure 3.13: Schematic of a *Johann* type spectrometer layout (a) with two additional cases of different source positions ((b) and (c)). For a source S placed on the Rowland circle with radius r_{RC}, the reflected rays are collected at point D. A focusing error occurs due to the miss-match of r_{RC} to the radius of curvature of the crystal r_{RoC}. If the source is placed inside of the Rowland circle (b), the reflection is very similar to that of a flat crystal spectrometer. If the source is placed outside of the Rowland cicle (c), a polychromatic crossover (meridional focus) exists.

the radii in horizontal (r_{h}) and vertical (r_{v}) plane and posses two foci described by

$$f_{\mathrm{h}} = \frac{r_{\mathrm{h}} \sin(\Theta)}{2} \qquad \text{and} \tag{3.30}$$

$$f_{\mathrm{v}} = \frac{r_{\mathrm{v}}}{2\sin(\Theta)}. \tag{3.31}$$

The spectral reflection follows the principle of a Johann type spectrometer described above along the horizontal plane and as mentioned there, the detector should be placed close to $D = r_{\mathrm{h}} * \sin(\Theta_{\mathrm{B}})$ for the best spectral resolution. The source is then placed according to the mirror equation $1/d_{\mathrm{SC}} + 1/d_{\mathrm{CD}} = 1/f_{\mathrm{h,v}}$ at

$$S = \frac{r_{\mathrm{h}} r_{\mathrm{v}} \sin(\Theta)}{2 r_{\mathrm{h}} \sin^2(\Theta) - r_{\mathrm{v}}} \tag{3.32}$$

This equation exposes the limitations of using a spherical bent crystal in such a spectrometer. While spherical crystals are relatively cheap to produce, condition 3.32 can only be fulfilled for Bragg angles $\Theta_{\mathrm{B}} > 45°$ [RR19]. A more flexible setup can be realised with toroidal crystal, which fulfil condition 3.32 for

$$\frac{r_{\mathrm{v}}}{r_{\mathrm{h}}} = \sin^2(\Theta). \tag{3.33}$$

These crystals are however much more expensive and when reusing a crystal with non-optimal radii for a given Bragg angle, a trade-off between spectral and spatial focussing has to be made [RR19]. An in-depth

[RR19] Renner and Rosmej (2019), "Challenges of x-ray spectroscopy in investigations of matter under extreme conditions".

analysis of the reflection properties of a toroidally curved imaging spectrometer can be found for example in the work of Gamboa *et al.* [Gam+11].

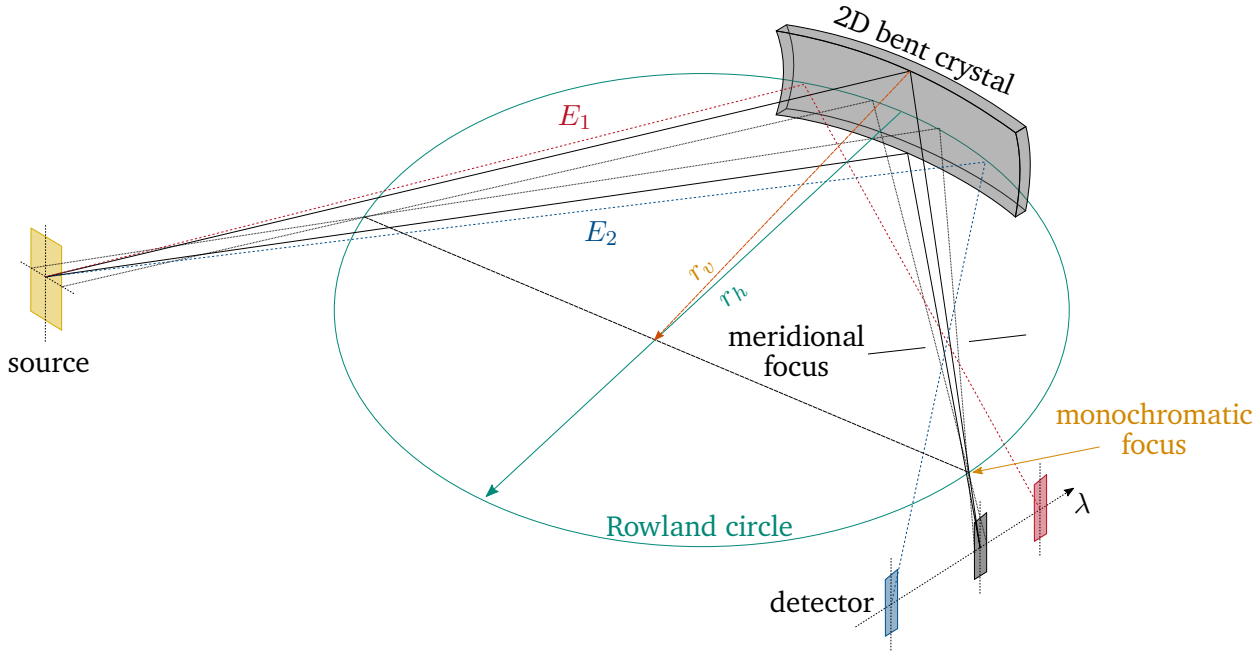

Figure 3.14: Schematic of an imaging spectrometer layout. The spectral dispersion follows the principle of a *Johann* type spectrometer. The vertical radius r_v leads to a monochromatic focus on the Rowland circle. If the detector is offset, the size of the source can be inferred in one dimension, perpendicular to the spectral resolution.

3.3.3 X-ray detection

Historically, X-ray radiation from laser-plasma sources was recorded with X-ray films, multi-channel plates (MCPs) and charge-coupled device (CCD) cameras [Bat77; How+06]. Many characteristics of the X-ray film have made it the primary detector of X-ray emission in laser-plasma experiments. They provide a high spatial resolution, reliability and flexibility in application, low cost and the response has been well studied for a wide range of photon energies [Hen+84b; Hen+84a; Tal+97]. However, each film has to be developed after exposure, which can introduce errors from the development process and limit the effective laser shot cycle if the information is needed quickly, as is the case during the alignment of a diagnostic [How+06]. X-ray films are also single use and its quality can deteriorate with age. As a result, where possible, X-ray films have been replaced with CCD cameras [How+06]. These possess a high detection efficiency and linearity for photons below $10\,\mathrm{keV}$, reaching quantum efficiencies of up to 90 - $100\,\%$ [GR09]. For temporal analysis of the X-ray emission, CCD cameras in combination with gated MCPs, for time resolutions of 30 - $40\,\mathrm{ps}$, or

[Bat77] Bateman (1977), "The detection of hard X-rays (10–140 keV) by channel plate electron multipliers".
[How+06] Howe et al. (2006), "Comparison of film detectors, charged-coupled devices, and imaging plates in x-ray spectroscopy of hot dense plasma".
[Hen+84b] Henke et al. (1984), "Low-energy x-ray response of photographic films. I. Mathematical models".
[Hen+84a] Henke et al. (1984), "Low-energy x-ray response of photographic films. II. Experimental characterization".
[Tal+97] Tallents et al. (1997), "Film calibration for soft x-ray wavelengths".

sweeping units for streaked images, with a resolution in the range of ps, have been developed [MKF90; Bra+92; Bra+95]. In addition, data acquisition is nearly instantaneous. However, the quantum efficiency of CCD chips drops with increasing energy, reaching negligible levels for photon energies above 20 - $30\,\mathrm{keV}$. Additionally, strong electromagnetic pulses (EMPs) are common during high intensity, short pulse laser matter interactions. An EMP can interfere during the measurement, distorting the data, interrupt the data acquisition and even damage the electronic components, so special care has to be taken to shield the instrument. More recently, IPs have been used as a X-ray diagnostic [How+06; Izu+06]. Initially developed in the 1980s and successfully used in medical fields and experimental physics [Seg92; Ame95], IPs were first reported for X-ray imaging in laser-plasma experiments in the early 2000s [Fuj+03]. IPs possess many of the advantages of both film and CCD cameras. They have a good X-ray sensitivity up to 60 - $100\,\mathrm{keV}$, and surpass the sensitivity of CCD cameras for energies above $4\,\mathrm{keV}$ [MBS08; GR09]. In addition, IPs have a high dynamic range of 10^6 with a linear response [Ame95]. They can also be erased and reused after exposure. Consequently, IPs were chosen as the detector for all spectrometers used in this thesis. The working principle of an IP will be described in the following section.

Image plates

In principle, an IP is based on the generation of defects inside phosphor crystals during interaction with ionising radiation [Kol03]. These defects are metastable at normal conditions and can later be recombined through optical or thermal excitation to stimulate luminescence. The macroscopic structure of an IP is displayed in figure 3.15. The photostimulable phosphor crystals are suspended in an organic binder, which is layered on a polyester base for structural support [Izu+06; How+06]. A ferromagnetic backside layer is used for adherence to magnetic scanning trays. In addition, a Mylar layer on the top protects the IP. The most commonly used phosphor for IPs are crystallite alkaline earth metal halides, doped with bivalent europium (Eu), namely: $\mathrm{BaFBr{:}Eu^{2+}}$ and $\mathrm{BaFBr_{0.85}I_{0.15}{:}Eu^{2+}}$ [MBS08].

For this phosphor, the physical mechanism of storing is as follows. An electron is removed from an anion (F^-, Br^-, I^-) through irradiation and is trapped in the vacancy of a displaced anion in the crystal lattice. Similarly, the hole is trapped on a regular anion lattice position in close proximity to either a Ba^{2+} or Eu^{2+} ion and shares the electron of a neighbouring anion. As this defect absorbs light in the visual range, it is called an F-center (from the german *Farb-center*) [Seg92]. The defect can then be prompted to recombination in a process called photo-stimulated luminescence (PSL). For this, a $650\,\mathrm{nm}$ He-Ne laser is used to excite the trapped electron just below the conduction band. Here, the electron can either tunnel to a nearby hole or overcome the remaining energy difference to the conduction band through thermal activation and then move to a hole. The energy emitted during the recombination of the electron/hole-pair can then be resonantly absorbed by a Eu^{2+} ion, if one is in close proximity. This leads to the excitation of

[MKF90] Murnane et al. (1990), "X-ray streak camera with 2 ps response".
[Bra+92] Bradley et al. (1992), "High-speed gated x-ray imaging for ICF target experiments (invited)".
[Bra+95] Bradley et al. (1995), "Development and characterization of a pair of 30-40 ps x-ray framing cameras".
[Izu+06] Izumi et al. (2006), "Application of imaging plates to x-ray imaging and spectroscopy in laser plasma experiments (invited)".
[Seg92] Seggern (1992), "X-ray imaging with photostimulable phosphors".
[Ame95] Amemiya (1995), "Imaging Plates for Use with Synchrotron Radiation".
[Fuj+03] Fujioka et al. (2003), "First observation of density profile in directly laser-driven polystyrene targets for ablative Rayleigh-Taylor instability research".
[MBS08] Meadowcroft et al. (2008), "Evaluation of the sensitivity and fading characteristics of an image plate system for x-ray diagnostics".
[Kol03] Kolb (2003), "Synthese und Eigenschaften keramischer Neutronenbildplatten auf der Basis von BaFBr:Eu2+ und Gd-Verbindungen".

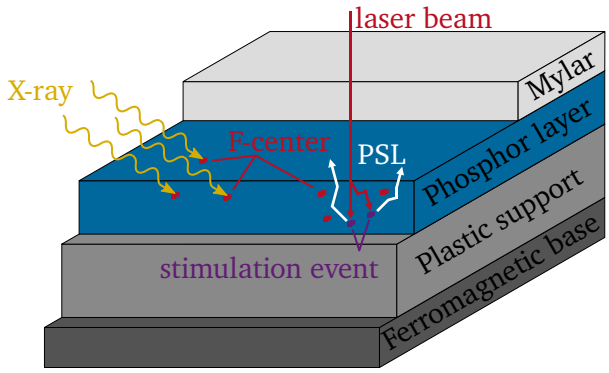

Figure 3.15: Schematic of an IP and the PSL process. X-ray radiation impinging on the phosphor layer create F-centers, thereby storing the information. Excitation of the F-center with a laser beam triggers a recombination process, resulting in the emission of PSL. In a typical IP, the phosphor layer is supported by a thicker plastic layer. For handling, a ferromagnetic base is often added. For some IP, a protective mylar layer is added as well. This layer can however influence the absorption behaviour, thereby making the IP less efficient for lower X-ray energies.

an Eu valence electron from the $4f^7$ to the 5d orbital [Kol03]. In turn, this excited state decays, emitting a photon with wavelength of $390\,\mathrm{nm}$. Research has shown, that for the phosphor discussed here, only $F(Br^-)$- and $F(I^-)$-center contribute to the PSL process [Seg92]. Two types of commercially available IPs were used during this thesis with slightly varying characteristics. The Fuji biological analysis system super resolution (BAS SR) is made with $BaFBr{:}Eu^{2+}$ and additionally doped with blue pigments [Izu+06]. The spatial resolution is limited during the readout due to scattering of the He-Ne laser in the phosphor layer. The blue pigmentation absorbs stray laser light, decreasing the spatial extent of the PSL [Izu+06]. The second type was the Fuji biological analysis system tritium (BAS TR), which is made with $BaFBr_{0.85}I_{0.15}{:}Eu^{2+}$ phosphor and is slightly stronger pigmented. In addition, no protective layer is applied as these IPs were originally designed for the low energy β-decay of tritium. The phosphor layer of the BAS TR IP is also only about half as thick as for the BAS SR IP, reducing the sensitivity [MBS08].

In practice, the 2D image is reconstructed by scanning the He-Ne laser over the IP and simultaneously recording the luminescence with a photo multiplier tube (PMT). The scanner then converts the recorded PMT signal into a gray scale image [Mad+11]. In order to obtain the signal S_{PSL} in units of PSL, this scanner specific conversion, which depends on various settings of the scanner during the readout, has to be reversed. For the commercially available Typhoon FLA 7000 IP scanner, the calibration is described by the following formula:

$$S_{\mathrm{PSL}} = \left(\frac{Res}{100\,\mu\mathrm{m}}\right)^2 * \left(\frac{4000}{S}\right) * 10^{L*\left(\frac{S_{\mathrm{gray}}}{G}-0.5\right)} \tag{3.34}$$

Here, S – gray is the scanned signal, Res describes the spatial resolution in $\mu\mathrm{m}$, S is the sensitivity of the PMT (either 1000, 4000 or $10\,000$), L the dynamic range latitude (4 or 5 orders of magnitude) and G the bit-depth of the gray scale image (8 or $16\,\mathrm{bit}$).

[Mad+11] Maddox et al. (2011), "High-energy x-ray backlighter spectrum measurements using calibrated image plates".

4 Target design and fabrication

The target concepts developed in the framework of this thesis are the subject of this chapter. Layered targets have seldom been used as direct X-ray backlighters and their advantages and limitations will be discussed in the first section 4.1. The actual manufacturing processes involved to fabricate the investigated targets is discussed in section 4.2 and an overview over the finished targets is given in section 4.3.

4.1 Overview of X-ray backlighter concepts

Various concepts are used to provide powerful and efficient X-ray backlighters for diagnosing high energy density (HED) experiments in the multi-keV range. In the beginning of the 21st century, gas targets and metallic foils are used. The former, albeit difficult to handle, provides very high conversion efficiencies (CEs) from laser energy to X-ray emission up to $20\,\%$ [Gir16]. Gas targets however are strongly limited in their spectral range, with no gases available for energies between 5 - $13\,\mathrm{keV}$, a relevant regime for probing HED states. For that reason, the focus remained with the mentioned metallic foils. Here, as discussed in section 3.1.5, a strong decrease of the CE into thermal line emission is observed with increasing Z materials, again limiting the usefulness of these sources for energies above approximately $10\,\mathrm{keV}$ [GR09]. With the much more common availability of higher intensities above $10^{18}\,\mathrm{W\,cm^{-2}}$, the $K\alpha$ emission of weakly ionised matter shows much promise.

Similar metallic targets are used to generate both the thermal line emission as well as the $K\alpha$ emission. A classical design is the simple foil target. Depending on the experimental configuration, the X-ray emission is then either used from the front or back side of the foil. Typically, the source size is well defined and not much larger than the laser spot for solid density targets [FK16] in contrast to larger emission volumes found for gas targets [Gir16]. The source size has however been further controlled through the target design. Wire targets, sometimes with the wire embedded into some substrate, or foil targets that are driven edge-on have demonstrated further reduction in the source size in one or multiple dimensions [Beg+97; Par+06; BKN19].

A further influence, that has been studied in regard to $K\alpha$ sources, is electron refluxing which is mainly dependent on the target thickness (see section 2.4.3). During the interaction with the high-intensity laser pulse, the laser energy is transferred to the electrons as discussed in section 2.3. For foil targets of a few $10\,\mathrm{micrometre}$ these energetic electrons have stopping ranges exceeding the target thickness multiple times. While initial electrons leave the target, the increasing space charge of the target promotes the recirculation of these electrons, the so-called electron refluxing. These electrons then interact with the

[FK16] Fourmaux and Kieffer (2016), "Laser-based K α X-ray emission characterization using a high contrast ratio and high-power laser system".
[Beg+97] Beg et al. (1997), "A study of picosecond laser–solid interactions up to 10 19 W cm -2".
[BKN19] Borm et al. (2019), "Properties of laser-driven hard x-ray sources over a wide range of laser intensities".

target matter through multiple passes, strongly increasing the CE of the target. In particular for higher intensities ($I_{\mathrm{L}} > 10^{17}\,\mathrm{W\,cm^{-2}}$), electron refluxing is the main driver of $K\alpha$ emission. At intensities above $10^{19}\,\mathrm{W\,cm^{-2}}$, approximately $95\,\%$ of the energy is carried by electrons with a continuous slowing down approximation (CSDA) of twice the target thickness or more [Nil+08; Neu+10]. This results in the requirement of targets that promote electron refluxing for efficient $K\alpha$ sources, i.e. a low thickness ($< 75\,\mu\mathrm{m}$) and limited overall mass. Also, embedding the source, for example a wire or layer, in some kind of substrate should be avoided [Neu+10].

Besides the investigation into the role of electron refluxing, the laser-target coupling has also been studied. As gas targets with densities below the critical density of the laser have shown very high CEs, the idea of under-dense targets made of non-gaseous materials was derived. For example, foam or aerogel targets doped with titanitum (Ti) or iron (Fe) were used to efficiently produce Heα emission [Pér+14]. Another approach uses a secondary pulse used to generate a large pre-plasma formation or even to pre-explode the complete foil target, which again provides an under-dense plasma for interaction with the main pulse [Gir16]. Though investigations have shown an increase of CE into $K\alpha$ for metallic foams as well [WLC18], any substantial pre-pulse decreases the efficiency of the $K\alpha$ source [Jar+14]. This is obvious, as these targets rely on the formation of a large volume of under-dense material, that can be quickly heated by the penetrating laser. The formation of high ionisation states is however detrimental to the emission of $K\alpha$ emission. On the contrary, efficient $K\alpha$ sources use high-contrast laser pulses (for the definition of laser contrast in the context of this work see sec. 5.2) to limit the exposure of the target and prevent any kind of substantial pre-plasma formation. Thus, a different approach is required to increase the efficiency of $K\alpha$ sources from a targets perspective and will be discussed in the following section.

4.1.1 Layered targets

Another approach to increase the CE of an X-ray backlighter target is the modification of the interaction surface. Similar to a foam target, a front surface comprised of nano-wire arrays shows great promise for both an increased laser absorption and a subsequent higher X-ray yield [Kul+00; Ye +13; Hab+16; Sam+18]. This is combined with an apparent decrease in plasma expansion in comparison to a flat foil, favouring the emission of $K\alpha$ over Heα. However, these structures are mainly used in lower energy laser pulses (10 - $100\,\mathrm{mJ}$ in $1\,\mathrm{ps}$ [Kul+00]; $4\,\mathrm{J}$ in $50\,\mathrm{fs}$ [Ye +13];20 - $30\,\mathrm{J}$ in $500\,\mathrm{fs}$ [Hab+16]; $3.5\,\mathrm{mJ}$ in $60\,\mathrm{fs}$ [Sam+18]), and these targets are believed to fall short for higher pulse energies of several $100\,\mathrm{J}$. The main reason for this is the small size of the nano-wires, in the range of a few $10\,\mathrm{nm}$ in diameter, which simply does not survive the ramp up of a full 200 - $500\,\mathrm{J}$ laser pulse and shifts the behaviour of the target to the previously mentioned foam targets.

Theoretical studies of larger front surface structures were based on these conclusions, namely pillars and cones in the range of 1 - $30\,\mu\mathrm{m}$ [Kli+11; Jia+14; Bla+17]. In particular, cones show great promise on many aspects of the laser-target interaction. Blanco *et al.* [Bla+17] showed a reduced laser reflectivity in particle-in-cell (PIC) simulations reaching up to $97\,\%$ absorption. A change of the electron distribution is observed as well, increasing the number of energetic electrons and exhibiting an almost isotropic angular distribution. In a publication by Ebert *et al.* [Ebe+20], similar structures to the ones described by the theoretical studies are investigated in an experiment for the first time. The predicted change of the electron distribution towards higher numbers was confirmed with a threefold increase of the measured electron flux [Ebe+20]. Related to the increased electron flux is an observed boost of the X-ray emission of 7

[Jar+14] Jarrott et al. (2014), "Kα and bremsstrahlung x-ray radiation backlighter sources from short pulse laser driven silver targets as a function of laser pre-pulse energy".

times over the measured spectral range between 1.7 - $1.85\,\mathrm{keV}$. This spectral range, much to low for many relevant probing experiments, is due to the material used to fabricate the cone-like microstructures, namely silicon (Si).

The question is, whether the advantage of these cone-like microstructures can be used to create efficient X-ray sources in a more relevant energy regime between 5 - $20\,\mathrm{keV}$. Targets could be fabricated from a more relevant material directly, a process which is investigated in a recent publication by Ebert *et al.* [Ebe+21]. However, the clear decoupling of the heated material, which would be subject to both $K\alpha$ and thermal line emission, and a weakly ionised (cold) material for pure $K\alpha$ emission appears appealing. The idea originates from so-called tracer layer or buried foil targets, which are a well established tool to investigate the electron distribution inside the target via *K*-shell spectroscopy [Che+09]. The heated target is highly non-uniform in temperature and density, making the distinction between the thermal and hot electron component difficult. Measurements by Theobald *et al.* [The+06] demonstrated however, that the heated area is strongly localised within a thin layer on the front side of the target (in the range of about $1\,\mu\mathrm{m}$). From this, the concept of a layered target similar to a buried foil target was derived and will be described in the following.

The target studied in this work is comprised of two layers. The laser-target interaction is optimised through the use of the previously mentioned cone-like microstructures, which constitute the first layer. The improved performance is used to offset the primary disadvantage of such a layered target, which is the decrease in efficiency due to the additional energy loss of the electrons in the front side layer. For the target investigated in this work, the first layer is fabricated from Si. The electrons accelerated from this optimised front surface then move into the second layer. Here, any material with a relevant $K\alpha$ transition could be used. For this work, copper (Cu) is chosen for various reasons. Primarily, Cu with a transition at $8\,\mathrm{keV}$ is of great interest for probing experiments, but already suffers from the decrease in Heα CE discussed in section 3.1.5. Nonetheless, Cu has been widely used for *K*-shell emission, both as a backlighter but also as a direct spectroscopic diagnostic, which enables to comparison of this proof-of-concept target with other studies. Cu is also comparatively easy to handle as it can be sputtered, electroplated and thermally evaporated. From this concept, a fabrication process was planned, which is described in the following section.

4.2 Fabrication

In order to fabricate the layered targets described above, two major fabrication steps are needed. These will be discussed in the following sections. Starting with a larger piece of a (100) Si wafer with a thickness of $50\,\mu\mathrm{m}$, smaller samples are laser-cut to roughly $5\mathrm{x}10\,\mathrm{mm}^2$. These samples are positioned in custom mounts for the formation of the Cu back side layer. This is described in section 4.2. With the back side layer in place, the samples are mounted on pins for the manufacturing of the microstructures (see section 4.2). Care is taken to not damage the back side layer during this step. After structuring, the samples are detached from the pins and All the targets were manufactured in the Detector and Target laboratory at the Technical University of Darmstadt by G. Schaumann, T. Abel and T. Ebert.

[Che+09] Chen et al. (2009), "X-ray spectroscopy of buried layer foils irradiated at laser intensities in excess of 1020 W/cm2".
[The+06] Theobald et al. (2006), "Hot surface ionic line emission and cold K-inner shell emission from petawatt-laser-irradiated Cu foil targets".

Back side layer

The back side layer has to be formed without any gaps between the two components of the target. A main motivation for this is the threat, that an air-filled gap could violently decompress during the pumping process of the target chamber, thereby destroying the target before the experiment. The ideal manufacturing techniques to deposit a metal layer are sputtering, electroplating or thermal evaporation. In all processes, a homogeneous layer with an highly controllable thickness can be deposited onto the sample. A deciding factor between these three techniques is the desired thickness of the layer. Sputtering is only feasible for very thin layers of a few nm, thermal evaporation can deposit thicker layers up to a few $\mu\mathrm{m}$ and electroplating is commonly used for layers in the range of 0.1 - $100\,\mu\mathrm{m}$. For the targets investigated in this work, thermal evaporation was chosen to fabricate the back side layer.

Thermal evaporation works as follows. The sample is placed in a vacuum chamber together with the Cu to be evaporated. The Cu is stored in a container, often called *boat* for its shape. The whole container can then be heated, in this case through resistance heating with a strong current. This melts the Cu and subsequently evaporation occurs. The evaporated Cu then expands into the space above the boat. The sample is placed above the boat, such that the expanding Cu reaches the sample. There, the evaporated Cu condenses on the cold surface of the sample into an homogeneous layer. A schematic of a typical thermal evaporation system is displayed in figure 4.1.

Important for both the purity and homogeneity of the deposited Cu layer is the quality of the vacuum in the processing chamber. The vacuum increases the mean free path of the evaporated Cu atoms and decreases the chance for interaction with residual air molecules, which could lead to oxidation of the Cu before or during condensation. For that reason, an oil diffusion pump is used to create a vacuum of up to $10^{-7}\,\mathrm{mbar}$. Secondly, the layer thickness has to be characterised during the deposition process. This is done with a calibrated quartz oscillator, whose resonant frequency changes depending on the amount of Cu deposited.

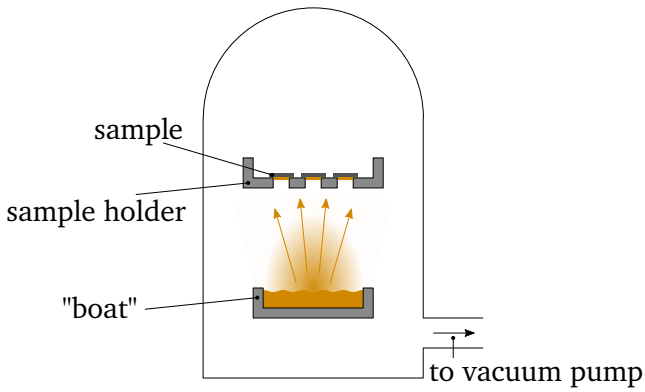

Figure 4.1: Schematic of the thermal evaporation process. The samples are positioned in the sample holder, which is positioned above the material container, also called „boat“. The material is evaporated through resistance heating. The evaporated material condenses on the cold samples, building the desired secondary layer of the target.

Laser-induced microstructures

The formation of microstructures in Si is based on a process first observed by Her *et al.* [Her+98]. Ultra-short laser pulses are used to irradiate the surface of a Si wafer. Interference of the incoming and reflected laser light leads to an intensity variation with a periodicity in the order of the laser wavelength. This subsequently leads to the generation of so-called laser induced periodic surface structures (LIPSS). The effect is further amplified through self-focusing of the laser on the modified surface. In the end, the combination of ablation, slight melting and etching due to self-generated intensity spikes finally form cone-like microstructures [Ebe+21]. In case of the in this work discussed targets, the processing steps needed to produce the samples have been discussed in publications by Ebert *et al.* [Ebe+17; Ebe+21] and will be shortly summarised here.

The samples are placed on scanning electron microscope (SEM) pins and subsequently in a processing chamber, that can be evacuated or filled with a processing medium. In this case, sulfur hexafluoride (SF_6) is used as the ambient medium with a pressure of $600\,\mathrm{mbar}$. The actual structuring is done with a pulsed Ti:sapphire laser at a central wavelength of $800\,\mathrm{nm}$ and with a repetition rate of $5\,\mathrm{kHz}$. The laser pulses, which are set to a pulse length of $100\,\mu\mathrm{m}$, pass a focusing lens. The beam is then pointed on the sample surface with two galvanometric mirrors, allowing for precise positioning and movement over a large area. On the surface, the focused beam with a size of $70\,\mu\mathrm{m}$ full width at half maximum (FWHM), is scanned over the sample. The distance between the scanning lines are optimised to achieve a homogeneous structuring, while the scanning speed determines the number of pulses interacting with each individual spot. With this process, an area of $1\mathrm{x}2\,\mathrm{mm}^2$ is treated.

A further characteristic of this process is that the formation of the structures is parallel to the laser and does not depend on the surface orientation [Ebe+21]. This can be used to fabricate slanted microstructures by tilting the sample during the structuring process. After the structuring process is finished, the samples are taken out of the processing chamber, detached from the SEM pin and ready to be mounted for the experiment.

4.3 Overview of finished targets

In the following section, an overview over the fabricated targets will be given. The main focus of this work is the layered target with microstructures on the front surface. Layered targets without a microstructured front surface were prepared and evaluated for comparison. Thirdly, simple pure Cu foil targets are prepared as well to observe and compared the results to a classical backlighter target during the experiment.

Microstructured layered targets

The microstructured layered targets (MLTs) are fabricated as outlined in the previous section (4.2). In figure 4.2 (a), a SEM image of a microstructured front surface is displayed together with a schematic (4.2 (b)), indicating the following dimensions. The structured area, with a size of $1\mathrm{x}2\,\mathrm{mm}^2$, has a remaining base thickness b of $(5 \pm 2)\,\mu\mathrm{m}$. The cone-like microstructures themselves have a height h of $(25 \pm 5)\,\mu\mathrm{m}$ and a base width w of $(6 \pm 2)\,\mu\mathrm{m}$. This leads to a rough distance between the cone tips of $(10 \pm 5)\,\mu\mathrm{m}$. These parameters are very similar to targets previously used in experiments conducted by Ebert *et al.* [Ebe+20].

[Her+98] Her et al. (1998), “Microstructuring of silicon with femtosecond laser pulses”.

The experiments, conducted at the STFC Rutherford Appleton Laboratory and using the VULCAN laser system, showed great promise of the microstructured surfaces for high energy laser experiments. The uncertainties of the here given values are mainly due to the random nature of the fabrication process, which leads to a variance of the cone-like structures.

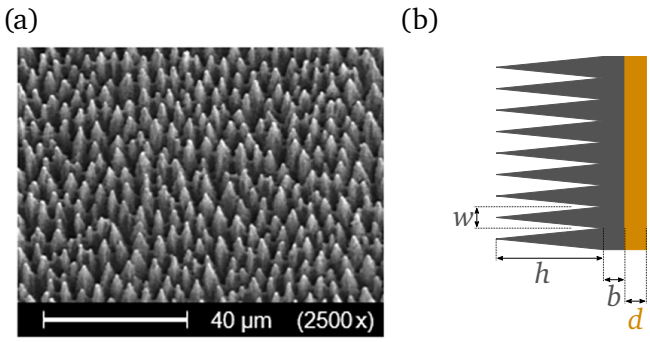

Figure 4.2: SEM image of Si microstructures (a) and relevant sizes of the MLT (b). The microstructures display a high degree of uniformity over the imaged region, with a relatively homogeneous positional distribution. The base width w is used to describe the spacing between the cone-like structures. The SEM image is reproduced from [Ebe+21].

The back side layer is defined by two main parameters, the lateral dimension and the thickness of the deposited Cu. The former is chosen to be $3\text{x}3\,\mathrm{mm}^2$ in order to cover all of the structured area from the back side. While this lateral dimension is relatively minor for the target performance, the thickness can influence the observed $K\alpha$ yield. As discussed previously, electron refluxing is the dominating mechanism of $K\alpha$ emission in a target driven by relativistic intensities. As such, as long as the layer enables sufficient electron collisions with the Cu atoms during each pass, no further change is expected beyond this lower boundary. This has been investigated by Theobald *et al.*, observing a constant yield for Cu target thickness variations between 2 - $20\,\mu\mathrm{m}$ [The+06]. The same behaviour is observed by Park *et al.* for silver targets up to $100\,\mu\mathrm{m}$ as well [Par+06]. For the targets investigated in this work, the thickness is chosen to be $(5 \pm 1)\,\mu\mathrm{m}$, well beyond the minimal thickness of $2\,\mu\mathrm{m}$.

The finished samples are then mounted for further handling during the experiment. The samples are first glued on a machined piece of polyethylene terephthalate (PET), such that the layered area extends roughly $5\,\mathrm{mm}$ beyond the stalk. PET is used here to electrically isolate the target from the chamber, limiting the return current of electrons through the mount. This somewhat decreases the typically observed electro-magnetic pulse created during these types of experiments. The PET stalk is then screwed in a short aluminium (Al) adapter, which in turn is bolted onto a Thorlabs kinematic base (type KB1X1). In figure 4.3 the schematic of a fully mounted target is displayed together with an image of the final target.

Multiple variations of the basic MLT are fabricated as well. In a typical solid target experiment, the high-power laser is aligned onto the target with a small angle to prevent direct back reflection of the light into the laser system. This leads to a tilt of the laser with respect to the target normal oriented microstructures. To investigate the influence of this tilt, targets with differently oriented microstructures were manufactured. For the experiments subject of this work, the laser angle is $15°$ (see experimental setup in section 5.1). As such, the microstructures were tilted by this angle with respect to the surface normal. The resulting targets are then used either in parallel or at an angle of $30°$ to the laser. In the following, the three sets of targets are referenced by their angle with respect to the high-power laser as 0, 15 and $30°$ MLT. A SEM image of such tilted microstructures is displayed in figure 4.4 (a).

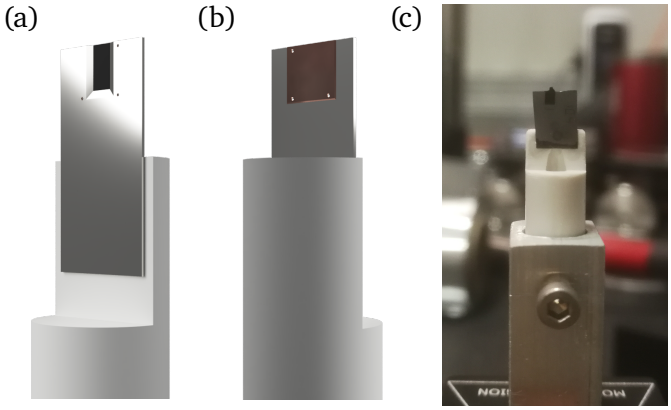

Figure 4.3: Target schematic front (a) and back (b) with image of final target (c). The structured area is clearly visible in the image as a black region. The $3\text{x}3\,\mathrm{mm}^2$ large Cu back side layer is visible in (b). Three small holes in the target were used as markers during the alignment of the target. For characterisation, roughly $1/5$ of the Si sample is broken away from the top, leading to the non-uniform top edge in (c).

The source size of an X-ray target is, together with the overall X-ray yield, an important quantity to gauge the achievable resolution during an experiment. For typical laser-based X-ray targets, this source size is mainly limited by either a very tight laser focus or by manufacturing an enclosure with a pinhole around the backlighter target. The layered target concept provides the unique opportunity to limit the area in which the Cu is deposited and thus restrict the source size. To demonstrate this capability, additional targets are manufactured with only two $(100 \pm 10)\,\mu\mathrm{m}$ diameter dots of Cu. The dots are separated with a distance of $(250 \pm 10)\,\mu\mathrm{m}$ center to center and are displayed in figure 4.4 (b).

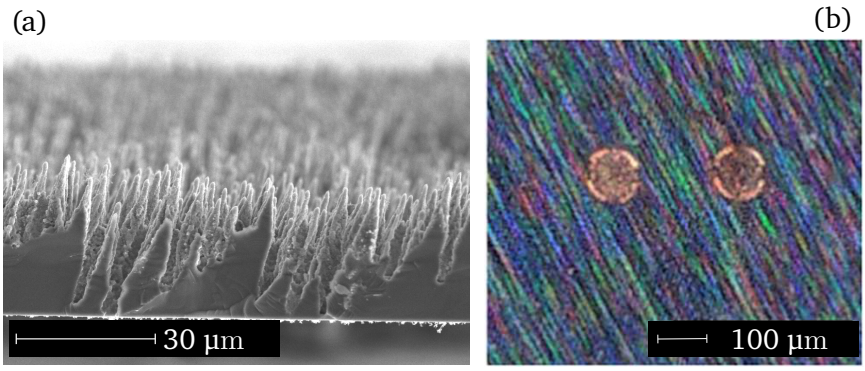

Figure 4.4: SEM image of tilted needles (a) and microscope image of Cu dots (b). The deep troughs between the cone-like microstructures are visible. The microstructures are tilted to the right by $15°$. In (b), the two small Cu dots are visible on the Si backside. The SEM image is courtesy of T. Ebert and (b) is adapted from [Ebe+21].

Reference targets

The flat layered target (FLT) were manufactured in a similar fashion to the MLT. Again, Si samples of $5\text{x}10\,\mathrm{mm}^2$ are laser cut. In order to be able to compare the FLT with the MLT, the thickness of the Si sample

is chosen to be $15\,\mu\mathrm{m}$. This value is derived from the mean density of the microstructured Si, from which the area density of the target is calculated to be $3.5\,\mathrm{mg\,cm^{-2}}$. Matching this value results in comparable energy losses of the electrons due to collisions in the Si layer of both target types. The back side layer is then directly formed through thermal evaporation of Cu up to a thickness of $(5 \pm 1)\,\mu\mathrm{m}$. Similar to the MLTs, two variations of this layer are fabricated. One with the spatial extend of $3\mathrm{x}3\,\mathrm{mm}^2$ and a second variant with two $(100 \pm 10)\,\mu\mathrm{m}$ diameter dots, again spaced $(250 \pm 10)\,\mu\mathrm{m}$ center to center.

For the pure Cu target, samples are simply laser cut from a $10\,\mu\mathrm{m}$ thick foil and directly glued to the PET stalk similar to the MLT. As discussed previously, the thickness of this foil has little influence on the target performance and no change of the CE is expected due to the doubled thickness.

5 Experimental methods

In order to study the microstructured layered targets (MLTs) as described in chapter 4, an experimental campaign at the Petawatt High Energy Laser for Heavy Ion Experiments (PHELIX) was planned, prepared and executed. While MLTs are a novel concept for X-ray backlighters that have not been used before, a previous experiment with only single layer microstructures was performed at the VULCAN laser system [Ebe+20]. This experiment was the cornerstone for the development of MLTs. The focus for the experiment was the close observation of the Cu spectra from the back side of the targets. This chapter gives an overview over how this measurement was achieved. This includes the general setup and secondary diagnostics (section 5.1), the laser system (section 5.2) and the deployed spectrometer (section 5.3).

5.1 Experimental setup

The general setup of the experimental campaign is displayed in figure 5.1. The PHELIX was used to interact with the investigated targets. Using a Cu F/1.7 off-axis parabola (OAP), the laser was focus onto the target under a $15°$ angle. The laser had a pulse length of $500\,\mathrm{fs}$, which together with a mean energy of $145\,\mathrm{J}$ resulted in a power of $290\,\mathrm{TW}$.

Various diagnostics were used to measure both the photon emission during the interaction as well as the ions accelerated from the backside in target normal direction. Four different spectrometers were used to record the copper (Cu) emission. All spectrometer were pointed on the back side of the target, aligned such that the laser target interaction region was in focus. The detected spectral ranges were between 8 - $9\,\mathrm{keV}$, always including the main $K\alpha$ transition at $8048\,\mathrm{eV}$. Two of these spectrometers used a highly oriented pyrolytic graphite (HOPG) as the diffractive medium (see section 5.3.1), while the other two spectrometers used germanium (Ge) crystals with a toroidal surface (see section 5.3.2). The spectrometers were placed under various angles to accommodate for space constraints inside the target chamber between the other diagnostics. The X-ray radiation was observed with image plates (IPs), mounted in an aluminium (Al) housing and shielded by a layer of Al foil from the laser interaction and ambient light inside the chamber. Thin sheets of lead (Pb) were used to block the direct line of sight between target and IP to prevent direct exposure of the IP with X-rays.

In addition to the above mentioned spectrometers that observe the X-ray emission from Cu, which are the main diagnostics, various additional diagnostics were used during the experimental campaign to study the investigated targets. These diagnostics were: a spectrometer with a conical potassium acid phthalate (KAP) crystal that was pointed to the front side to record the X-ray emission at 1.6 - $2.1\,\mathrm{keV}$ as well as a Thomson parabola and radiochromatic films (RCFs) to record the ions and electrons, accelerated target normal from the backside. As these diagnostics were used to study different properties of the targets, the results of these diagnostics will not be discussed further in this thesis.

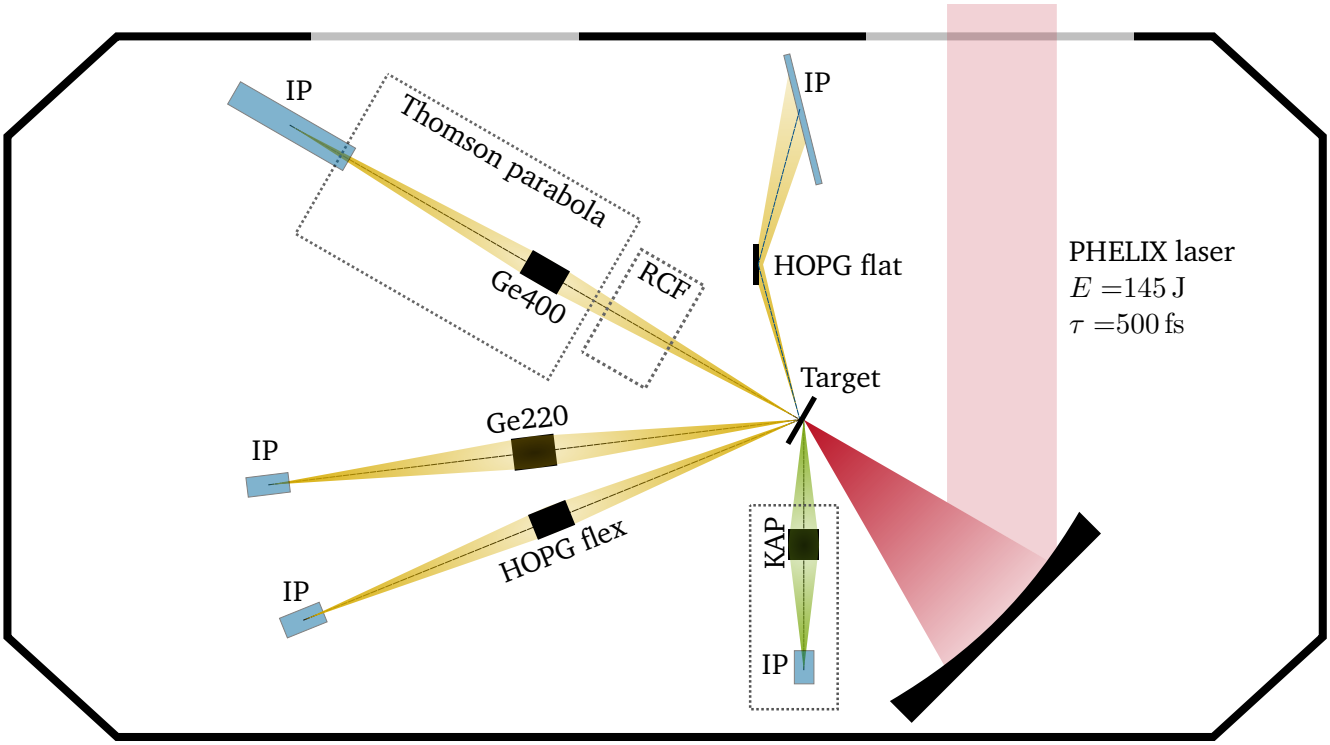

Figure 5.1: Overview over the experimental setup. The PHELIX laser enters the target chamber on the top right flange. The laser is reflected from a Cu $45°$ OAP onto the target under $15°$. Four spectrometer measure the emission spectrum on the back side of the target. The two additional diagnostics (Thomson parabola and RCF stack) are used to diagnose the spectrum of accelerated ions, an analysis not done in this thesis.

The setup included focal diagnostic, imaging the focal plane with a microscope objective (50X Mitutoyo Plan Apochromat) onto a charge-coupled device (CCD) camera outside of the target chamber. This diagnostic was used to align the target before each measurement. The principle procedure included the following steps. First, the target was positioned with the help of alignment markers. With the help of these markers, a central position within the structured area was located for the interaction with the laser. Due to the light-absorbing nature of the microstructures, the imaging system was not able to allow for a direct positioning of the laser with respect to single structures. As such, the interaction is statistically distributed with respect to the position along a single structure between measurements. As a second step the target was aligned with respect to the focal plane, which was achieved through optimizing the edges of the alignment markers and assuming a flat target. Once the target position was found, the target was moved out of the beam path and the laser was imaged into the focal diagnostic with the same focal plane.
An exemplary focus is shown in figure 5.2. The best achievable focus for the experiment was measured to be $(6.4 \pm 1.2)\,\mu\mathrm{m}$, indicated by the red circle in figure 5.2. In addition to the focus, coma-like aberrations are observed for all pre-measurement focal images. These aberrations distribute the delivered energy into a much larger area. A similar behaviour of this specific OAP is documented by Hornung *et al.* as well [Hor+20]. This spread in the focal plane lead to a decrease of energy inside the focus to about 30 - $40\,\%$, with the remaining energy located in a roughly $12 \times 12\,\mu\mathrm{m}^2$ area. This lead to an effective peak intensity of the focal spot of $1 \times 10^{20}\,\mathrm{W\,cm^{-2}}$, with the remaining energy being distributed around the

[Hor+20] Hornung et al. (2020), "Enhancement of the laser-driven proton source at PHELIX".

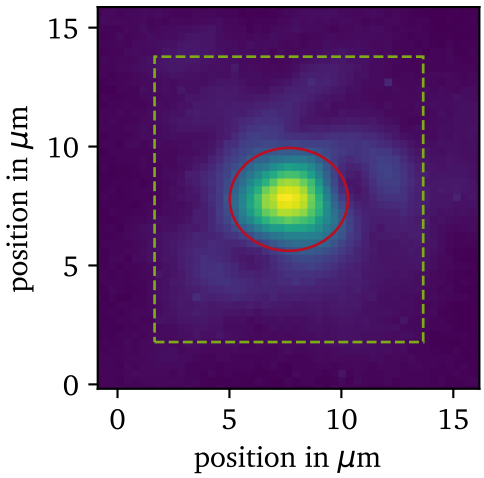

Figure 5.2: Recorded image of the laser focus. The focus image displays some coma-like aberrations around the focus in a $12 \times 12\,\mu\mathrm{m}^2$ area (green box). The focus itself is indicated with the FWHM by a red circle.

focus still reaching intensities of $1 \times 10^{19}\,\mathrm{W\,cm^{-2}}$.

Besides the previously mentioned laser parameters, the laser contrast is also vital to the targets performance. In particular, the level of amplified spontaneous emission (ASE) before the main pulse can determine the nature of the laser target interaction. If the contrast between ASE and laser peak is low, the ASE can already begin to ionise the target multiple ns before the main pulse arrives. This can harm the interaction in multiple ways. On the one hand, the ionised material can fill the valleys of the microstructures, themselves only multiple $\mu\mathrm{m}$ large and destroy any geometrical advantage. On the other hand, some electron heating mechanisms rely on a sharp surface gradient which is lost with the ablation of ionised material. Thus it is important to have a high ASE contrast. During the experiment, the influence of this ASE contrast was studied by varying it, a unique possibility at the PHELIX laser. How this was achieved is discussed in the following section.

5.2 The PHELIX laser system

The PHELIX laser system is a short pulse, high energy laser system, which amplifies its pulses through multiple stages of chirped pulse amplification (CPA). The PHELIX laser system has two front ends, which generate a long (0.7 - $20\,\mathrm{ns}$) or short (0.5 - $10\,\mathrm{ps}$) pulse, respectively [Bag+10]. Either pulse is then amplified by multiple Nd:glass amplifiers before being delivered to one of three target areas: the laser lab, the target chamber in the PHELIX laser hall, which was used for the experiment in this work, and the Z6 experimental area for investigations in tandem with the Nanosecond High Energy Laser for Heavy Ion Experiments (nhelix) laser and the ion beam provided by the Unilac.

In the scope of this work, only the short pulse option of the PHELIX laser was used. The laser pulse is generated in a commercial Ti:Sa-oscillator (Mira 900, Coherent) with a central wavelength of $1053\,\mathrm{nm}$, a pulse energy of $2\,\mathrm{nJ}$ and a pulse duration of $100\,\mathrm{fs}$ full width at half maximum (FWHM). This laser pulse is

[Bag+10] Bagnoud et al. (2010), “Commissioning and early experiments of the PHELIX facility”.

then passed into an ultrafast optical parametric amplifier (uOPA). In this module, the laser pulse is split, with one part remaining the signal pulse and the other part being the pump pulse. The signal pulse is simply delayed and then guided into a barium borate (BBO) crystal, where it is overlapped with the pump pulse. The pump pulse is stretched to $480\,\mathrm{ps}$ and then amplified by a doped fiber and afterwards by a regenerative amplifier. It is then compressed to approx. $1\,\mathrm{ps}$ (FWHM) and frequency doubled to $520\,\mathrm{nm}$, before being overlapped with the signal pulse. During the overlap, the signal pulse is amplified to an energy of $200\,\mu\mathrm{J}$ without the generation of ASE. The signal pulse itself is then stretched to $2.3\,\mathrm{ns}$ (FWHM) and further amplified by two regenerative amplifiers. Through the initial amplification with the uOPA, the two following regenerative amplifiers can be operated with a lower amplification factor and subsequently, a lower ASE level is achieved. Following the initial front-end amplification, the signal pulse is further amplified by the pre-amplifier with three flash lamp pumped Nd:glass rods up to a pulse energy of $5\,\mathrm{J}$. The last amplification stage is then realised with ten Nd:glass slaps, grouped into five amplifiers. This module is operated in a double pass, increasing the laser energy to $180\,\mathrm{J}$ used in the experiment. Finally, the pulse is compressed with two $80 \times 40\,\mathrm{cm}^2$ dielectric gratings to the final pulse length of $500\,\mathrm{fs}$ and transported to the target chamber with two deflection mirrors, before the final focusing is achieved with a Cu F/1.7 OAP. The transmission of these last optics is estimated to $80\,\%$, resulting in a laser energy of $145\,\mathrm{J}$ on the target.

Through a change in the amplification factor between the uOPA and the following two regenerative amplifiers, the PHELIX laser system can continuously change the ASE level from 3.5×10^7 without the uOPA to 1.1×10^{12} for the best achievable contrast. For the experiments presented here, in addition to both previously stated contrast settings, a third medium contrast was adjusted to be at 1.8×10^{10}. The corresponding measurements up to $2\,\mathrm{ns}$ before the main pulse are shown in figure 5.3.

5.3 X-ray spectrometers

In this section, an overview over the four different crystal spectrometers measuring the Cu X-ray yield is given. The overall Cu spectrum for *K*-shell emission ranges from 8027 - $8905\,\mathrm{eV}$ for $K\alpha_2$ to $K\beta$, respectively. Two spectrometers are used to cover this spectral range, a flat crystal HOPG spectrometer and a curved crystal HOPG spectrometer (referred to as HOPG flat and HOPG flex respectively). The latter had a slightly reduced spectral range, covering only up to $8800\,\mathrm{eV}$, but was set up with a much narrower instrumental energy spread. These two spectrometer are described in section 5.3.1.
To measure the spatial extend of the sources as well as the spectral output, two spectrometers with toroidal crystals were set up. The principle of these crystals is described in chapter 3.3.2. In addition to the imaging capabilities, the spectral resolution is also increased for these spectrometers. The key characteristics and differences between these two spectrometers are described in section 5.3.2. For a quick reference, Tab. 5.1 lists some relevant characteristics of the four mentioned spectrometers.

Table 5.1: Overview of spectral characteristics of the used spectrometer setups.

spectrometer	layout	spectral range in eV	PSF width in eV	efficiency in sr
HOPG flat	flat crystal	8000 - 8905	30.0	5.78×10^{-4}
HOPG flex	von Hamos	8000 - 8800	8.8	1.99×10^{-4}
Ge220	imaging	8000 - 8200	3.4	2.65×10^{-5}
Ge400	imaging	8000 - 8100	2.3	3.31×10^{-6}

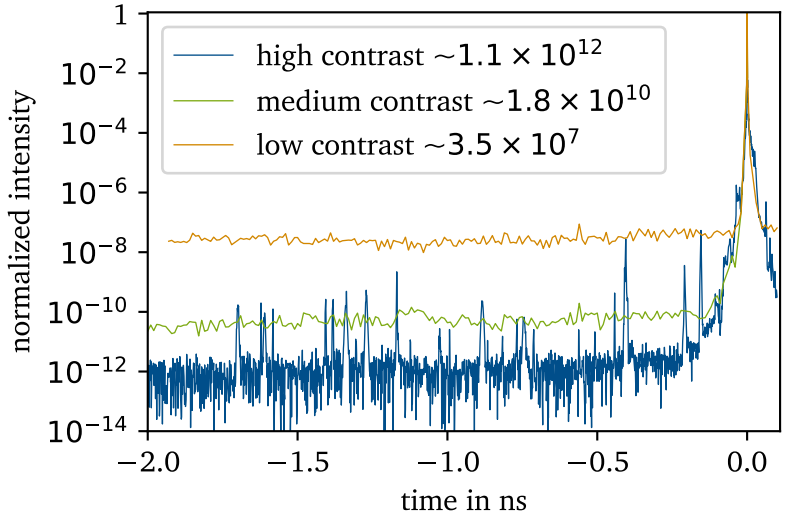

Figure 5.3: ASE contrast of the PHELIX laser for three different settings of the uOPA. The measurement of the high contrast is made before the experiment and with a higher resolution than the medium and low contrast measurements. Due to the lower resolution, potential pre-pulses are not observed. A constant ASE level up to $2\,\mathrm{ns}$ before the main peak is observed for all three uOPA settings. The measurements were made by C. Brabetz.

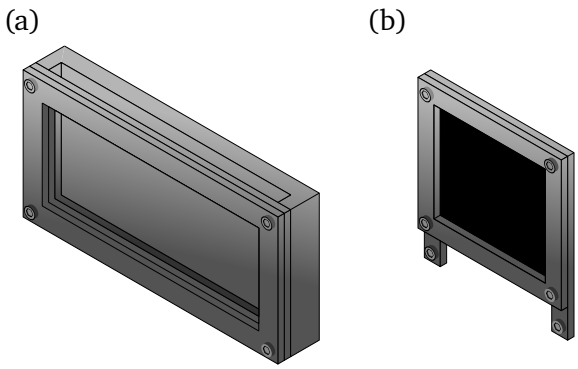

Figure 5.4: Schematic of the IP housing (a) and debris shield (b). The IP housing has a slit at the top for easy access during the change-over. Black Pokalon is used as a debris shield in front of the crystals.

All spectrometers used IPs manufactured by Fuji to record the X-ray radiation. Fuji BAS-SR type IPs were used for the flat HOPG spectrometer, while Fuji BAS-TR IPs were used for the other three Cu spectrometers. The utilised calibrations to convert the recorded signal to incident photon numbers are described in section 3.3.3. All IPs were mounted in an Al housing, a schematic of which is displayed in figure 5.4 (a). The housing consisted of a base plate with a cut out for the IP and two Al frames to be mounted in front of the IP. Fully assembled, the housing allowed for easy access of the IP through the top slit, which was closed with Al tape during the measurement itself. Al foil was positioned between the two frames, fully shielding the IP from ambient light exposure.

A similar holder, consisting of two Al frames was positioned in front of the crystals (see figure 5.4 (b). A sheet of $12\,\mu\mathrm{m}$ thick Pokalon[1] was mounted in the holders to protected the crystals from the disintegrating target. If the observed signal on the IP was too strong, saturating the scanner, additional layers of $10\,\mu\mathrm{m}$ thick Cu foil were used in conjunction with the Pokalon to decrease the signal.

5.3.1 HOPG spectrometers

To capture the spectral range of $\Delta E \approx 1\,\mathrm{keV}$, a large surface area is needed to allow for the required change in incidence angle while retaining a good spectral resolution. Two HOPG crystals are used to achieve this, a thick, flat HOPG crystal with a surface area of $50\,\mathrm{mm} \times 20\,\mathrm{mm}$ and a thin, flexible HOPG crystal[2] with an area of $40\,\mathrm{mm} \times 20\,\mathrm{mm}$. The latter is fixed on a Al base, which gives the crystal a radius of curvature of $115\,\mathrm{mm}$. The two spectrometers are setup following the von Hamos geometry (see section 3.3.2), albeit the flat crystal does not benefit from the focusing advantages of this geometry. Nonetheless, the distance from target to crystal d_{sc} is kept the same to the distance from crystal to detector d_{cd} for optimal mosaic focusing. Both crystals are placed on the horizontal plane of the target, observing the emitted radiation from the backside. As shown in figure 5.1, the angle to the target normal is relatively large for both spectrometer with $(41.0 \pm 0.1)^\circ$ and $(52.1 \pm 0.1)^\circ$ for the flat and curved HOPG crystals, respectively.

Despite the similar approach, the two spectrometer lead to very different dispersion behaviours. For the flat HOPG crystal, the nominal resolution on the IP is $0.84\,\mathrm{eV/px}$. However, due to a high thickness of $> 2\,\mathrm{mm}$, which leads to a high acceptance angle, the point spread function (PSF) is very broad with a FWHM of $30.0\,\mathrm{eV}$. The curved HOPG on the other hand is thinner, decreasing the mosaic focusing error, leading to a narrower PSF of $8.8\,\mathrm{eV}$ width (FWHM). As this crystal is $10\,\mathrm{mm}$ shorter in the dispersive direction, this higher resolving power is offset by a shorter overall spectral range. Both spectrometers measured the spectral range from the $K\alpha$ doublet up to the Lyα peak, with the flat HOPG spectrometer even recording the $K\beta$ at $8905\,\mathrm{eV}$. The development, set up and initial analysis of the latter spectrometer was done during a master thesis by D. Hartnagel [Har19], and the reader is referred to this work for further information.

The spectrometer performance was analysed with the help of the ray tracing code mmpxrt[3] developed by Šmíd *et al.* [ŠPF21]. The code was developed with the unique characteristics of mosaic crystals such as HOPG in mind. It can deliver useful insights such as the specific PSF for the setup, as well as a rough dispersion relation. In figure 5.5 (a) and (b), the estimated PSFs calculated with mmpxrt are shown. The above discussed effect of crystal thickness can be seen in both the shape and overall width of the PSF. In

[Har19] Hartnagel (2019), "Entwicklung eines Röntgenspektrometers für Laser-Plasma-Experimente".
[ŠPF21] Šmíd et al. (2021), "X-ray spectrometer simulation code with a detailed support of mosaic crystals".

[1] Pokalon is the proprietary name of a polycarbonate thermoplastic polymer foil.
[2] The HOPG flex crystal was provided by the group of K. Falk at the Technical University Dresden.
[3] The code can be found at `https://gitlab.hzdr.de/smid55/mmpxrt`

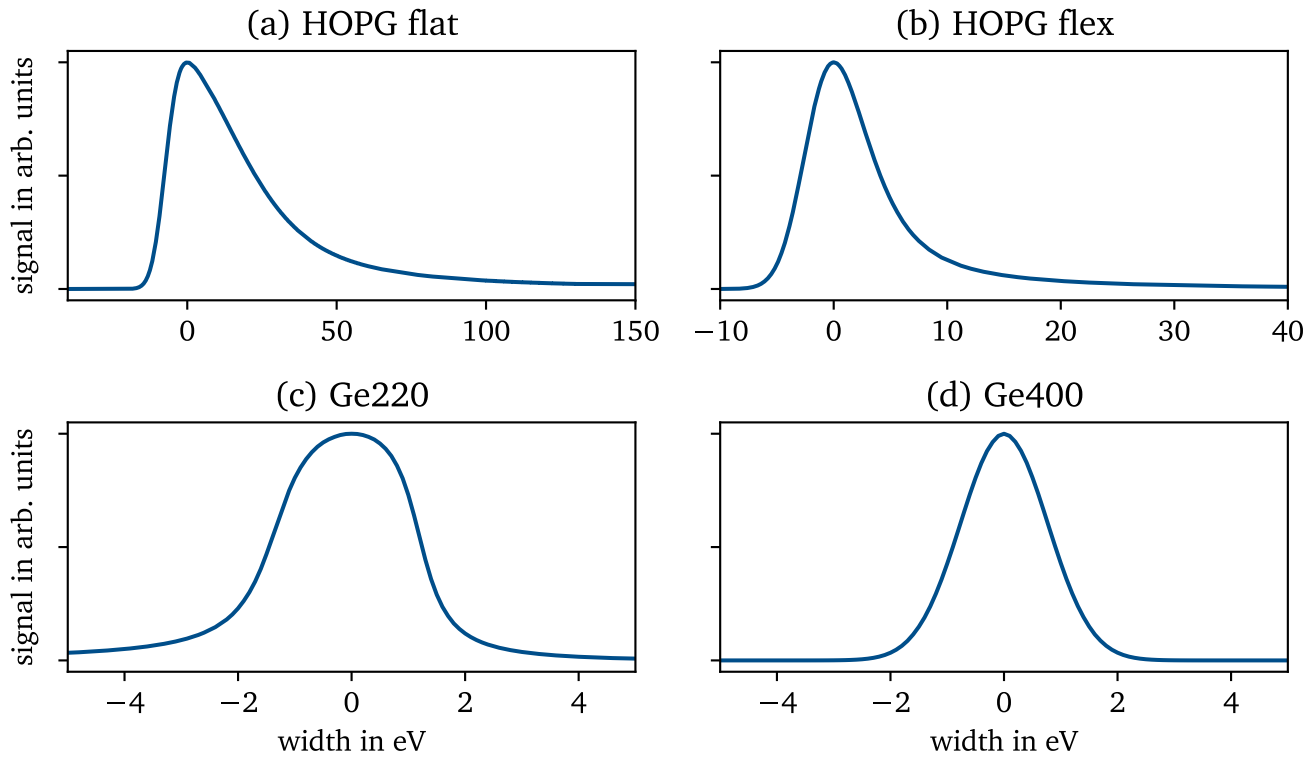

Figure 5.5: Estimated PSF for the employed spectrometers. For both HOPG spectrometers, the PSF displays an asymmetric behaviour. This asymmetry is due to varying levels of penetration into the crystal, leading to mosaic focusing errors. This is larger for the thicker, flat HOPG. In comparison, the two Ge spectrometers display much more symmetric PSFs, with the one for the Ge400 spectrometer being close to Gaussian. The width is also much smaller for these two spectrometers.

addition, this tool is used to estimate the spectrometer efficiency without the need to further measure the rocking curve and integrated reflectivity. This value is influenced by both the crystal characteristics as well as the distances d_{sc} and d_{cd}. For the here discussed spectrometers, the efficiencies are estimated to be $5.78 \times 10^{-4}\,\text{sr}$ (HOPG flat) and $1.99 \times 10^{-4}\,\text{sr}$ (HOPG flex).

5.3.2 Ge spectrometers

In order to infer spatial information about the source as well as spectral data, toroidally shaped crystals were used. The spectrometers follow the design principle of a 2D bent crystal described in section 3.3.2, referred to as imaging spectrometer. The key difference between the two Ge crystals is the plane along it is cut. This is also used to identify the two spectrometers in the following. Furthermore both crystals are produced with varying radii in spatial (R_v) and dispersive (R_h) direction. The values are given in Tab. 5.2.

The experimental setup chosen for both spectrometers has a big impact on the detection resolution of the $K\alpha$ doublet. The crystals are placed again facing the back side of the targets, with the Ge220[4] in the

[4]The Ge220 crystal was provided by the group of K. Falk at the Technical University Dresden.

Table 5.2: Geometric parameters of the used Ge crystals.

reflection plane	size in mm^2	R_v in mm	R_h in mm
(220)	25×50	150	1500
(400)	15×50	200	400

horizontal plane and offset from the target backside normal by $(42.3 \pm 0.1)°$. The Ge400[5] crystal is placed nearly target normal ($(2.1 \pm 0.1)°$ in the horizontal plane), but vertically offset by an angle of $(64.3 \pm 0.1)°$. This had to be done due to spatial constrains imposed by the target normal ion diagnostics (see figure 5.1). The IPs are placed further away from the crystals ($d_{\mathrm{cd}} > d_{\mathrm{sc}}$) to achieve a magnification > 1, in contrast to the mosaic crystals. This magnification is 1.89 for the Ge220 and 1.72 for the Ge400 spectrometer. The resulting spectral ranges are such, that only the $K\alpha$ doublet is visible. The advantage is a higher resolution of this doublet, as can be seen by the very narrow PSFs in figure 5.5 (c) and (d). As Ge is a monocrystalline, the observed PSF is also much more symmetric than for the HOPG crystals.

The efficiencies of the two spectrometer are again estimated with the code mmpxrt. However, values for R_{int} and the FWHM of the rocking curve had to be estimated beforehand. This was done with the code DIXI [HWF98]. The calculations with this code were made by M. Šmíd. The resulting efficiencies are much smaller than for the mosaic crystal spectrometers at $2.65 \times 10^{-5}\,\mathrm{sr}$ and $3.31 \times 10^{-6}\,\mathrm{sr}$ for the crystals Ge220 and Ge400 respectively. While lower efficiencies are expected for monocrystals, a decrease by over one magnitude seems implausible. One possibility for this could be an under-estimation of the crystal reflectivity. Rocking curve measurements of the crystals were however not possible during this thesis to further determine the reflectivity of these crystals and thus giving the possibility of more precise efficiency calculation.

5.3.3 Image plate calibration

For the analysis of a recorded spectrum on the IP, and in particular the calculation of recorded photon numbers, a conversion from deposited energy to photo-stimulated luminescence (PSL) is needed. Furthermore, the metastable states stored in the IP decay over time. As such, a fading correction needs to be applied. Both calibrations have been studied by multiple groups and the calibrations selected for this thesis are described in the following.

Image plate fading

After a measurement, the target chamber has to be vented and checked for radioactive radiation before the IPs can be accessed and transported to the scanner for read out. Overall, this processes took between 20 - $30\,\mathrm{min}$. For the transport, the IPs were kept in light-tight sleeves to minimise the de-excitation of the metastable states. However, even ambient thermal excitation can lead to a decay of signal. Many studies have been done to investigate the fading behaviour of Fuji BAS IPs [OYN00; OY02; MBS08; Mad+11;

[OYN00] Ohuchi et al. (2000), "Functional equation for the fading correction of imaging plates".
[OY02] Ohuchi and Yamadera (2002), "Dependence of fading patterns of photo-stimulated luminescence from imaging plates on radiation, energy, and image reader".

[5] The Ge440 crystal was a loan from D. Montgomery from the Los Alamos National Laboratory.

Bon+13b; Bon+13a; Bou+15]. It has been found that the rate at which the signal fades depends on multiple factors. These include the IP type, the radiation type and its energy, the temperature of the IP and the scanner used for the read-out [OY02].

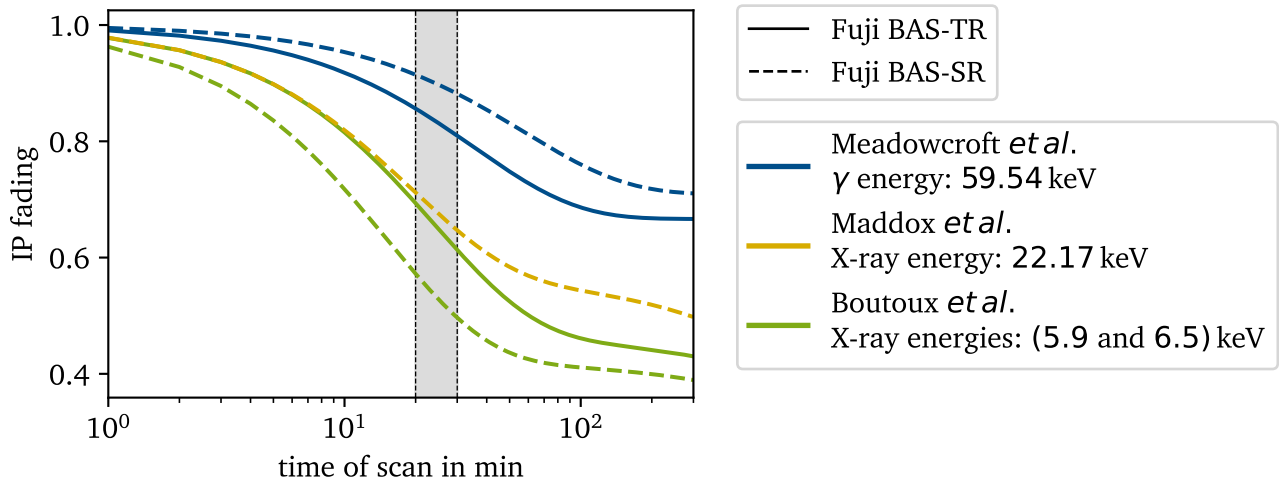

Figure 5.6: Fading characteristic of an IP. The fading curves, reproduced from [MBS08; Mad+11; Bou+15], show a strong variation depending on the incident photon energy. The in green shown fading corrections are chosen for this analysis, as the incident photon energies are the closest to the observed spectral range. The rough time window of the scan times is marked in gray.

Of the mentioned studies, three used X-ray emission to irradiate the IP and subsequently scanned the IP with the same scanner as used for this experiment, a Fuji Typhoon FLA-7000 [MBS08; Mad+11; Bou+15]. The fading behaviour found in these references is displayed in figure 5.6 for both the Fuji BAS-TR and BAS-SR type IPs. A strong variation between the three studies can be observed, leading to a difference in faded signal between $5\,\%$ to $50\,\%$ in the case of Fuji BAS-SR IPs for a fade time of $25\,\mathrm{min}$. The remaining free parameter between the three studies is the photon energy used to irradiate the IPs. Meadowcroft *et al.* used a ^{241}Am source, emitting $59.54\,\mathrm{keV}$ gammas, while Maddox *et al.* used a ^{109}Cd source, which emits $22.17\,\mathrm{keV}$ X-rays and Boutoux *et al.* used a ^{55}Fe source, with X-ray emission of 5.9 and $6.5\,\mathrm{keV}$. With the observation of X-rays in the energy range of 8 - $9\,\mathrm{keV}$ during the experiments, the fading correction of Boutoux *et al.* was chosen for this thesis for both the Fuji BAS-TR and BAS-SR types. The following double-exponential model was found by the authors:

$$f\left(t\right) = A_1 * \exp\left(\frac{-t}{B_1}\right) + A_2 * \exp\left(\frac{-t}{B_2}\right). \tag{5.1}$$

The corresponding values for $A_{1,2}$ and $B_{1,2}$ are recorded in table 5.3. It is assumed, that the fast and slow component within this double-exponential behaviour are due to differently trapped electrons. If the electrons are trapped closer to the conduction band, the decay is more probable, leading to a faster decay [OYN00].

[Bon+13b] Bonnet et al. (2013), "Response functions of imaging plates to photons, electrons and 4 He particles".
[Bon+13a] Bonnet et al. (2013), "Response functions of Fuji imaging plates to monoenergetic protons in the energy range 0.6–3.2 MeV".
[Bou+15] Boutoux et al. (2015), "Study of imaging plate detector sensitivity to 5-18 MeV electrons".

Table 5.3: Values of the used fading function. Analytic model was found by Boutoux *et al.* [Bou+15]

	A_1	B_1 in min	A_2	B_2 in min
Fuji BAS-TR	0.535 ± 0.016	23.8 ± 2.2	0.465 ± 0.012	3800 ± 500
Fuji BAS-SR	0.579 ± 0.021	15.1 ± 1.6	0.421 ± 0.013	3800 ± 650

Response function

The measured signal is given in PSL after application of the scanner specific calibration (see section 3.3.3). In order to calculate photon numbers from PSL, a calibration of the IP is needed. This calibration Ψ is again a function of IP type, the radiation incident on the IP, radiation energy and the scanner. Many of the above mentioned studies that investigate the fading behaviour also provide a calibration for various radiation types and energies for Fuji biological analysis system (BAS) IPs [MBS08; Mad+11; Bon+13b; Bon+13a; Bou+15]. Of these studies, Meadowcroft *et al.*, Maddox *et al.* and Bonnet *et al.* investigated the response of IPs to X-ray irradiation [MBS08; Mad+11; Bon+13b]. All three found a piecewise linear response, which is split at the most prevalent absorption edges of the phosphor material, namely the Ba L-edges between 5.2 - $6\,\mathrm{keV}$ and the Br K-edge at $13.474\,\mathrm{keV}$. The calibration is then described by

$$\Psi\left(E\right) = \eta * \left(m_j * E + c_j\right), \tag{5.2}$$

where E is the incident X-ray energy in keV and m_j and c_j the linear coefficients for the IP response per absorbed X-ray photon in the energy range j. The prefactor η describes the absorption behaviour. The three studies used different methods to determine the absorption inside of the IP. Meadowcroft *et al.* only used calculated absorption efficiencies for their model, without further specifying the calculation details. Bonnet *et al.* used a Monte Carlo code to model the interaction and estimate the absorption, while Maddox *et al.* measured the absorption and found good agreement to calculated absorption efficiencies, again without further specification of the calculation itself. Neither authors provide a analytical representation of the found absorption behaviour. Thus, for this work, the absorption was determined from known transmission data of Mylar and $\mathrm{BaFBr_{0.85}I_{0.15}}$, found by Henke *et al.* [HGD93]. Figure 5.7 displays the calibration found by Meadowcroft *et al.* and the transmission through the protective layer and the phosphor. For energies between 6 - $13.5\,\mathrm{keV}$, the Fuji BAS SR IP has a higher response than the BAS TR IP. Between 3 - $3.5\,\mathrm{mPSL}$ per incident photon of 8 - $9\,\mathrm{keV}$ is expected, depending on the IP type.

Overall, Meadowcroft *et al.* and Bonnet *et al.* are in good agreement within the uncertainties of their measurements, while the calibration found by Maddox *et al.* shows lower responses for energies below $20\,\mathrm{keV}$ [Bon+13b]. The calibration of Meadowcroft *et al.* was chosen for the further analysis for two main reasons. First, the response stated by Meadowcroft *et al.* is higher, ensuring that the calculated photon numbers are a lower bound. Secondly, Maddox *et al.* do not provide a calibration for one of the used IP types (Fuji BAS TR). Furthermore, as these calibrations, together with the fading correction, depend on many factors that could not be ensured during the experiment, such as a stable temperature during the delay between measurement and scan time, the uncertainty is assumed to be $50\,\%$ for all values obtained with these calibrations.

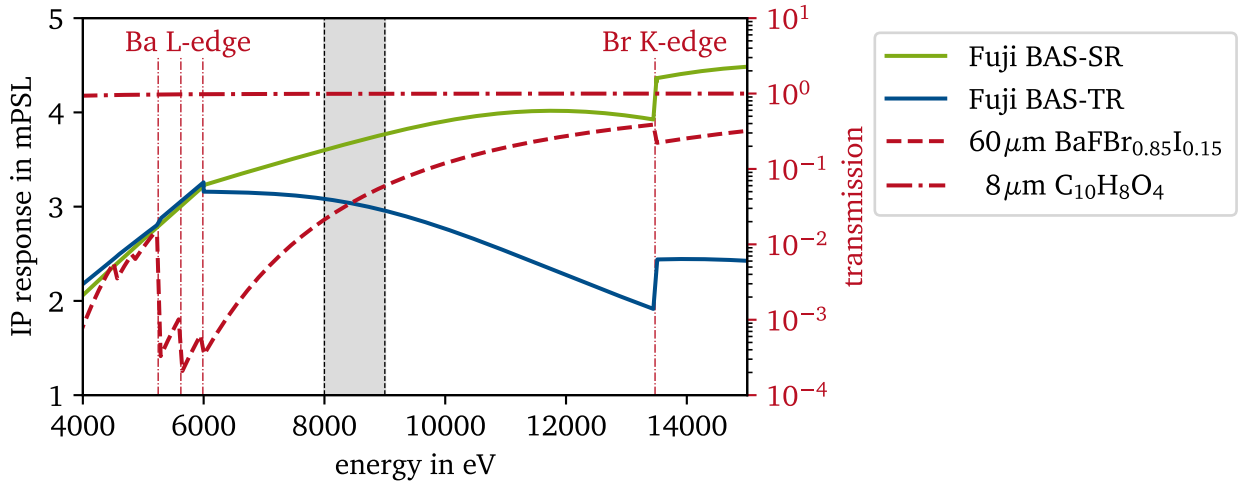

Figure 5.7: Response functions of the employed IPs. The response functions are influenced by the transmission through the phosphor layer (red dashed), while the mylar top layer does little to influence the BAS-SR response function. The spectral range relevant for this work is shaded in gray. The transmission data is obtained from Henke *et al.* [HGD93] and the response functions are reproduced after Meadowcroft *et al.* [MBS08].

6 Experimental results

In the following sections, the results from the experimental campaign at the PHELIX laser system are presented. These results include the general spectral emissivity of the layered targets 6.1, the quantitative analysis of the observed emission behaviour 6.2 and the comparison with atomic-radiative simulations to conclude bulk electron temperatures in the copper (Cu) layer of the target 6.3.

6.1 Spectral emissivity of layered targets

The spectral emissivity of the studied target can give great insights into the state of the emitting material, as has been discussed in chapter 3. In this section, this spectral emissivity is analysed. First, the procedure of spectrum calibration is explained (6.1.1). Then the three major target types are discussed individually, namely the reference pure Cu foil, the flat layered target (FLT) and the microstructured layered target (MLT).

6.1.1 Calibration of the spectrometers

The raw scan has to be processed before the final spectrum can be acquired. Starting with the initial scan, the image is converted from grayscale to photo-stimulated luminescence (PSL) according to equation (3.34). The result of this step is displayed in figure 6.1 (a). A lineout of the spectrum is taken within the horizontal lines. Between the clearly visible line emission, a varying background is observed as well. Its shape is approximated with an asymmetric least squares smoothing algorithm [BEH05; Bae+15] and then simply subtracted. It should be mentioned that for the flat HOPG spectrometer, a prominent flat field is observed as well. This further modifies the bremsstrahlung background and is subtracted in the same manner.

The next step is to find the dispersion relation. This is done through peak identification of measurements with two or more identifiable peaks. Only peaks with well known energy are used here, typically $K\alpha$, Heα and Lyα. A polynomial of either first or second order, depending on the number of identifiable peaks, is fit through these points. The found dispersion relation is then compared to the estimate derived from the ray-tracing simulation of the spectrometer (see sections 5.3.1 and 5.3.2). For all spectrometer, a reasonable agreement of the calculated dispersion relation to the experimental one could be found. The thus found dispersion relations are then applied to the remaining measurements, where the prominent $K\alpha$ peak is used as a fixpoint.

[BEH05] Boelens et al. (2005), "Sign Constraints Improve the Detection of Differences between Complex Spectral Data Sets: LC-IR As an Example".
[Bae+15] Baek et al. (2015), "Baseline correction using asymmetrically reweighted penalized least squares smoothing".

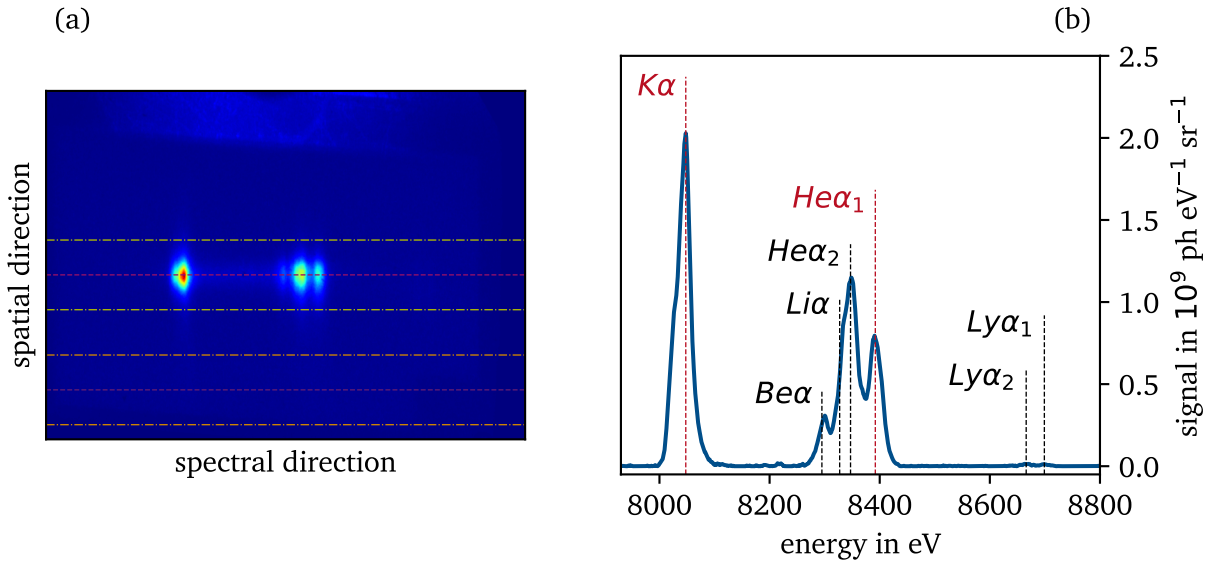

Figure 6.1: Spectrum calibration process. The scanned image of an IP is shown in (a). Vertical summation between the dash-dotted lines lead to the signal (upper area) and background (lower area) of the measurement. The lineout is calibrated through peak identification, for which the red marked lines are used, and with equation (6.1). The resulting spectrum is shown in (b).

To evaluate the spectra quantitatively, a conversion from PSL to photon numbers must be made. This is done through multiple corrections previously described in the sections 3.1.3 and 5.3.3. A fading of the PSL signal $f(t, E)$ due to a delay between measurement and scan of approximately $(25 \pm 5)\,\mathrm{min}$ is corrected according to equation (5.1). The image plate (IP) response $\Psi(E)$ is corrected as well with equation (5.2), which corresponds to approximately 3 - $4\,\mathrm{mPSL}$ per photon. Both corrections are functions of the IP type and photon energy and are applied accordingly. During the experiment, aluminium (Al), Cu and pokalon filters were used. This is done to, on the one hand, shield the IP from scattered light inside of the target chamber and secondary, reduce the signal on the IP such that the IP scanner does not saturate. The transmission τ through these filters are obtained from Henke *et al.* [HGD93]. Finally, the spectrometer covers only a small angle and its crystal has a limited reflectivity. These values are combined in the spectrometer efficiency $\eta(E)$ and the spectrum is corrected for them as well. All of these corrections can be summarised with

$$S_{\mathrm{ph}}(E) = \frac{S_{\mathrm{PSL}}(E)}{f(t, E) * \Psi(E) * \tau(E) * \eta}. \tag{6.1}$$

Application of equation (6.1) on a calibrated signal results in the final spectrum, as is shown in figure 6.1 (b). It is customary to assume a large uncertainty of $40\,\%$ for the obtained number of photons due to the many assumptions regarding crystal performance and IP calibration. This large uncertainty however does not reflect the shot to shot uncertainty for a single experiment, which is expected to be much smaller at about $5\,\%$.

6.1.2 Results from pure Cu foil target

In figure 6.2, the spectrum observed from the $10\,\mu\mathrm{m}$ thick Cu foil target is displayed. The main resonance lines of Cu are present in this spectrum. The strongest peak is the $K\alpha$ peak at $8047.78\,\mathrm{eV}$, which together

with the $K\beta$ peak at $8905\,\mathrm{eV}$, is emitted from weakly ionised material. As the $K\alpha$ line is used as a fix point during the calibration of the spectrum, no shift can be measured. Inspection of the much higher resolved $K\alpha$ emission recorded with the Ge400 spectrometer (see figure 6.2 (b)) also only displays a small high-energy wing around $8065\,\mathrm{eV}$. While this emission is indicative of weakly ionised Cu, the weak development and strength justifies the assumption of negligible energy shift from the $K\alpha$ lines due to L-shell ionisation. The $K\beta$ line on the other hand displays a clear shift of the line center towards higher energies. This also suggests ionisation of the target. The $K\beta$ is here much more sensitive to the more easily ionised M-shell electrons. Further discussion of the quantitative implications on ionisation state and bulk temperature can be found in section 6.3. The strength of the $K\beta$ emission is also relatively weak at only $11\,\%$ peak height and $15\,\%$ of the FWHM integrated area in comparison with the $K\alpha$ line emission. This is below tabulated relative intensities, which predict a $K\beta$ to $K\alpha$ ratio of 0.17 [Tho+09]. The smaller ratio is explained with an increases of the optical thickness for the central emission line, leading to a reduces peak height and larger peak width. Again, ionisation of the atoms rises the absorption probability, leading to the observed change of the optical thickness.

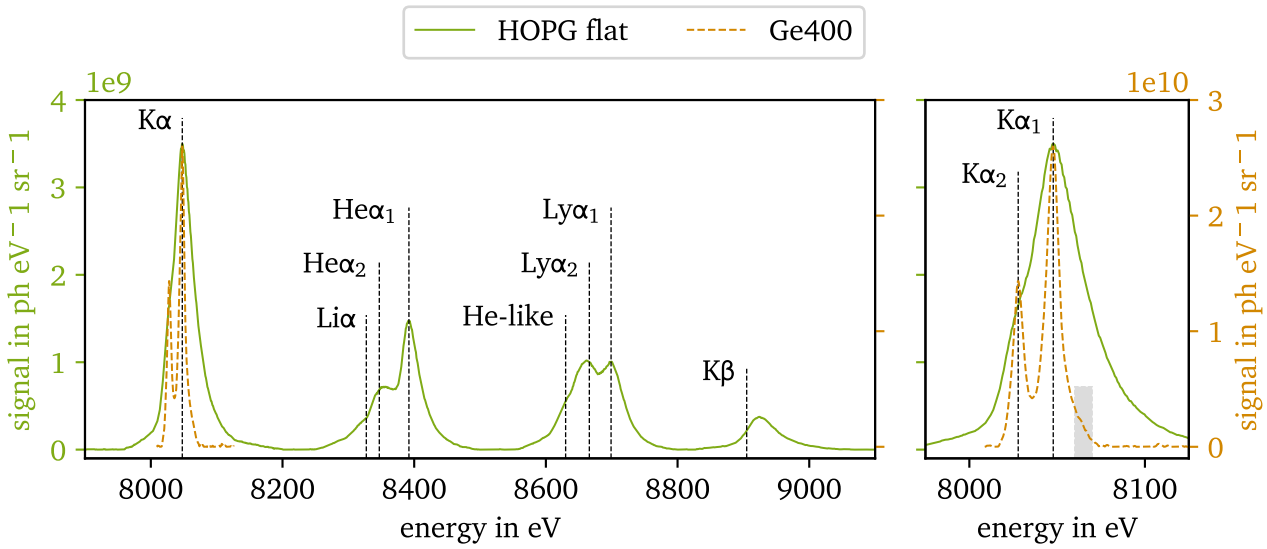

Figure 6.2: Spectral emissivity of the pure Cu target. The emission from both weakly ionised material ($K\alpha$, $K\beta$) as well as from highly ionised material (Heα, Lyα) is observed. A small high energy wing around $8065\,\mathrm{eV}$ indicates some ionisation of the M-shell. The signal height between the two spectrometer differs by almost one magnitude. This is attributed to an under-estimation of the germanium (Ge) crystal reflectivity, leading to an over-estimation of the signal strength (see section 6.2.2).

Together with the emission from weakly ionised material is substantial emission from highly ionised material detected. The He-like transitions from the singlet and triplet state at $8392\,\mathrm{eV}$ and $8347\,\mathrm{eV}$, respectively, are well resolved. An additional lower energy wing indicates the presence of Li-like and Be-like states. However, no substantial radiation between the $K\alpha$ and Heα radiation is found. Radiation in this energy regime is expected to occur with the formation of a large pre-plasma formation from ns exposure, which produces a wide distribution of ionisation states. The observed behaviour is explained with the high contrast of the PHELIX laser, which leads to little pre-plasma formation [Wag+14]. Towards higher energies, the doublet state transitions of H-like Cu atoms are measured as well. Both the Lyα_1 at $8699\,\mathrm{eV}$ and the Lyα_2 at $8666\,\mathrm{eV}$

[Tho+09] Thompson et al. (2009), *X-Ray Data Booklet*.

are resolved, again with a slight blue-wing detectable around $8630\,\mathrm{eV}$. The peak ratio of Lyα_2/Lyα_1, which is close to unity, is a clear indication that the Lyα_1 line is optically thick. Together with the overall strong Lyα emission, which is at around $70\,\%$ of the Heα peak indicates a very high degree of ionisation. In fact, some of the front side plasma might be fully ionised, as no emission from this state is emitted and could be recorded. Other studies have shown that a ratio of Lyα/Heα close to one indicates bulk electron temperatures in the order of 1 to a few keV [Šmí+19]. Overall the spectrum displays the expected emission behaviour of a classical X-ray backlighter target driven by a relativistic laser pulse with high contrast.

6.1.3 Results from flat layered target

The spectra observed from the FLT are displayed in figure 6.3. In comparison with the above described spectrum of the Cu foil target, two drastic changes in the target emission behaviour can be observed. Primarily, no thermal lines are detected. Moreover, the cold *K*-shell emission is strongly reduced and the $K\beta$ line displays less shift towards higher energies.

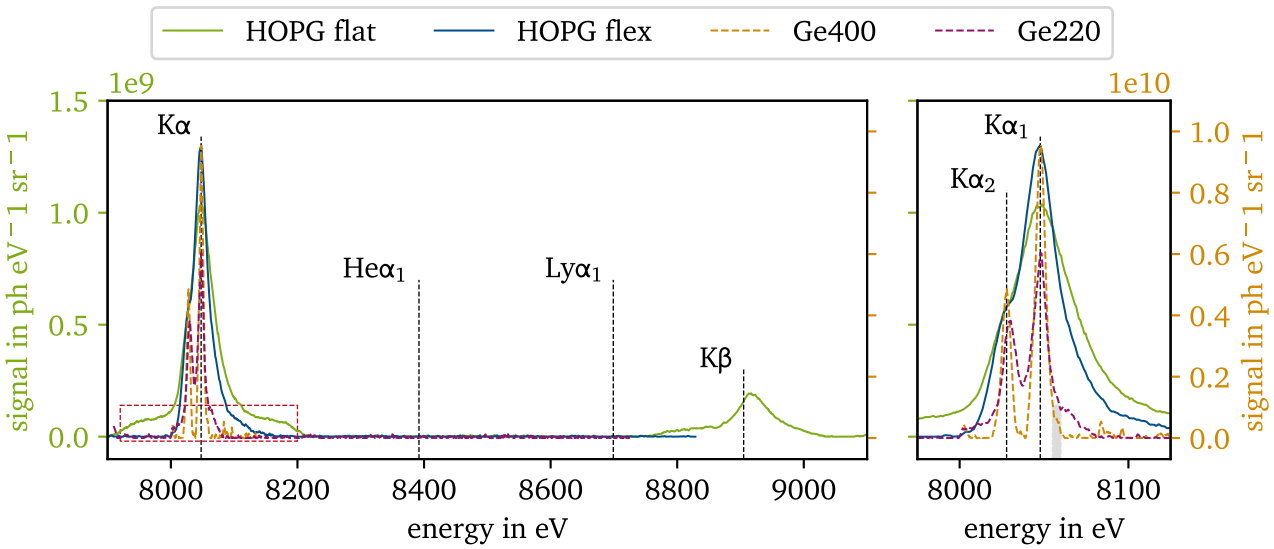

Figure 6.3: Spectral emissivity of the FLT. Only emission from weakly ionised Cu is observed. No thermal line emission is measured. The measurement of the flat highly oriented pyrolytic graphite (HOPG) spectrometer displays a large around the $K\alpha$ peak (red box), which is attributed to an artefact. As for the pure Cu target, a high energy wing around $8065\,\mathrm{eV}$ indicates some ionisation of the *M*-shell (gray box). The signal strength is much weaker than for the pure Cu target.

The absence of the thermal line emission is a clear indicator that the Cu layer of the target was not strongly heated during the laser target interaction. This is in agreement with other studies that have found the strong heating of relativistic laser pulses to be localised within the first few nm of the surface [The+06]. The here investigated target has a Si front side layer with a thickness of $15\,\mu\mathrm{m}$, much larger than the expected region of strong heating. Furthermore, the cold *K*-shell emission lines $K\alpha$ and $K\beta$ underline

[Šmí+19] Šmíd et al. (2019), "Characterization of suprathermal electrons inside a laser accelerated plasma via highly-resolved Kα-emission".

reduced heating of the Cu layer. On the one hand, the $K\beta$ is less shifted than for the pure Cu foil target. It is also much stronger in relation to the $K\alpha$ emission with a relative peak height of $19\,\%$ and a relative integrated intensity of $25\,\%$. Close inspection of the $K\alpha_1$ peak (see figure 6.3 (b), Ge400 spectrometer) also shows a decreased high energy wing, extending only to about $8060\,\mathrm{eV}$. While all these features indicate some degree of ionisations through collisions from the hot electrons, the mean ionisation is expected to be lower than for the pure Cu foil. For a further quantitative analysis, the reader is pointed to section 6.3. The large pedestal around the $K\alpha$ line emission visible in the spectra with the HOPG flat spectrometer (red box in figure 6.3) is expected to be a measurement artefact. This assumption is supported by the absence of a similar emission in the other three spectrometer.

Comparing the photon yield of the FLT with the pure Cu foil target, a clear decrease of about $70\,\%$ is observed. This decrease appears to be the result of an energy loss of the hot electrons in the Si front side layer of the target. While electron refluxing has been shown to be the driving mechanism of $K\alpha$ emission of relativistically driven targets [The+06; Neu+10], a short auxiliary consideration will be used to support this assumption.

One important quantity for the production of K-shell vacancies is the electron impact cross section for K-shell ionisation σ_K. For Cu, this cross section is plotted in figure 3.1 in section 3.1.1. The cross section rises sharply above the binding energy up to a maximum around $30\,\mathrm{keV}$, decreases again to a minimum at approximately $1\,\mathrm{MeV}$ before rising again. For Si, the behaviour is similar, however the maximum of σ_K is at $10\,\mathrm{keV}$. Assuming a typical electron spectrum for intensities of $10^{20}\,\mathrm{W\,cm^{-2}}$, as stated for example in [Neu+10; Cul+14], most electrons are expected to have energies in the order of a few $100\,\mathrm{keV}$ with small numbers reaching a few MeV. Each electron then moves repeatedly through the target, losing energy through collisions. The energy loss can be estimated through a Monte-Carlo simulation of the electron trajectories in Si and Cu, respectively. This is done with the CASINO code [Dem+11]. In figure 6.4, the energy loss of an electron in the two target layers is plotted over various initial energies of the electron. Electrons with energy of $<40\,\mathrm{keV}$ are stopped completely, while electrons with higher energy lose between 10 - $30\,\mathrm{keV}$ with each pass, depending on their energy. The loss is slightly higher in the denser Cu layer.

A simple multiple pass model is used to estimate the fraction of the total electron energy lost in the Si layer. The results of this model are displayed for varying starting energies in figure 6.4. The fraction oscillates strongly, depending on how often the electron refluxes before it is completely stopped. Depending on the final layer, the fraction lost in the Si front side layer is either larger or smaller, as the remaining energy of about $40\,\mathrm{keV}$ is completely deposited there. With increasing starting energy, the amplitude of this oscillation is dampened, as the last energy portion of $40\,\mathrm{keV}$ represents a smaller portion of the starting energy. Even this simple model already predicts an energy loss due to the additional Si front side layer of roughly $47\,\%$. Not included in this model are additional losses, for example additional stopping inside the front side plasma, lost energy due to escaping electrons and disruptions of the electron transport along the Si/Cu interface. As such, the observed decrease of the $K\alpha$ intensity to about $70\,\%$ can be attributed to a large part to the energy losses due to the higher overall target thickness and the additional Si front side layer. Only the relative ratio of Si front side layer thickness to Cu back side layer thickness might impact the observed target performance. For example, a thicker Cu back side layer could increase the target performance. However, the gain is limited, as shown in figure 6.4. Here, a second test case with a $10\,\mu\mathrm{m}$ back side layer is shown as well. The target would still lose roughly $30\,\%$ of the electronic energy in the Si front side layer. The back side layer thickness can also not be increased indefinitely, as the thicker layer will reabsorb a larger part of the emitted $K\alpha$ radiation. An increase thickness will also reduce the

[Cul+14] Culfa et al. (2014), "Hot electron production in laser solid interactions with a controlled pre-pulse".
[Dem+11] Demers et al. (2011), "Three-dimensional electron microscopy simulation with the CASINO Monte Carlo software".

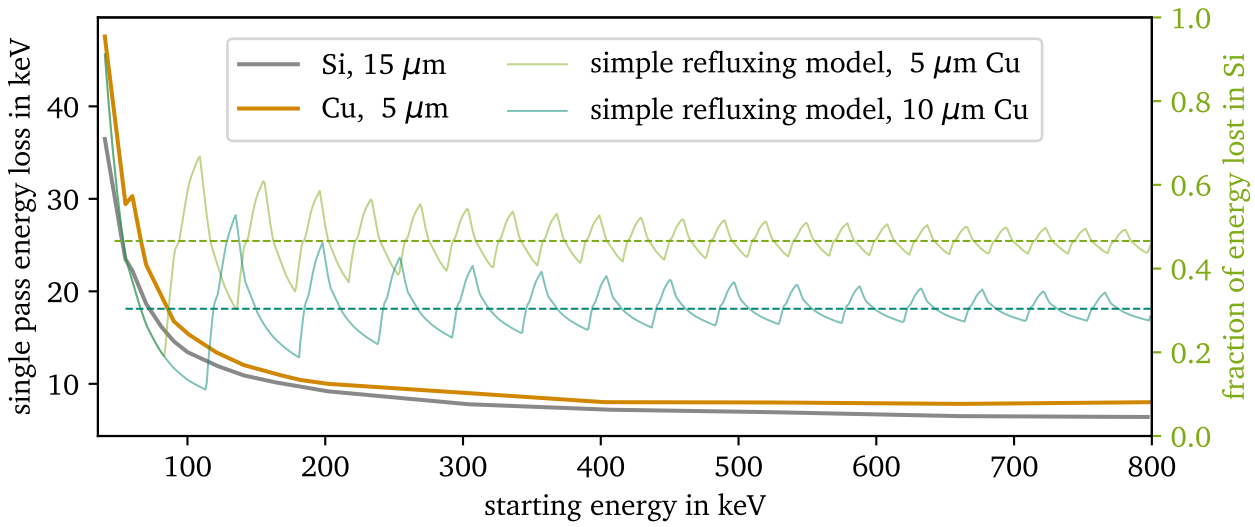

Figure 6.4: Simple refluxing model to estimate the energy loss in the silicon (Si) layer of the target. The single pass energy loss (solid gray and orange) display the estimated loss of energy due to a single pass through the respective layer of the target. The energy loss is estimated with the CASINO code [Dem+11]. A simple refluxing model is used to estimate the portion of energy lost in the front side Si layer of the target depending on the thickness of the Cu back side layer. For the in the experiments used targets, roughly $47\,\%$ of the energy is expected to be deposited in the Si layer.

refluxing of electrons. As discussed in section 2.4.3, the target should not exceed $75\,\mu\mathrm{m}$ for a $500\,\mathrm{fs}$ pulse. This leaves the front side microstructures as a viable alternative to increase the photon yield. The MLTs will be discussed in the following section.

6.1.4 Results from microstructured layered target

In figure 6.5, the spectra observed for the MLTs are displayed, averaged over 2 measurements for all detectors. The spectral emission of the MLTs is very similar to the emission observed from the FLT. A prominent $K\alpha$ line emission dominates the observed spectrum and the $K\beta$ peak is again slightly shifted towards higher energies. The $K\alpha$ peak is here much stronger than for the FLT, and on a similar level as the pure Cu foil. The maximal detected peak value of $(3.9 \pm 1.9)\,\mathrm{ph\,eV^{-1}\,sr^{-1}}$ is even about $10\,\%$ stronger than the emission of the pure Cu foil. However, some spread of the emission intensities is observed for the same target configuration, as indicated in figure 6.5. In part, this due to a large energy variation of the laser from shot to shot, for which the spectra are not corrected. The reader is referenced to section 6.2, where a more quantitative analysis of the varying target types is explored. Furthermore, each target configuration was measured at most twice at the same conditions, limiting somewhat the statistical significance of the here presented values. It should also be mentioned that the interaction of the laser focus with a spot size of $(6.4 \pm 1.2)\,\mu\mathrm{m}$ is highly sensitive to the specific position, where it connects with the microstructures, which are of similar size. In part, this will lead to some observed variation in the emission spectrum as well.

The $K\beta$ peak is much weaker in comparison with the FLT spectrum at an integrated intensity of only about $12\,\%$ when compared to the $K\alpha$. As mentioned above, this could be an indication of an increasing vacancy

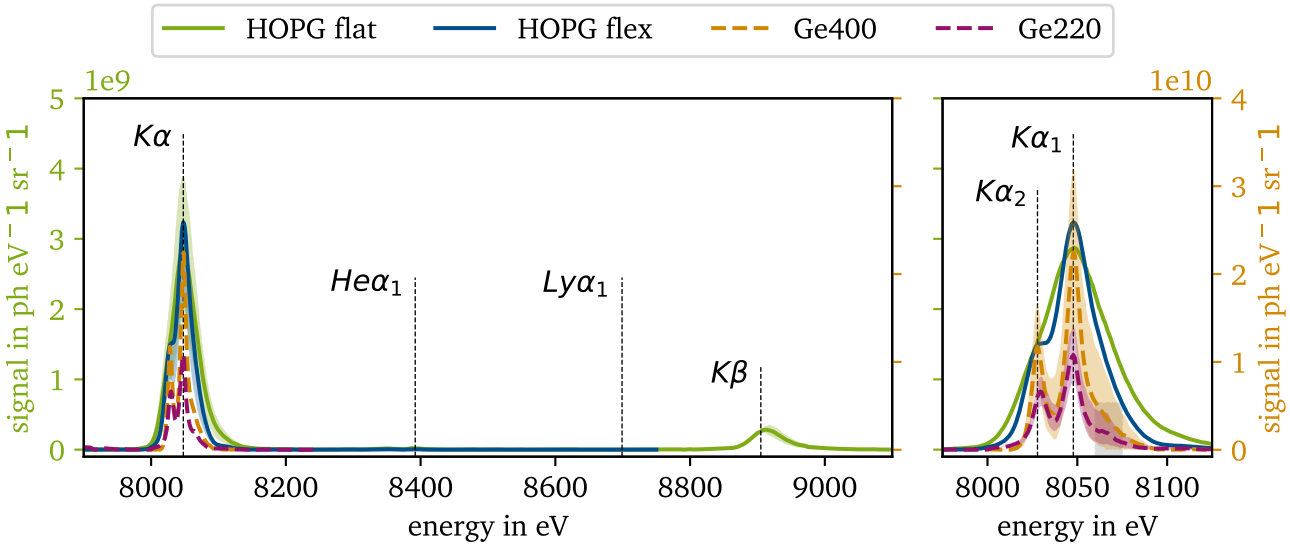

Figure 6.5: Spectral emissivity of the $15°$ MLT. The displayed spectra are averaged between to measurements (shaded coloured area). Similar to the FLT, no thermal line emission is observed. The $K\alpha$ peak is at a similar level as the pure Cu target. As for the other two target types, some emission between 8060 - $8075\,\mathrm{eV}$ indicates ionisation of the *M*-shell.

of the *M*-shell electrons due to a rising ionisation of the Cu atoms. A similar conclusion can be derived from the high energy wing visible for both Ge spectrometer around the 8060 - $8075\,\mathrm{keV}$, indicative of a strong *M*-shell ionisation. The quantitative analysis of these features with be the focus of the section 6.3.

As discussed in the previous section, a thicker Cu back side layer might have resulted in some additional gain of the emitted radiation by increasing the relative energy share deposited in the Cu back side layer. However, as the FLT and MLT target are constructed with the same areal density of the two layers, the here observed gain is most likely due to the changed distribution of the laser-accelerated electrons. This is a direct result of the modified front surface. To reach this boosted signal strength, either more electrons have to be accelerated or the accelerated electrons have to have more energy, depositing it over more refluxing cycles. A previous experiment conducted at the VULCAN laser system [Ebe+20], which used similar microstructured Si foils without any back side layer, gives some indication. In that experiment, the measured electron spectrum showed an increased flux by a factor of 3.1, while the electron temperature stayed roughly the same. Thus the former assumption appears the most likely. This additional electron flux is connected with a larger source size of the X-ray emission, as will be discussed in the following section 6.2.1.

6.2 Target performance

Following the qualitative discussion of the spectral emission, various quantitative aspects of the studied targets are the focus of this section. These include the $K\alpha$ source size and the conversion efficiency (CE) of laser energy to $K\alpha$ emission. These values are discussed with respect to target type and amplified spontaneous emission (ASE) contrast of the laser system.

6.2.1 Source size measurements

The spatial extent of the $K\alpha$ emission region is measured in one direction with the help of the imaging spectrometers. The found values are displayed in figure 6.6 over the various layered target types. A strong increase from the laser spot size of $(6.4 \pm 1.2)\,\mu\mathrm{m}$ to at least $140\,\mu\mathrm{m}$ is observed. This source size is much larger than for other recorded source sizes of simple foil targets, which typically ranges for similar laser foci between 50 - $90\,\mu\mathrm{m}$ [Par+06; BKN19]. This increase from the initial laser focus size can be explained with the movement of the refluxing electrons. While their movement is complex, the reflections at the strong electric field on the rear side (sheath field, see section 2.4), and additional collisions with the bound electrons, lead to trajectories out of the forward direction [Tow+05]. There remains however an additional increase of about 2 from the in the literature given source sizes to the here measured ones. An explanation for this much larger source size might be a deflection of the hot electrons at the Si/Cu interface, as suggested by the work of Gremillet *et al.* [GBA02], leading to a strong fragmentation of the electron beam. Furthermore, as mentioned in section 5.1, the focus of the PHELIX laser displayed a coma-like aberration which distributed up to $60\,\%$ of the laser energy to a larger region. Thus, part of the increased source size can also be attributed to this larger laser focus.

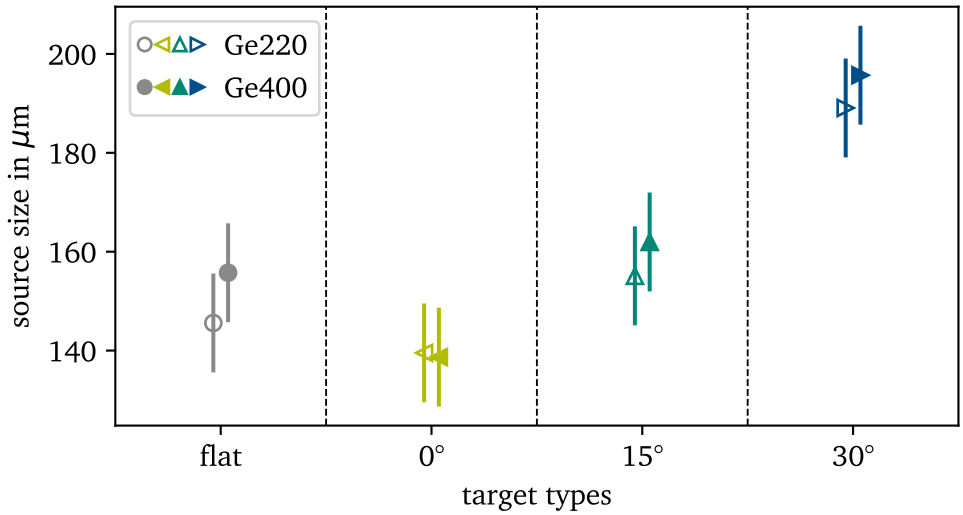

Figure 6.6: Source size for all layered target types. The measurements of the two imaging spectrometer agree very well for each target type. Overall, the source sizes are much larger than the laser spot. A almost linear increase of the source size with microstructure tilt from 0 - $30°$ is observed.

There is also a clear dependence of the source size with the target type, measured by both spectrometers. In particular an almost linear rise of the source size with the microstructure tilt angle is observed. It is assumed that the microstructures influence the area of interaction of the laser with the target. For the $0°$ target, the laser is guided by the cone-like structures, which in turn strongly limits the surface area. As the microstructures are tilted away from the principle laser axis, the laser cannot penetrate as deeply, interacting more with the upper part of the microstructures. This increases the overall surface area on the target, which in turn increases the observed source size. Comparing these values to the base value for the FLT, the additional focusing due to the aligned microstructures leads to a smaller source size by roughly $15\,\mu\mathrm{m}$. On the other hand for the $30°$ MLTs, source size increases to about $200\,\mu\mathrm{m}$.

[Tow+05] Town et al. (2005), "Simulations of electron transport for fast ignition using LSP".
[GBA02] Gremillet et al. (2002), "Filamented transport of laser-generated relativistic electrons penetrating a solid target".

6.2.2 Conversion efficiencies

A significant value to describe the performance of a target is the CE, as described in section 3.1.5. This value is defined by the ratio of emitted X-ray energy to deposited laser energy. For the former, the value can be derived by integrating over the respective spectral range in the calibrated spectrum. While this value is a commonly used measure to compare different target types, care has to be taken for the following reasons. Primarily, it has been shown that the CE depends on the laser intensity. Similarly, while the CE is normalised to the laser energy, a systematic difference has been observed for different laser systems and in particular for different pulse lengths (for example mJ-fs-class lasers) [Par+06]. Lastly, most references assume an isotropic emission of the X-ray radiation into 4π [Par+06; GR09; Neu+10], while others give the values for the half space 2π [FK16] or do not specify it [Tom+11; BKN19]. However, as has been shown by Borm *et al.* [BKN19], the assumption of isotropic emission and subsequent scaling to 4π is reasonable, and will therefore also be done to the here presented data.

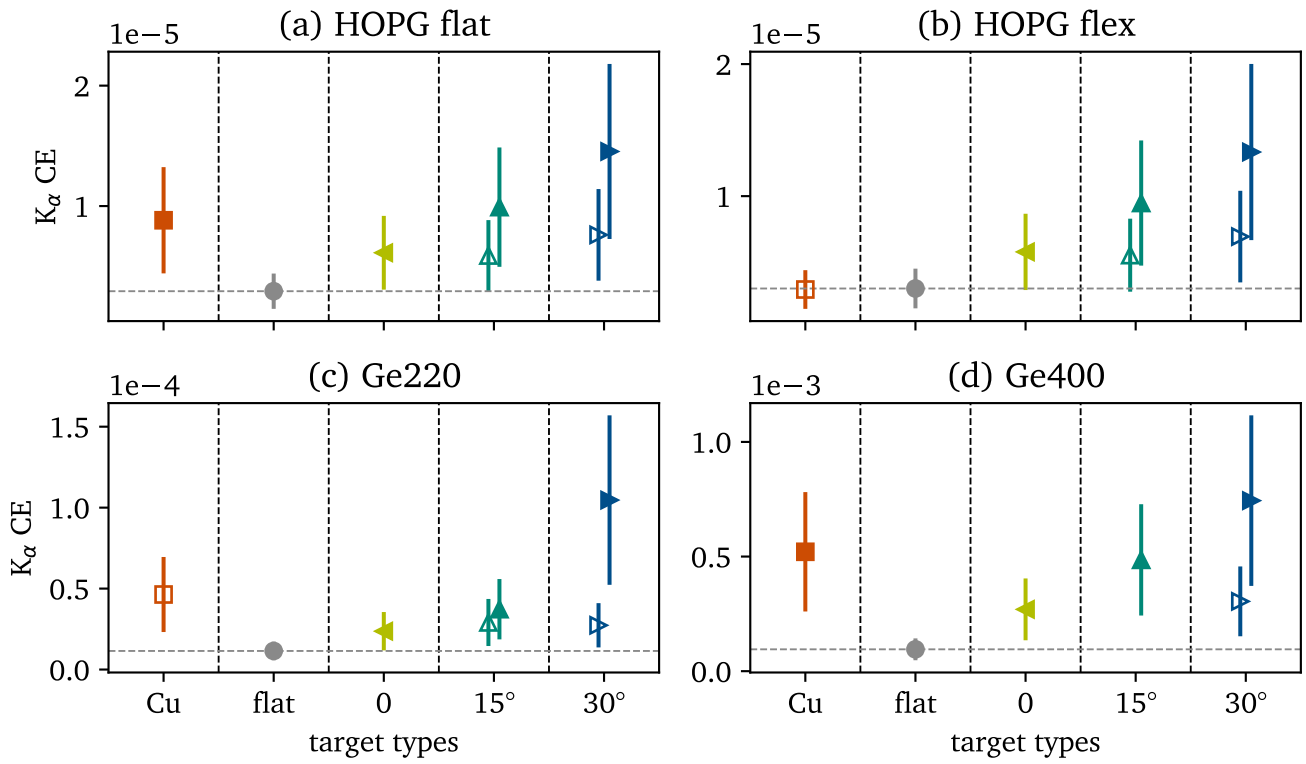

Figure 6.7: CE over target type for all spectrometer. The lowest CE is measured for the FLT. As for the source size, an almost linear increase of the CE is measured with microstructure tilt. The $15°$ MLT performs roughly equal to the pure Cu target. The CEs for the Ge spectrometer is much larger, most likely due to an under-estimation of the reflectivity, leading to an over-estimation of the $K\alpha$ signal. The large uncertainty is due to the assumed uncertainty of $50\,\%$ when deriving the absolute photon numbers. The empty symbols represent not finally aligned spectrometer in case of the pure Cu target or strong thermal line emission (in case of the MLT). The latter indicates a direct interaction of the laser with Cu. These values are therefore excluded from any further analysis.

[Tom+11] Tommasini et al. (2011), "Development of Compton radiography of inertial confinement fusion implosions".

In figure 6.7 (a), the CE $\eta_{K\alpha}$ into $K\alpha$ radiation are displayed for the investigated target types. The in section 6.1 discussed trends can also be observed for the CE of the pure Cu, the flat layered and the $15°$ MLT. Furthermore, an influence of the microstructure tilt on the $K\alpha$ emission can be observed as well. While a tilt of the microstructures towards the principle laser axis (0°) leads to a slightly reduced $K\alpha$ emission, the opposite effect is observed when slanting the microstructures away (30°). This difference in emission can be, for the most part, explained by a varied interaction surface due to the changed orientation of the microstructures that results in a changed source size (see section 6.2.1).

Comparison between the four spectrometer (figure 6.7 (a)-(d)) displays very similar trends with respect to the target type as expected. The overall values of $\eta_{K\alpha}$ are however diverging. In particular for the two spectrometer that used a Ge crystal, the stated $\eta_{K\alpha}$ is much larger at values of about 5×10^{-5} and 5×10^{-4} for the Ge220 and Ge400 spectrometer, respectively. On the other hand the values for the two HOPG spectrometer agree reasonably well within the error margin. The suspected reason for this discrepancy is the estimated integrated reflectivity R_{int}, in particular of the Ge crystals. Therefore, the $\eta_{K\alpha}$ of the HOPG spectrometer is expected to be more reliable.

As a whole, a value of about 10^{-5} is on the lower end of the regime of other studies, which found values up to a few 10^{-4} for similar experiments [Par+06; GR09; Neu+10]. In particular for the high intensities used in the experimental campaign ($> 10^{20}\,\mathrm{W\,cm^{-2}}$), the measured CEs are rather small [Par+06]. One explanation for this observation can be found in the work of Neumayer *et al.* [Neu+10], which studies the effect of refluxing on the $K\alpha$ yield. There it is shown that for high intensities above $10^{19}\,\mathrm{W\,cm^{-2}}$, a free standing foil performs much better than a substrate backed foil that will hinder electron refluxing. In particular, free standing Cu foils with a lateral dimension of $2\,\mathrm{mm}$ and a thickness of $10\,\mu\mathrm{m}$ were used to achieve a high CE. On the other hand, the pure Cu foil target used in this work achieved a much lower CE. As the thicknesses of the Cu foils are the same, the mounting and the larger lateral dimension of $1.5\text{x}5\,\mathrm{mm}^2$ are suspected to have decreased the performance. Smaller lateral dimensions together with a less massive mounting are therefore expected to increase the CEs of the targets even further.

It should also be mentioned that for two of the measurements done with the MLTs, thermal line emission was observed. This is presumably due to small holes in the base of the microstructured Si layer, an artefact of the target fabrication process. This leads to a direct interaction of the laser with the Cu, locally generating much higher ionisation states. It is therefore assumed that these targets are not representative of the performance of the MLTs. This assumption is also supported by the recorded CEs, which are lower for these two measurements (see figure 6.7, empty symbols).

The CEs can now be combined with the measured source sizes, which are discussed in the previous section 6.2.1. A clear increase with microstructure tilt was observed for both variables in the sections above. Normalizing the CE to the source size leads to an reversal of this observation. In figure 6.8, these values are displayed for the layered target types. The strong increase of at least 2.7 in CE per emitting area with the microstructured front surfaces is clearly seen for all MLTs. The highest photon flux is achieved with the $0°$ MLT. As discussed for the source size, it is assumed that the laser interacts much deeper inside the microstructure valleys in case of the $0°$. This leads to the higher photon flux, as the electrons have to travel through a thinner layer of Si and thus on average experience less collisions.

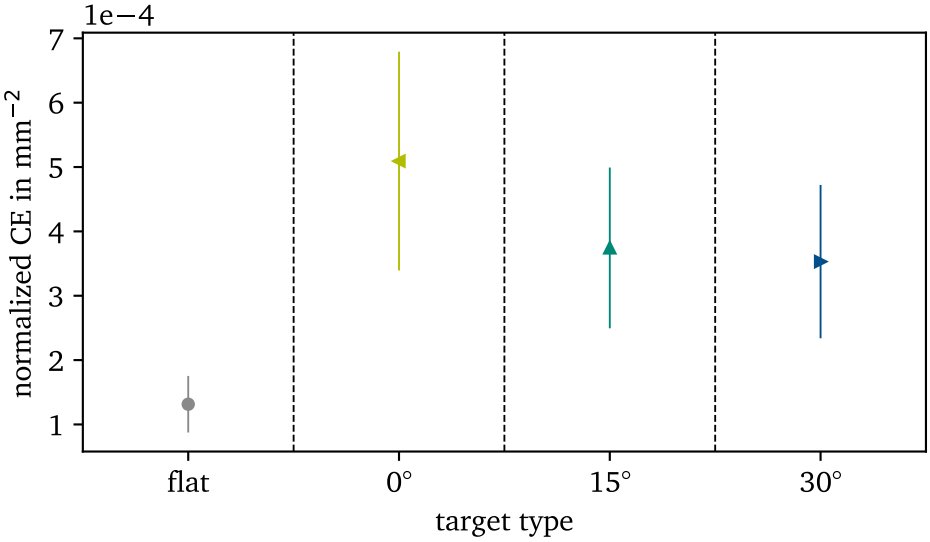

Figure 6.8: CE normalised to source size for the various layered targets. The lowest photon flux is observed for the FLT. For the MLTs, the smaller source size for the aligned microstructures leads to the highest photon flux, even though the pure CE is the lowest for this target. With increasing tilt angle, the photon flux decreases as the source size increases (see figure 6.6.

6.2.3 Influence of ASE contrast

In the previous sections, the influence of the microstructure tilt is discussed. Besides this variation on the target side of the experiment, the influence of the ASE contrast on the laser side of things is the focus of the following section. As described in section 5.2, the ASE contrast was changed by adjusting the amplification factor of the ultrafast optical parametric amplifier (uOPA) to three different levels (see also figure 5.3 in section 5.2). For each of these three contrasts, three different target types are investigated, namely the FLT, the $0°$ MLT and the $15°$ MLT.

In figure 6.9, the measurements for the different contrast levels are displayed. For the highest contrast of 1.1×10^{12}, the measurements correspond to the previously discussed CEs (see section 6.2.2). For the medium (1.8×10^{10}) and low contrast (3.5×10^{7}), a clear decrease in target performance of the MLTs is observed. While the CE of the FLT stays roughly the same between the low and high contrast, no increase if found when modifying the front surface. It is therefore assumed that even at the medium contrast, substantial pre-plasma formation occurs. This plasma expands into the space between the microstructures, prohibiting any geometric advantages of the cone-like microstructures. The laser absorption and hot electron acceleration is shifted from those mechanisms that rely on a sharp density boundary such as the Brunel absorption to those that occur in shallow density gradients, such as resonant absorption. While it was not measured during the here discussed experiment, it is assumed that the decreased CE is also due to less energy being absorbed and rather back-reflected for the medium and low contrast.

The source size was measured as well for the three ASE contrast levels. The results are displayed in figure 6.10. In comparison to the in section 6.2.1 discussed source sizes for the high contrast, a slight decrease in source size of both the FLT and the $0°$ MLT is observed with decreasing ASE contrast. One explanation of the smaller source size could be a smaller laser focus due to self-focusing of the laser in the expanding pre-plasma, as discussed by Wagner *et al.* [Wag+14]. The source size of the $15°$ MLT on the

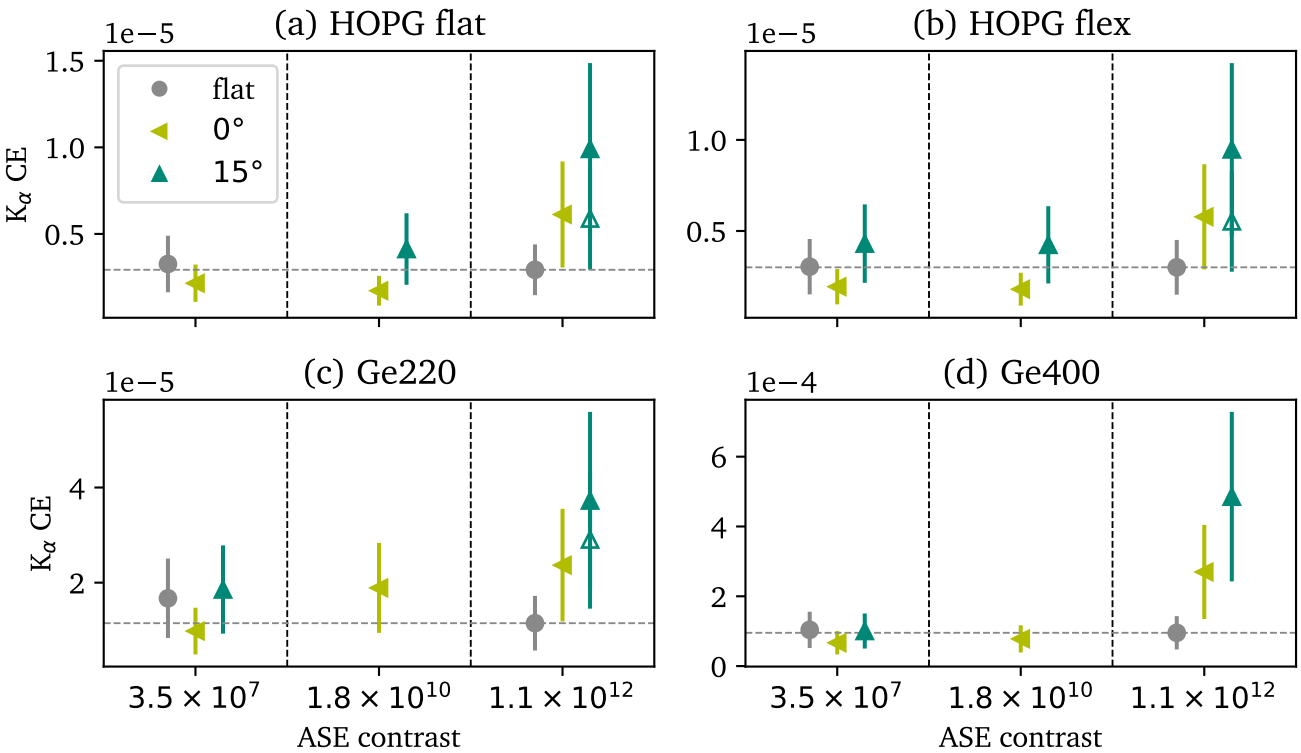

Figure 6.9: CE for varying levels of ASE contrast of the PHELIX laser. A clear decrease in target performance is observed for both the medium and low contrast. This is attributed to a stronger pre-plasma formation, resulting less hot electron production for the same energy. The higher CEs of the Ge spectrometers is a result of an underestimated R_{int} for the Ge crystals.

other hand stays roughly the same between low and high contrast. As the laser cannot penetrate as deep into the microstructure valleys due to the $15°$ tilt, the pre-plasma expansion is expected to occur further from the microstructure base as compared to the $0°$ MLT. Thus the hot electrons are accelerated further from the back side layer and will spread further than for the other two target. As a result, the source size increases drastically even with some self-focussing of the laser in the expanding pre-plasma. Another interesting aspect is that for the lowest contrast of 3.5×10^7 little difference between the $15\,\mu\text{m}$ thick flat Si layer and the aligned microstructures is observed. This further supports the assumption that for the lower contrasts a substantial pre-plasma formation prevents any geometrical advantages and the MLTs act similar to a flat surface.

6.2.4 Source size limited targets

In addition to the above discussed layered targets, some additional measurements were performed with the in section 4.3 described dot targets. For these targets, the Cu back side layer consisted of only two small Cu dots. The key parameters of these dots are a diameter of $(100 \pm 10)\,\mu\text{m}$ for each dot, with a distance center to center of $(250 \pm 10)\,\mu\text{m}$ between the dots. The objectives with these targets are the limitation of source size through material constraints and the demonstration of spatially separated sources with a singular target. Both of these objectives are achieved, as is discussed in the following.

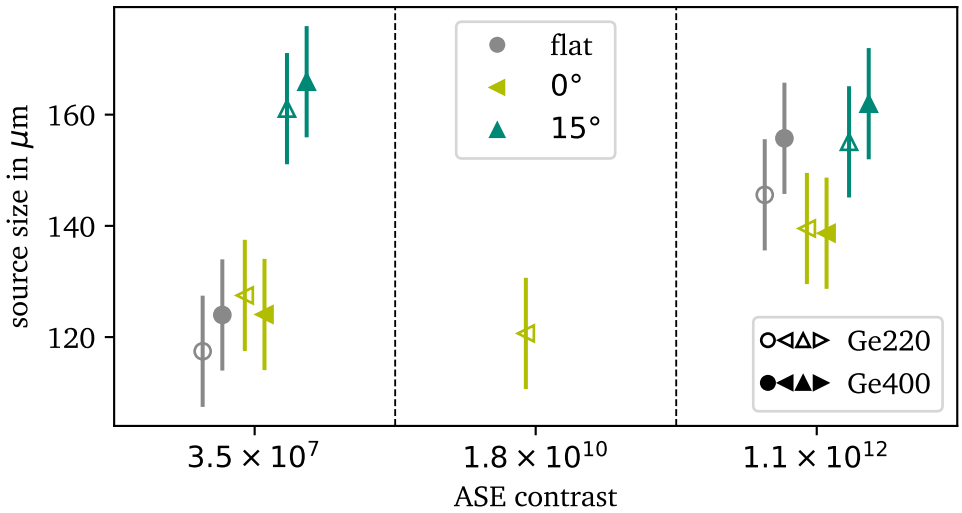

Figure 6.10: Source sizes for varying levels of ASE contrast of the PHELIX laser. The source sizes for the highest contrast correspond to the values discussed in section 6.2.1. For the medium and low contrast, the source sizes of the FLT and the $0°$ MLT decrease slightly. The source size of the $15°$ MLT stays roughly the same for the low and high contrast. No measurements for the FLT and $15°$ MLT were possible for the medium contrast, as the spectrometers were not finally aligned for optimal spatial focussing.

Before the advantages of the dot targets are discussed, one major drawback has to be mentioned: the overall CE. In figure 6.11, the CEs for both the flat and the $15°$ microstructured dot target are displayed. A clear increase with a microstructured surface is visible for these targets with about the same factor as has been found for the full layered targets with a $15°$ tilt. This again underlines the improvement that can be achieve through front side modification with cone-like microstructures. The CE for the dot targets is however over one magnitude smaller than for similar targets with a full Cu back side layer. One reason for this is the miss-alignment between laser focus and dot position on the backside. By design is the laser adjusted to interact centrally between the dots, so that both Cu volumes are equally traversed by hot electrons. This leads however to a large portion of the electrons, which are mainly accelerated in forward direction of the laser, to only reflux through the Si. Thus only electrons with a sufficiently strong deflection will reach the small Cu volumes, and will most likely have lost some energy already in collisions that resulted in the required deflection. Second to this is also simply the smaller volume of Cu that can generate the $K\alpha$ radiation. Assuming two dots of diameter $100\,\mu\mathrm{m}$, one would expect a decrease in $K\alpha$ emission of $22\,\%$ when comparing it to a source size of $160\,\mu\mathrm{m}$, as has been measured for the $15°$ MLT. Further development has to be done to optimize these target with respect to $K\alpha$ output, improving refluxing of the electrons and, if only one source is required, a direct alignment such that forward accelerated electrons interact with the small volume.

Nonetheless, the here discussed proof-of-principle targets also showed quite good results with respect to the above described objectives. In figure 6.12 (a), the recorded, spatially resolved spectrum of a dot target is shown. Besides the clear separation of the $K\alpha_1$ and $K\alpha_2$ peaks, the spatial separation of two sources can be seen. The laser was aligned to hit the target centrally between the two dots. The electron are accelerated in forward direction, as discussed above, and the laser interacts with the target surface under $15°$ to normal incidence. Thus, due to the central alignment, one dot experiences a stronger flux of electrons, resulting in a strong signal for, in this case, the upper spectrum.

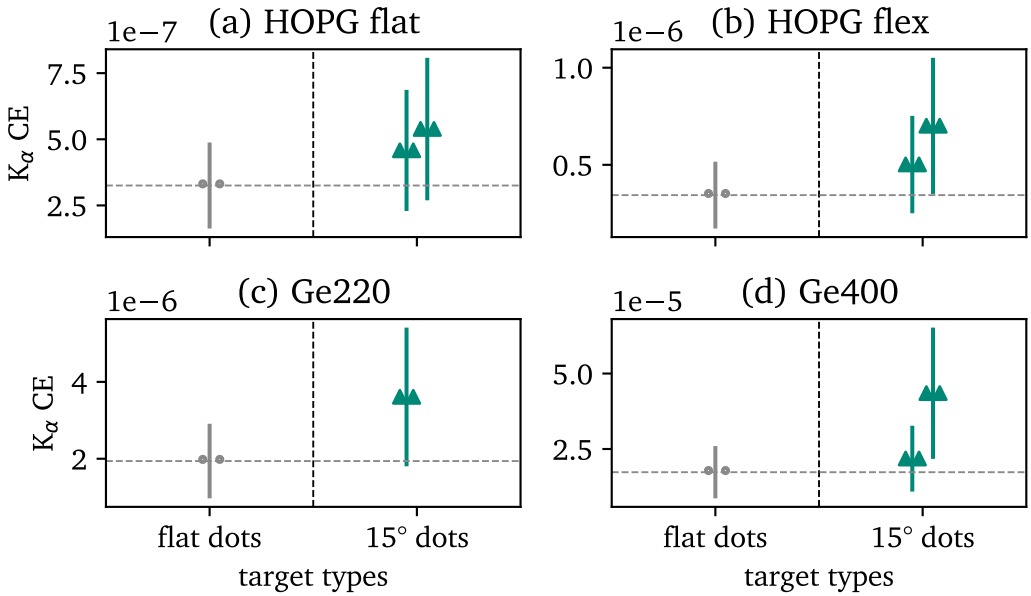

Figure 6.11: Measured CE for the dot targets. An increase with the microstructured front surface is observed with all spectrometer. Overall, the CEs are much lower than for the full layer targets.

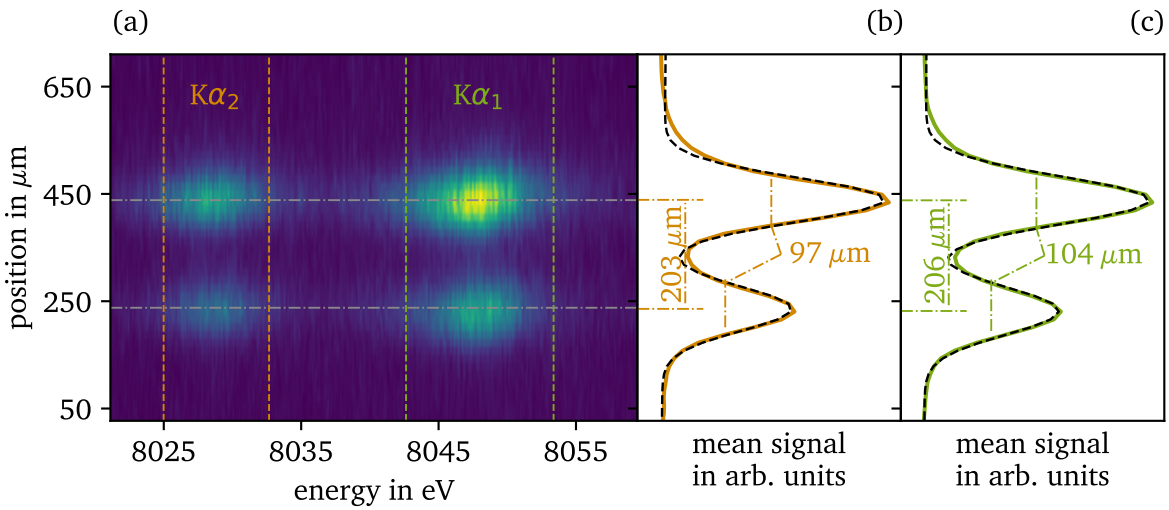

Figure 6.12: Spatially resolved spectrum of a dot target (a) together with the horizontal summation of the $K\alpha_2$ (b) and $K\alpha_1$ (c) peaks. The two sources are nicely separated vertically, with a good spectral resolution of the two $K\alpha$ peaks. The quantitative analysis is made with a double-Gaussian fit (black, dashed line) to the horizontal summation, leading to the measurements of center to center separation and individually source sizes. The latter are determined by the FWHM of the Gaussian fit. For both spectral peaks, the source size between the two dots is the same for the given precision.

Horizontal summation between the orange ($K\alpha_2$) and green ($K\alpha_1$) lines are shown in Figs. 6.12 (b) and (c), respectively. A double-Gaussian fit is used to determine the center to center separation and individual source size. The former is about $50\,\mu\mathrm{m}$ smaller than the manufactured center to center distance. It is assumed that this is the result of a slight rotation of the dots with respect to direction that the spectrometer resolves spatially. Thus the dots appear closer than they actually are. Another explanation could be that only part of each dot is actually emitting radiation, shifting the observed peaks closer together. This however seems less likely, as the source sizes are very close to the manufactured size of $(100 \pm 10)\,\mu\mathrm{m}$. It is also surprising that for both spectral peaks the individual source size was the same with $(97 \pm 10)\,\mu\mathrm{m}$ for the $K\alpha_2$ and $(104 \pm 10)\,\mu\mathrm{m}$ for the $K\alpha_1$ peak.

6.3 Atomic radiative simulations

In the following section, the detected spectra are further analysed with the help of the atomic radiative code SCFLY and FLYCHK [Chu+17; Chu+05]. These codes are used to estimate the bulk electron temperature and density in the Cu back side layer. Multiple parameters have to be set to calculate the spectrum. These parameters will be described in the following section 6.3.1. A merit function of the agreement between simulated and experimental spectrum is then determined. The bulk electron temperatures are inferred with this merit function. The resulting bulk electron temperatures are discussed in section 6.3.2.

6.3.1 Set-up of the simulation

The set-up of each calculation requires several parameters. The primary parameters include the nuclear charge Z, the electron temperature in eV and the electron density. The latter is specified through the mass density ρ in $\mathrm{g\,cm^{-3}}$, from which the electron density is calculated through charge neutrality recursively. Besides the most basic parameters, two further options were used to modify the calculations. Included is the thickness of the sample d_{layer}, in order to estimate the strength of the opacity and a secondary electronic component to represent the laser-accelerated electrons that collide with the back side layer atoms. The incorporation of these two parameters is done as follows. To estimate the opacity, the code assumes a slab of thickness d_{layer}, given in cm, and infinite extend in the lateral dimensions. For the layered target designs, this value is simply the back side layer thickness of $5\,\mu\mathrm{m}$. For the pure Cu foil, the initial thickness of $10\,\mu\mathrm{m}$ will not be completely heated to the high temperature expected from the spectral emissivity that was observed during the experiment. For that reason a comparison of the spectral emissivity for varying d_{layer} is displayed in figure 6.13 (a). In the regime between 1 - $10\,\mu\mathrm{m}$, no change of the qualitative spectral form is observed. Only the intensity increases with a larger thickness. As the spectra will be mainly compared after normalization, the spectra calculated with a thickness of $d_{\text{layer}} = 5\,\mu\mathrm{m}$ are used.

Relevant for all calculations is the secondary electronic component, which is defined with an additional temperature and a fraction of the total number of electrons. The influence of both parameters is investigated as well and the results displayed in figure 6.13 (b). The temperature can be estimated with equation (2.16) and is assumed to be $1.5\,\mathrm{MeV}$. Similarly, the fraction of electrons is typically estimated in the range of 0.01 - $1\,\%$. In comparison to the electron temperature, the calculated spectra are much more sensitive to the chosen fraction. This influence is however mainly limited to the thermal line emission, as for example investigated by Chen *et al.* [Che+09]. With respect to the cold K-shell emission, a variation of the hot

[Chu+17] Chung et al. (2017), "Atomic processes modeling of X-ray free electron laser produced plasmas using SCFLY code".

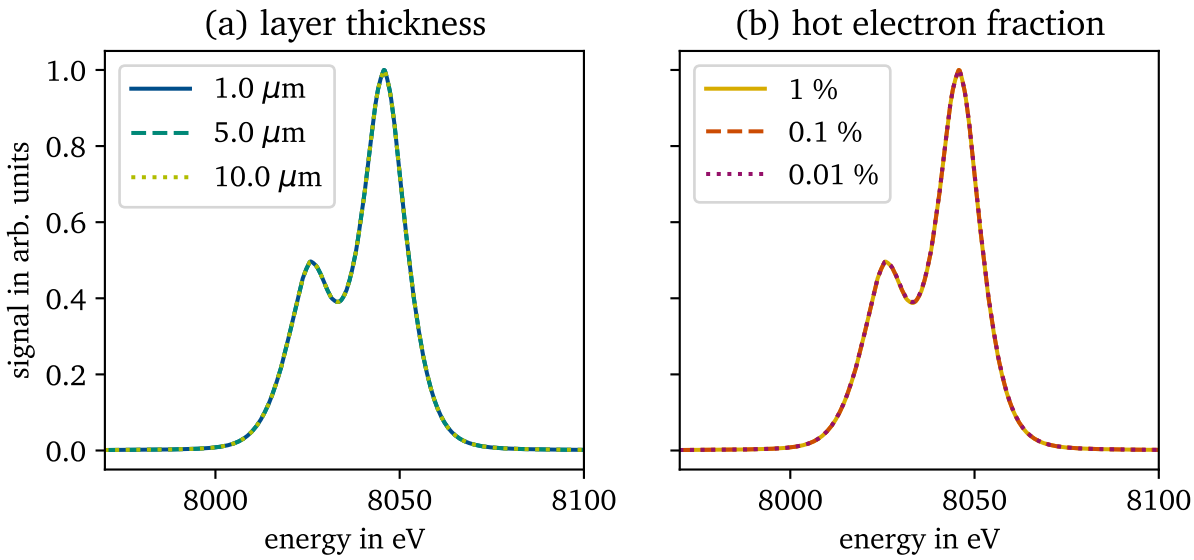

Figure 6.13: Influence of layer thickness (a) and hot electron fraction (b) on the resulting $K\alpha$ spectrum. The assumed layer thickness in (a) and hot electron fraction in (b) are indicated in the legend. For both parameters, no change in the spectral shape is observed with parameter variation.

electron fraction does not change the observed line shape, but rather only the intensity of the line. Overall, a fraction of $0.1\,\%$ of hot electrons with a temperature of $1.5\,\mathrm{MeV}$ were chosen for all following simulations.

Every experimental spectrum is modified by the observing spectrometer during the measurement. This transformation is due to the spectrometer specific point spread function (PSF), sometimes also called instrumental function, which typically imposes an additional broadening on the emission spectrum (see section 3.3.1). This PSF must therefore be corrected for before a comparison between a simulated and experimental spectrum can be done. For a rough estimation of the plasma parameters, in particular if more attention is paid to the peak ratios, typically a Gaussian function with a certain full width at half maximum (FWHM) can be used to approximate such a PSF. This is a valid approach for single crystals, like the Ge crystals used in this work. However, for the accuracy pursued in the following analysis, the ray-tracing code mmpxrt is used (see section 5.3). This code provides a much more accurate estimation of the PSF, which can be for example highly asymmetrical in case of mosaic crystals. An important value for the calculation of the PSF besides the used crystal and general spectrometer layout is the source size itself. A larger source size will lead to a much higher broadening of the observed spectrum. During the experimental campaign, the source sizes were measured (see section 6.2.1) and a mean source size of $150\,\mu\mathrm{m}$ was found (see section 6.2.1). Once the PSF is determined, two approaches can be used to compare the spectra. The experimental spectrum can be deconvolved or the simulated spectrum convolved with the PSF. Typically, it is much easier to calculate the convolution of two functions, for that reason the latter approach is chosen for this analysis. In figure 6.14, the calculated PSF of the HOPG flat spectrometer is shown together with a simulated and convolved spectrum.

Once the convolved spectrum is obtained, a measure of the similarity between this simulated spectrum to the experimentally observed one has to be defined. For every energy, the euclidean distance between the simulated spectrum S_{sim} to the experimental spectrum S_{exp} is calculated. This value is then weighted by the value of the experimental spectrum at this energy to focus comparison to the actual peak rather than the red and blue wing, which is more likely superimposed with other plasma states. The merit function is

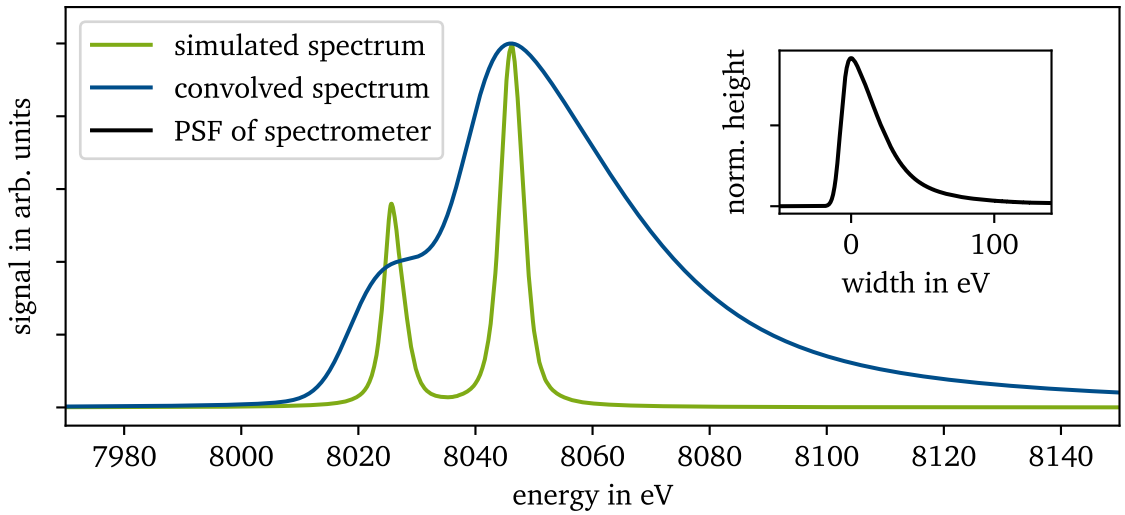

Figure 6.14: Effect of instrumental PSF on simulated spectrum. The influence of a relatively wide PSF on the simulated spectrum is shown. The PSF of the flat HOPG spectrometer (inset) is used for this, displaying how the clearly separated $K\alpha_1$ and $K\alpha_2$ cannot be resolved by this particular spectrometer.

thus defined as follows:

$$d\left(S_{\text{sim}}, S_{\text{exp}}\right) = \sqrt{\sum \left(S_{\text{sim}} - S_{\text{exp}}\right)^2 \times S_{\text{exp}}}. \tag{6.2}$$

This value can then be minimised through variation of the starting parameters, until a good agreement is found. The values of that simulation are then assumed to be the prevalent plasma state of the emitting region. Of course, as the measured spectrum is integrated over space and time, this will only result in an estimation of the mean value.

6.3.2 Temperature of the $K\alpha$ source

The main focus of this work is the $K\alpha$ emission from the weakly-ionised and still relatively cold region of the target. This radiation will therefore be analysed with more detail in this section. First, the general behaviour of the $K\alpha$ doublet is presented with the help of calculated spectra. Then an analysis for a singular measurement is discussed exemplarily. The section will conclude with more general statements on the differences between the targets.

As the material has to be weakly ionised in order to emit the classical $K\alpha$ line, a low bulk electron temperature in the emitting region of the target is expected. Together with this low bulk electron temperature, limited movement of the ions is expected, leading to a near solid density. The online available FLYCHK code, which has demonstrated great agreement with experimental data for highly ionised atoms of medium density, such as coronal plasmas [Chu+05], cannot be used for this cold and dense regime. The reason for this becomes quickly apparent from figure 6.15, where a calculation from FLYCHK for solid density Cu with a bulk electron temperature of $30\,\text{eV}$ is shown. The line width is grossly overestimated, most likely due to the limited atomic configurations used by the implemented super-configuration transition array (STA) model. For that reason, the code SCFLY is used for the analysis of the cold $K\alpha$ radiation [Chu+17]. The kinetics model of this code has been developed with X-ray free electron laser (XFEL) produced plasmas in

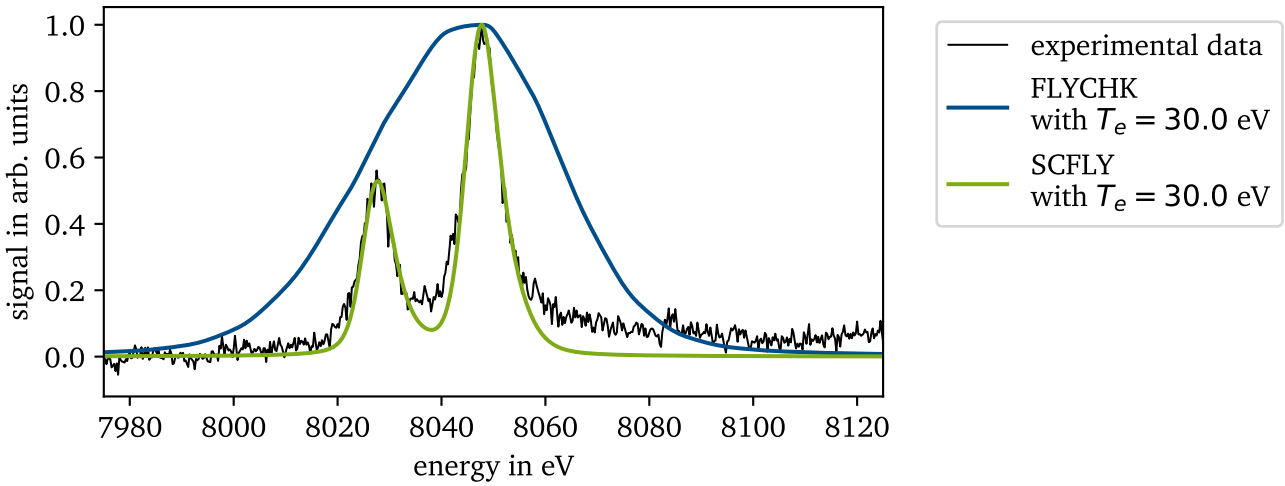

Figure 6.15: Comparison of spectra generated with FLYCHK and SCFLY together with experimental spectrum. The spectral emission of a $5\,\mu\mathrm{m}$ thick Cu slab of solid density and at an electron bulk temperature of $30\,\mathrm{eV}$ is shown as calculated by FLYCHK (blue) and SCFLY (green) together with an experimental spectrum recorded with the Ge400 spectrometer. The *K*-shell ionisation is driven by a secondary hot electron component with a temperature of $1\,\mathrm{MeV}$ and a share of $0.1\,\%$. The expanded set of atomic configurations implemented for the code SCFLY produces a much better agreement with the experimental data.

mind. Special care has been taken to expanded the set of atomic configurations needed when modelling solid density plasmas. In figure 6.15, a calculation with SCFLY with the same general parameters as the FLYCHK calculation shows a much greater agreement with the experimental data.

With the help of the code SCFLY, the behaviour of the $K\alpha$ line emission in dependence of the temperature T_e can be investigated. This is shown in figure 6.16. As a rough estimate, if the ionisation of the Cu atoms exceeds 19, electrons from the *L*-shell have to be ionised, leading to a stronger shift of the $K\alpha$ transition. To ensure that no substantial part of the material is ionised this high, the bulk electron temperature has to be well below $200\,\mathrm{eV}$. This can also be observed in figure 6.16, where for a temperature of $200\,\mathrm{eV}$ a strong blue wing develops with a clear satellite line emission around $8110\,\mathrm{eV}$. This is an indicator of a starting *L*-shell ionisation. As no such emission is observed around the $K\alpha$ peak in the experimental data, an upper bound of $200\,\mathrm{eV}$ for the bulk electron temperature can already be given.

Investigating the regime between 0.25 - $200\,\mathrm{eV}$ further, another aspect of the $K\alpha$ line emission is observed. The central energy of the $K\alpha$ line transition moves even without substantial *L*-shell ionisation. This movement is minimal for temperatures below $50\,\mathrm{eV}$, but increases strongly above this temperature. As the experimental data is calibrated with the $K\alpha$ peak as a fix point, this movement cannot be observed in the experimental spectra. In particular, for the regime between 10 - $50\,\mathrm{eV}$, the slight movement towards lower energies cannot be resolved with the given spectrometer calibration. For that reason, the peak width and shape are chosen as the criterion for the following analysis, while the calculated position is disregarded by shifting it to coincide with the experimental peak.

The results of such an analysis are discussed in the following on the basis of an experimental spectrum observed for a MLT. In figure 6.17 (a), the values of the merit function are shown over the temperature range of 0.25 - $200\,\mathrm{eV}$. A clear minimum can be observed around $(37 \pm 5)\,\mathrm{eV}$. The width of the dip also

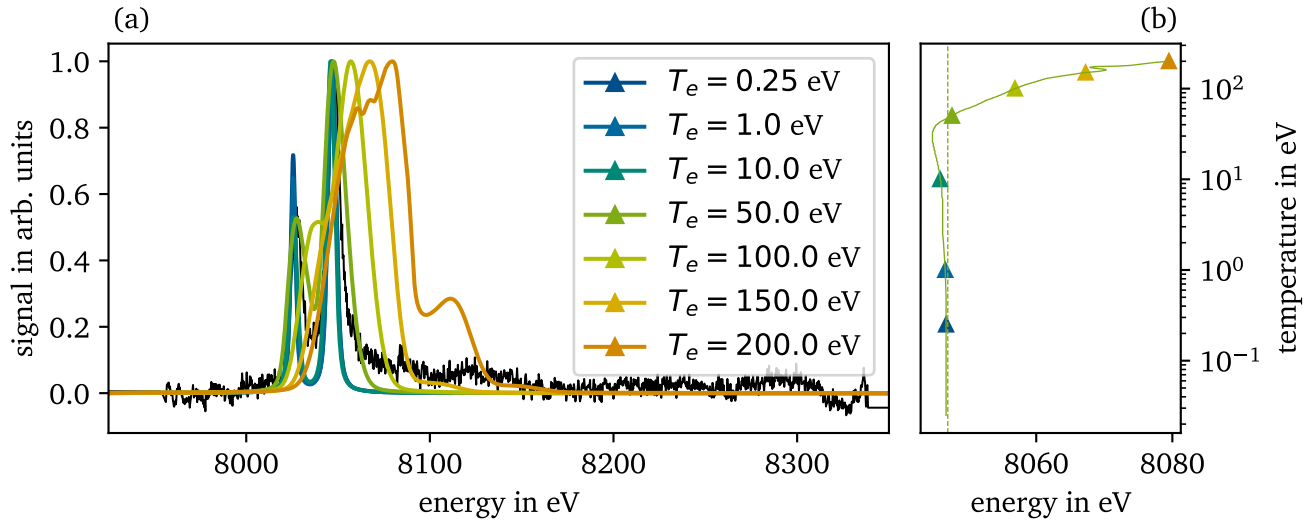

Figure 6.16: Spectral emission (left) and position of dominant *K*-shell emission (right) with varying bulk electron temperature. Starting with $50\,\mathrm{eV}$, a strong shift of the emission towards higher energies can be observed. At a temperature of $200\,\mathrm{eV}$, a satellite line around $8110\,\mathrm{eV}$ is already developed. Both changes are indications of a high *M*-shell and starting *L*-shell ionisation.

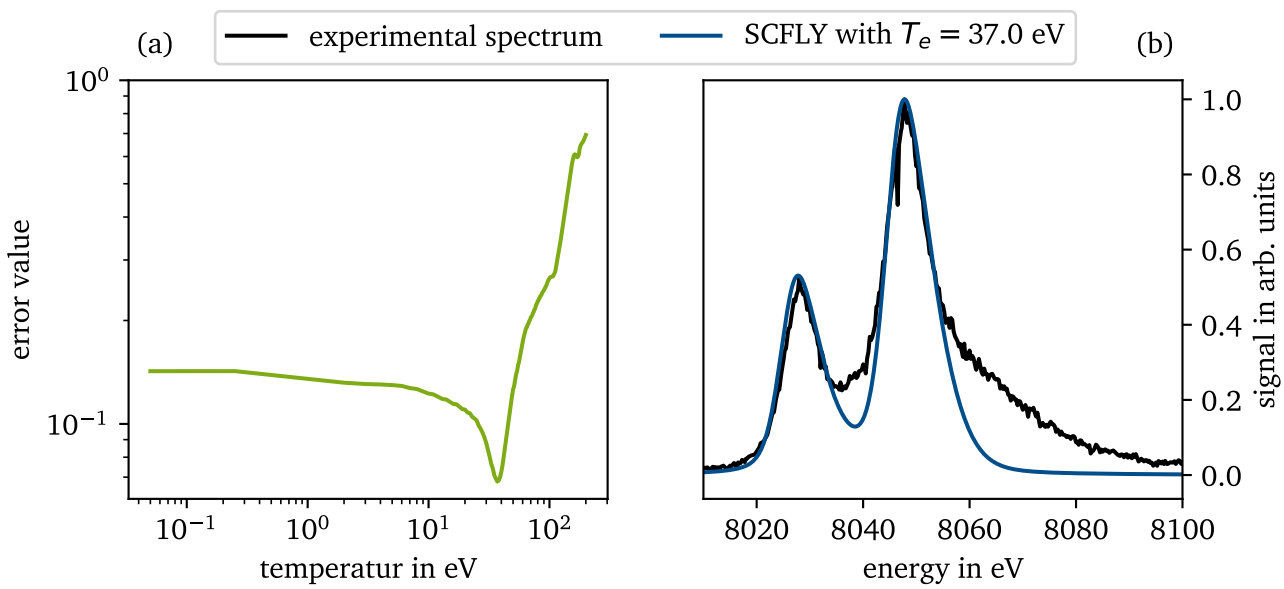

Figure 6.17: Values of the merit function over bulk electron temperature (a) and comparison of best fitting simulated spectrum to experimental measurement (b). The merit functions displays a clear minimum at $37\,\mathrm{eV}$. The corresponding simulation represents the peak shape of the experimental spectrum very good. The strong high energy wing of the $K\alpha_1$ peak is however not reproduced by a singular temperature.

indicates the accuracy of this analysis, with a FWHM of about $10\,\mathrm{eV}$. In figure 6.17 (b), the calculation corresponding to that minimum is shown in comparison to the experimental measurement. A very good agreement is found for the general peak shape as well as the ratio of the $K\alpha_1$ to $K\alpha_2$ peak, indicating that a temperature of $37\,\mathrm{eV}$ is a reasonable assumption for the average bulk electron temperature. However, the strong blue wing towards higher energies is underestimated with this singular temperature.

To model the blue wing of the peak, additional calculations with varying temperatures are added to form a composite model. In figure 6.18, such a composite model is displayed. In this case, temperatures in the range from 10 - $200\,\mathrm{eV}$ are chosen. However, the specific values given in figure 6.18 (b) should be understood as a representative of the general temperature range. The given percentages have to be understood accordingly, only giving an estimation of the possible electron distribution. In figure 6.18 (a), the corresponding relative ion population for the different temperatures is shown, scaled by the assumed percentages. In can be seen that roughly $50\,\%$ of the atoms are in the charge states Cu^{8+} and Cu^{9+}, with the remaining material mostly higher ionised between Cu^{10+} to Cu^{17+}. As expected, no ionisation beyond Cu^{19+} is observed. Overall the composite model represents the blue wing of the $K\alpha_1$ peak very well. However, with the addition of the multiple higher temperatures, the $K\alpha_2$ peak of the composite model is slightly worse in comparison to the pure $37\,\mathrm{eV}$ calculation seen in figure 6.17 (b).

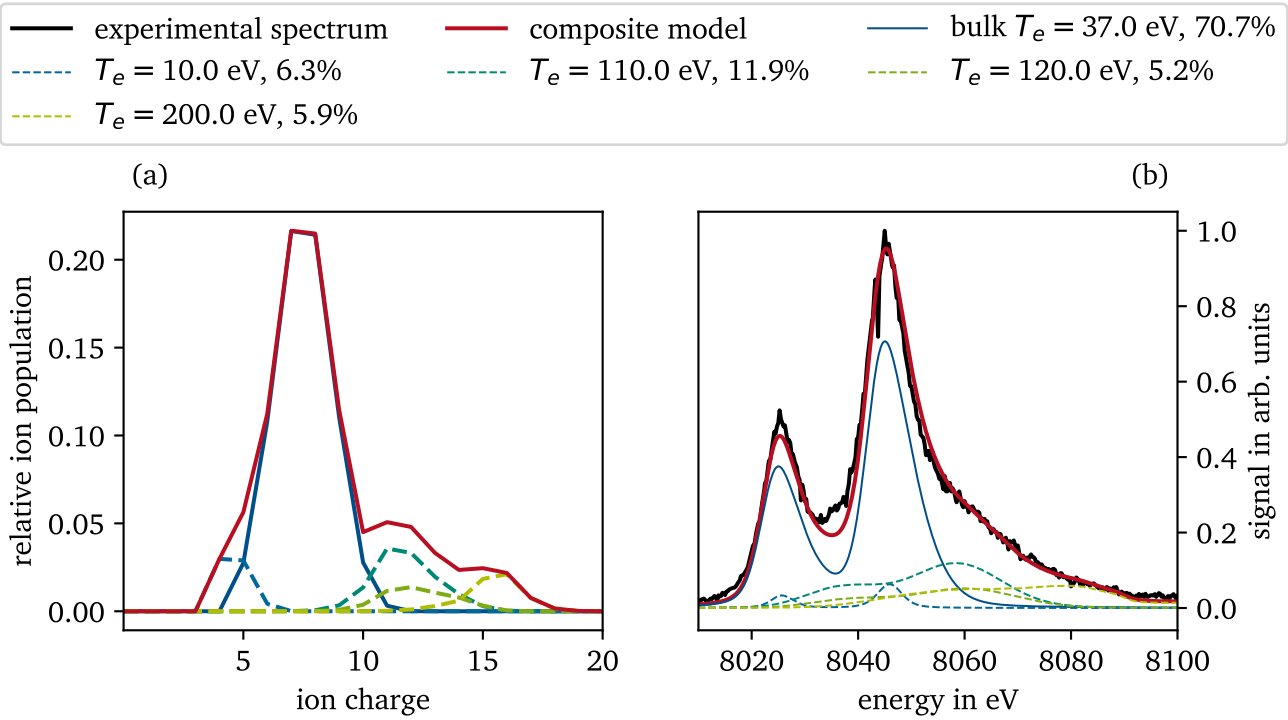

Figure 6.18: Relative ion population (a) and spectral shape of a composite model (b). The composite model is derived by addition of various simulations with temperatures between 10 - $200\,\mathrm{eV}$. This approach reproduces the high energy wing of the measured spectrum. The relative portions of material are derived from the scaling factors used to reproduce the observed spectrum. The modification to the relative ion population with this composite model mainly shows the additional higher ionisation states needed.

In comparison to the above discussed example, the composite model and corresponding relative ion population of a second experimental measurement is displayed in figure 6.19. This experimental spectrum, observed for a FLT, has a much less developed blue wing. The bulk T_e is also slightly smaller at $30\,\mathrm{eV}$, while the calculation is much closer to the experimental peak shape. This suggests a much larger portion of the emitting material to be well modelled with this averaged temperature. The composite model displayed in figure 6.19 (b) underlines this assumption, with mainly one secondary component at a temperature of $90\,\mathrm{eV}$. In addition, the composite model suggests a third temperature at $200\,\mathrm{eV}$. This is however due to the bump observed around $8080\,\mathrm{eV}$, which is most likely a spectrometer artefact rather than an actual feature. The lower temperature is also reflected in the lower overall ionisation, as displayed in figure 6.19 (a). Most of the material is in the range of Cu^{5+} to Cu^{9+}, with only a small portion at an ionisation of Cu^{15+} to Cu^{17+}. The latter is due to the falsely identified temperature of $200\,\mathrm{eV}$, and should therefore be disregarded. Thus, as expected from the much narrower peak, the analysis suggests much less heating within the Cu layer of the FLT. In the following, the influence of the target type on the found T_e and thus the observed bulk electron heating will be discussed.

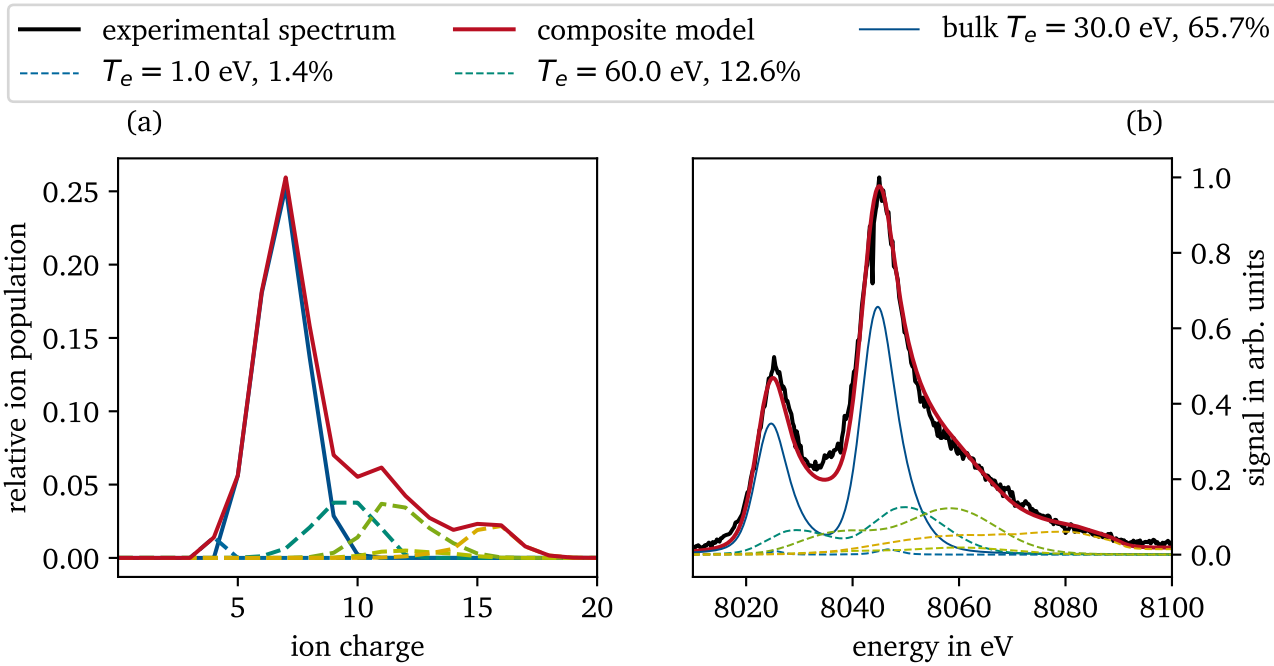

Figure 6.19: Relative ion population (a) and spectral shape of a narrower $K\alpha$ line (b). In comparison to figure 6.18, a less developed high energy wing results in a simpler composite model that only includes two additional temperatures. The high temperature of $200\,\mathrm{eV}$ is the result of the bump at $8080\,\mathrm{eV}$, which is an assumed spectrometer artefact.

In figure 6.20, the bulk electron temperatures are displayed over the investigated target types. The measured bulk electron temperature is a result from collisions of the laser-produced hot electron. As such, this temperature is an indicator of the amount of collisions that occurred. The temperature of the hot electrons is here dependent on the intensity on the target (see section 2.3), while the number of accelerated electrons also depends on the total laser energy irradiated on the target. Overall, the temperature range between 31 - $43\,\mathrm{eV}$ agrees well with the literature for similar experimental conditions [Nil+08; Nil+09].

[Nil+09] Nilson et al. (2009), "Bulk heating of solid-density plasmas during high-intensity-laser plasma interactions".

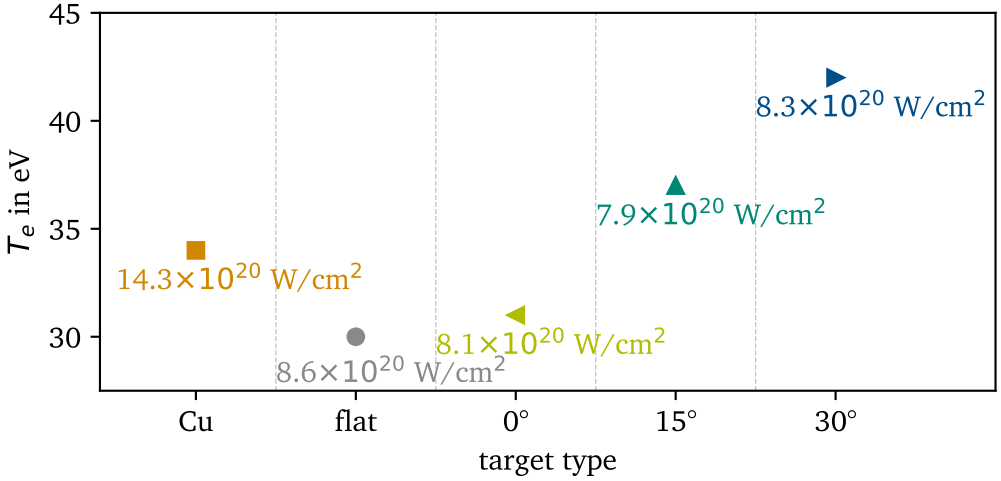

Figure 6.20: Bulk electron temperature for the investigated target types. The temperature variation with target type is remarkably similar to the variation of the CE into $K\alpha$ emission (see figure 6.7). This suggests a common cause for the amount of $K\alpha$ emission and the bulk electron temperature, which can be explained with the number of collisions in the Cu back side layer. This in turn is a result of the total number of accelerated hot electrons.

Comparing the temperatures of the pure Cu foil to the FLT, less heating of the bulk electrons is observed for the latter. This is a reasonable finding, as the laser-produced hot electrons have to travel through the $15\,\mu\mathrm{m}$ thick Si front side layer of the FLT. Partly, the electrons loose some energy before interacting with the Cu back side layer. The thicker target also leads to a larger spread of the electrons (see also section 6.2.1), further distributing the energy to a larger volume. Lastly, the intensity on the FLT was only about half of the intensity on the pure Cu target, leading to a reduction of the hot electron temperature of about $20\,\%$. Together, this leads to the observed decrease in bulk electron heating for the FLT.

A temperature very similar to the FLT is observed for the $0°$ MLT. This is surprising, as the two target types are geometrically very different. Previous studies by Ebert *et al.* [Ebe+20] have investigated the changed hot electron production due to the front side microstructures in comparison to flat surfaces. While no change in the temperature of the hot electrons is observed, the number of hot electrons is increased for the trough target. The increased number of hot electrons leads to a higher number of collisions in the Cu back side layer. Thus a higher bulk electron temperature is expected for the $0°$ MLT. This expectation is further underlined by the higher photon yield of this target type (see section 6.2.2) and the smaller source size (see section 6.2.1). However, the number of hot electrons is also dependent on the overall energy deposited on the target, which was only about $60\,\%$ in case of the $0°$ MLT, leading to the observed similar temperatures. Thus a slightly higher temperature would be expected for this target type in case of comparable laser energies.

For the MLTs, a clear increase of T_e with decreasing microstructure alignment is observable. All targets are driven with a similar intensity of around $8 \times 10^{20}\,\mathrm{W\,cm^{-2}}$, however as mentioned above, in case of the $0°$ target, the laser energy is about $20\,\%$ lower than for the other two targets. As the microstructures are tilted into the laser incident axis, the light can penetrate deeper into the troughs formed by the microstructures. Conversely, tilting the microstructures away from the laser axis shifts the interaction region towards the cone tips and increases the interaction surface. With this larger surface area, more hot electrons are expected to be accelerated, which is also indicated in the measured temperatures with an increase from

31 eV to 42 eV. The same observation is also made with respect to the total photon numbers recorded for the different target types (see section 6.2.2).

In addition to the previously discussed target types, FLTs and MLTs with a limited Cu volume on the back side were studied as well. The measured bulk electron temperatures are displayed in figure 6.21 together with the corresponding target type, which has a full surface Cu back side layer. For both target type groups, the bulk electron temperature is much lower for the small Cu volumes. One explanation for this observation could be a strong deflection of the hot electrons at the Si-Cu interface, as suggested by the work of Gremillet *et al.* [GBA02]. This could also reduce the flux of hot electrons that reach the small volumes. Another reason might be that the laser focus was not centrally between the two 150 µm spaced dots, such that only strongly scattered hot electrons could interact with the small Cu volumes, as discussed in section 6.2.4. This would lead to a lower flux of electrons. For the two MLTs with dots, the bulk electron temperature appears to scale with the intensity as expected.

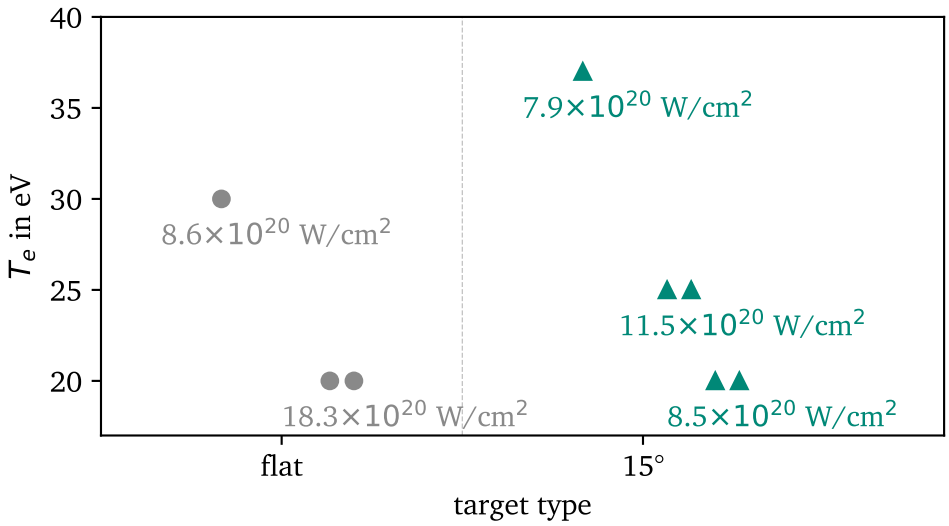

Figure 6.21: Bulk electron temperatures for limited Cu volume targets together with full layered targets. The temperature is much lower for the dot targets, as is the CE (see figure 6.11). For the two measurements of the dot MLTs, the temperature appears to scale with the intensity.

Besides the influence of the microstructures and their alignment with respect to the laser axis, the ASE contrast of the laser was varied during the experiment as well. In figure 6.22, the measured bulk electron temperatures are displayed over this contrast for three different target types. For the high contrast, the values correspond to the above discussed bulk electron temperatures for the FLT and the 0° and 15° MLTs. In contrast to the clear rise in temperature with microstructure tilt, for the lower ASE contrasts a different behaviour is observed. The targets are stronger irradiated before the main pulse arrives as the ASE level increases. This leads to a more developed pre-plasma that changes the absorption behaviour of the laser. The lower temperature measured for all target types at the low and medium contrast suggest that less hot electrons are produced during the interaction, resulting in less collisions. From this follows that even at a medium contrast of 3.5×10^{10}, the microstructures do not provide an additional benefit and a high contrast is necessary when using microstructured front surfaces. A similar observation is made when investigating the total number of photons emitted at different contrasts (see section 6.2.2).

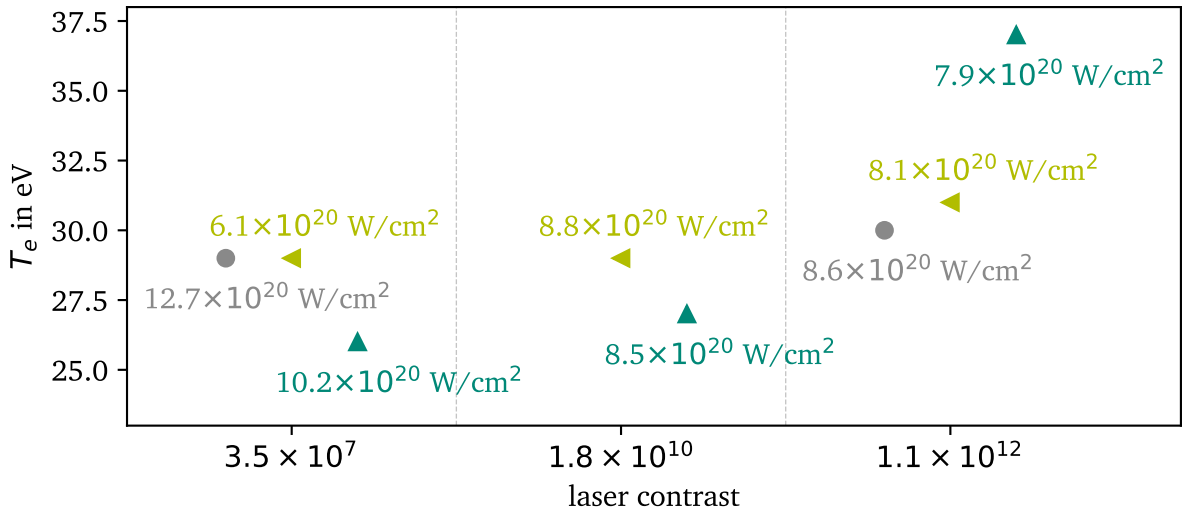

Figure 6.22: Bulk electron temperature over ASE contrast for three target types. The low and medium ASE contrasts lead to a slightly lower temperature, as is consistent with the findings for the CE (see section 6.2.3). Only the temperature for the $15°$ MLTs appears to be smaller. This leads to the conclusion that for the unaligned microstructures, the large pre-plasma formation results in a lower hot electron flux, which is partly compensated by a probable larger source size for the CE.

Overall, the analysis of the $K\alpha$ doublet with the SCFLY code has shown that the Cu back side layer was mostly heated to 20 - $45\,\mathrm{eV}$, with some further heating up to $200\,\mathrm{eV}$ for small portions of the emitting volume. In particular, the MLTs showed a higher bulk electron temperature when compared to the FLTs, indicating a higher number of collisions that not only heat the bulk electrons but also lead to $K\alpha$ emission by means of K-shell ionisation, leading to the observed higher CEs.

7 Conclusion and Outlook

The goal of this thesis was the development of an efficient $K\alpha$ source for future backlighting and scattering experiments. In this work, this goal was achieved with a novel layered design, that was inspired by tracer layer targets. The microstructuring of the target front side was used to offset the loss of efficiency due to the de-coupling of hot electron generation and X-ray emission. For the emission layer, Cu was chosen as it is well studied and at the verge between efficient $K\alpha$ and Heα sources. To the knowledge of the author no layered target concept was previously used as a primary backlighter source but always only as a diagnostic tool of the target itself. The key aspects, that were studied for this target design include: the presence of thermal line emission, the CE into $K\alpha$ radiation in comparison to commonly used flat foil targets and the resulting $K\alpha$ source size. With respect to other laser systems, the influence of the ASE level on the CE and source size was investigated as well.

The behaviour of the MLTs was studied during an experimental campaign at the PHELIX laser. Four crystal spectrometers measured the X-ray radiation from the back side of the targets. For all layered targets, the effective suppression of thermal line emission was demonstrated, independent of microstructure tilt towards the incoming laser beam or ASE level. For the FLTs, the expected decrease of CE is observed in comparison to a pure Cu foil target. The effectiveness of the front surface microstructures was demonstrated. An increase of two to three times higher CEs was shown when comparing MLTs to FLTs. The measured CE of 1×10^{-5} to 2×10^{-5} for the MLTs put the targets into the regime of possible applications for scattering experiments, such as collective X-ray Thomson scattering (XRTS) [GR09].

The tilt of the microstructures has been shown to influence the source size which was found to be between 140 ± 10 - $190 \pm 10\,\mu\mathrm{m}$ for the MLTs. The sizes are much larger when compared to the laser focal spot ($(6.4 \pm 1.2)\,\mu\mathrm{m}$) and to source sizes given in literature (50 - $90\,\mu\mathrm{m}$). A limitation of the source size to $100\,\mu\mathrm{m}$ was demonstrated with modified dot targets. These dot targets highlighted another unique feature of the layered targets, spatially separate sources generated with one target.

The variation of the ASE contrast showed a clear decrease in target efficiency for higher ASE levels. Even at a medium contrast of 1.8×10^{10}, a value that is common for many kJ laser systems [DNH14; Dor+15b; Din+21], no advantage of the MLTs over the FLTs was observed. Therefore, the ASE level has to be considered when planning future experiments using these microstructures.

A study of the $K\alpha$ doublet, supported by atomic radiative simulations, resulted in a bulk electron temperature of 31 - $42\,\mathrm{eV}$. The temperature measurements were consistent with the observed CE, indicating an increase in collisions, that is a larger number of hot electrons, with microstructure tilt.

Within the scope of this thesis, a novel target design was successfully developed. The thermal isolation of the emission layer was demonstrated, evidenced by an effective suppression of thermal line emission. This results in a clean spectrum for scattering applications. A significant boost of X-ray emission was achieved through the use of front side modifications in comparison to FLTs. The MLTs retain a sufficiently high $K\alpha$ CEs in comparison to conventional targets. The developed concept of MLTs offers new and unique

opportunities. One of these is the generation of spatially separate sources with one laser target interaction, which was successfully demonstrated. Furthermore can the source size be directly influenced upon target manufacturing, preventing the need of complex target shapes traditionally used to define a point-like source. These exciting results of the proof-of-principle experiment motivate further investigation into the combination of microstructured surfaces with a secondary layer for X-ray emission.

7.1 Outlook

Possible directions of future research with MLTs are discussed in this section. The start of future research should be aimed at improving the limited statistic of the presented data. For each combination of target and laser parameter, at most two independent measurements were possible. The promising results of this initial investigation into MLTs as indirectly driven $K\alpha$ backlighters should demonstrate the need for a more comprehensive study. Included in this investigation can be variations of the microstructure sizes as well as layer thicknesses, that could optimise the photon yield. Second to this is the high intensity of $> 10^{20}\,\mathrm{W\,cm^{-2}}$, that was used in this thesis. For simple foil targets, no additional improvement of the $K\alpha$ CE with increasing intensity beyond $10^{18}\,\mathrm{W\,cm^{-2}}$ has been observed. Additionally, the tight focus of the laser limited the interaction to at most one cone-like microstructure or the valley between. Future experiments should therefore focus on larger focal spot sizes to benefit from the homogeneous distribution of microstructures. Keeping the other laser parameters the same, a focal spot of $60\,\mu\mathrm{m}$ FWHM should be achievable. A lower intensity of about $10^{18}\,\mathrm{W\,cm^{-2}}$ will also relax the requirement of the ASE contrast.

Future experiments should be supported with particle-in-cell (PIC) simulations for a better understanding of the electron distribution that propagates through the back side layer. This could give insight into possible electron beam disruptions at the layer interface. Another step towards a better understanding of the emission behaviour would be the combination of the PIC simulated hot electron distribution with atomic radiative simulations. Initial studies with this combination of simulations are currently pursued for other targets, leading to insights such as a temporally resolved emission spectrum. Experimentally, the duration of the X-ray emission could be measured with an X-ray streak camera to obtain a more thorough survey of the target characteristics.

So far, only experiments with a Cu back side layer have been conducted. One advantage of the layered target design is that the same microstructure front side can be used with other back side materials. A switch to higher Z materials could prove useful for two reasons. The energy of the $K\alpha$ would be increased, which would allow the probing of denser material. Furthermore the fluorescence yield increases with Z, which could boost the resulting CE.

In addition to the use of other back side materials, the spatial limitation of the emitting material on the back side should be further explored. The focus of the investigated dot targets in this thesis was the demonstration of source size limiting and especially the spatial separation of two sources from one laser target interaction. In particular, the latter is most likely the cause of the much lower CE of these targets. Therefore, experiments that align the focal spot centrally with respect to the emitting volume should be done to measure the CE in dependence of material volume. The lateral dimensions of the deposited material could also be further reduced to provide small X-ray sources for high resolution applications.

Finally, the combination of limited material deposition with multiple materials proposes an interesting and unique opportunity. New experimental schemes could be explored that probe for example a shock-compressed or isochorically heated volume with multiple distinct wavelengths at the same time.

Acknowledgements

Ohne die Unterstützung vieler Menschen wäre diese Arbeit nicht mögliche gewesen. An dieser Stelle möchte ich mich dafür bedanken.

Zunächst gilt mein Dank **Prof. Dr. Markus Roth**, der mich über weite Strecken meiner wissenschaftlichen Ausbildung begleitet hat. Markus, Du hast mir die Arbeit in einem wahnsinnig spannenden Feld ermöglicht, und das noch dazu in einer großartigen Gruppe. Ich habe viel gelernt von Dir, von der Bachelorarbeit bis zur Promotion. Danke für Dein Vertrauen!

Außerdem möchte ich mich bei **Dr. Gabriel Schaumann** für die ausdauernde Unterstützung im Targetlabor bedanken. Dein Wissensschatz über Targets ist schier unendlich, Gabriel, und es ist jedes Mal spannend Dir zuzuhören. Danke für Deine Unterstützung bei Haupt- und Nebenprojekten.

Ein großer Dank gilt zudem **Dr. Tina Ebert** und **Dr. Markus Hesse**. Ihr seid die besten Kollegen der Welt und die Arbeit mit Euch hat super viel Spaß gemacht!
Tina, die morgendlichen Gespräche haben nicht nur die Motivation hochgehalten sondern haben auch immer wieder neue Ideen hervorgebracht - vielen Dank! Ohne Dich hätte ich wohl auch keine Targets gehabt.
Markus, auf Dich ist immer Verlass! Danke für deine Unterstützung bei Strahlzeiten, Laborarbeiten und so vielem mehr.

Furthermore, I would like to thank **Dr. Katja Falk**, **Dr. Michal Šmíd** and **Xiayun Pan** for all the support during my experiment and thereafter. I thank you for the many constructive discussions during the analysis and the simulations you provided.

An dieser Stelle möchte ich mich auch bei dem gesamten **PHELIX Team** für eine unglaublich gute Strahlzeit bedanken. Ihr habt euch richtig reingehängt und aus der kurzen Zeit viele Schüsse für mich herausgeholt! Mein Dank gilt auch **Dr. Torsten Abel** für die Unterstützung im Targetbau sowie **Dr. Alexandra Tebartz**, **Dr. Johannes Hornung**, **Christoph Bläser** und **Daniel Hartnagel** für den Support während der Strahlzeit!

Ich möchte mich auch bei **Dr. Alex Ortner** und **Dr. Jan Helfrich** bedanken, die mich auf dem Weg zur Promotion begleitet und motiviert haben. Ihr wart tolle Betreuer und habt mich überzeugt, das Projekt „Promotion“ bei Markus zu wagen.

My thank also goes to **Dr. Christian Stoeckl** for the opportunity to join experiments at the OMEGA EP facility.

Ohne eine großartige Arbeitsgruppe macht die Arbeit nur halb so viel Spaß - zum Glück seid ihr großartig! Danke an die ganze **AG Roth** für die tollen Jahren!

Vor der Promotion kam das Studium, und das wäre ohne **Laura**, **Sabine**, **Barbara**, **Mona**, **Janika** und **Victor** einfach nicht dasselbe gewesen. Danke an Euch für die Urlaube, Serien- und Dokuabende, für nächtliche Wanderungen und sonstige Abenteuer - an der Uni und abseits davon!

Meiner Tante **Andrea** möchte ich für die Unterstützung während meiner gesamten Ausbildungszeit danken. Du hast mich immer daran erinnert, dass Arbeit nicht alles ist und man seine freie Zeit mit schönen Dingen füllen soll. Dafür danke ich Dir!

Ein besonderer Dank gilt auch meinen Eltern **Elke** und **Jörg**. Ihr habt mir das Vertrauen mit auf den Weg gegeben, dass ich alles schaffen kann. Ihr habt mich fliegen lassen und mich immer unterstützt! Danke, dass ich immer zu Euch kommen kann!

Ohne Dich wäre diese Arbeit wohl nie fertig geworden. Danke **Oxana**, dass Du mich stützt, aufbaust und wieder auf den richtigen Weg bringst, dass Du mich ermunterst, Abenteuer zu erleben und immer etwas Neues auszuprobieren und dass Du immer da bist, wenn man Dich braucht.

Bibliography

[Alf39] H. Alfvén, “On the motion of cosmic rays in interstellar space”, Phys. Rev. **55**, 425 (1939).

[Ame95] Y. Amemiya, “Imaging Plates for Use with Synchrotron Radiation”, Journal of Synchrotron Radiation **2**, 13 (1995).

[Bae+15] S.-J. Baek, A. Park, Y.-J. Ahn, and J. Choo, “Baseline correction using asymmetrically reweighted penalized least squares smoothing”, The Analyst **140**, 250 (2015).

[Bag+10] V. Bagnoud, B. Aurand, A. Blazevic, S. Borneis, C. Bruske, B. Ecker, U. Eisenbarth, J. Fils, A. Frank, E. Gaul, S. Goette, C. Haefner, T. Hahn, K. Harres, H.-M. Heuck, D. Hochhaus, D. H. H. Hoffmann, D. Javorková, H.-J. Kluge, T. Kuehl, S. Kunzer, M. Kreutz, T. Merz-Mantwill, P. Neumayer, E. Onkels, D. Reemts, O. Rosmej, M. Roth, T. Stoehlker, A. Tauschwitz, B. Zielbauer, D. Zimmer, and K. Witte, “Commissioning and early experiments of the PHELIX facility”, Applied Physics B **100**, 137 (2010).

[Bar+89] A. Bar-Shalom, J. Oreg, W. H. Goldstein, D. Shvarts, and A. Zigler, “Super-transition-arrays: A model for the spectral analysis of hot, dense plasma”, Physical Review A **40**, 3183 (1989).

[Bat77] J. Bateman, “The detection of hard X-rays (10–140 keV) by channel plate electron multipliers”, Nuclear Instruments and Methods **144**, 537 (1977).

[BBK88] J. Bauche, C. Bauche-Arnoult, and M. Klapisch, “Unresolved transition arrays”, Physica Scripta **37**, 659 (1988).

[BMS95] D. Bauer, P. Mulser, and W. .-. Steeb, “Relativistic ponderomotive force, uphill acceleration, and transition to chaos”, Phys. Rev. Lett. **75**, 4622 (1995).

[Beg+97] F. N. Beg, A. R. Bell, A. E. Dangor, C. N. Danson, A. P. Fews, M. E. Glinsky, B. A. Hammel, P. Lee, P. A. Norreys, and M. Tatarakis, “A study of picosecond laser–solid interactions up to 10 19 W cm -2”, Physics of Plasmas **4**, 447 (1997).

[Ber+] M. J. Berger, J. Coursey, M. Zucker, and J. Chang, *ESTAR*, `https://www.nist.gov/pml/stopping-power-range-tables-electrons-protons-and-helium-ions` (visited on 08/03/2021).

[BH87] M. Berger and J. Hubbell, *XCOM: Photon cross sections on a personal computer*, tech. rep. 3597 (Oak Ridge Operations, Oak Ridge, TN, 1987), p. 26.

[BU64] L. C. F. Blackman and F. R. S. Ubbelohde, “Stress recrystallization of pyrolytic graphite”, Proceedings of the Royal Society of London. Series A. Mathematical and Physical Sciences **280**, 153 (1964).

[Bla+17] M. Blanco, M. T. Flores-Arias, C. Ruiz, and M. Vranic, “Table-top laser-based proton acceleration in nanostructured targets”, New Journal of Physics **19**, 033004 (2017).

[BEH05] H. F. M. Boelens, P. H. C. Eilers, and T. Hankemeier, “Sign Constraints Improve the Detection of Differences between Complex Spectral Data Sets: LC-IR As an Example”, Analytical Chemistry **77**, 7998 (2005).

[Bon+13a] T. Bonnet, M. Comet, D. Denis-Petit, F. Gobet, F. Hannachi, M. Tarisien, M. Versteegen, and M. M. Aleonard, “Response functions of Fuji imaging plates to monoenergetic protons in the energy range 0.6–3.2 MeV”, Review of Scientific Instruments **84**, 013508 (2013).

[Bon+13b] T. Bonnet, M. Comet, D. Denis-Petit, F. Gobet, F. Hannachi, M. Tarisien, M. Versteegen, and M. M. Aléonard, “Response functions of imaging plates to photons, electrons and 4 He particles”, Review of Scientific Instruments **84**, 103510 (2013).

[BKN19] B. Borm, D. Khaghani, and P. Neumayer, “Properties of laser-driven hard x-ray sources over a wide range of laser intensities”, Physics of Plasmas **26**, 023109 (2019).

[Bou+20] V. Bouffetier, L. Ceurvorst, M. P. Valdivia, F. Dorchies, S. Hulin, T. Goudal, D. Stutman, and A. Casner, “Proof-of-concept Talbot–Lau x-ray interferometry with a high-intensity, high-repetition-rate, laser-driven K-alpha source”, Applied Optics **59**, 8380 (2020).

[Bou+15] G. Boutoux, N. Rabhi, D. Batani, A. Binet, J.-E. Ducret, K. Jakubowska, J.-P. Nègre, C. Reverdin, and I. Thfoin, “Study of imaging plate detector sensitivity to 5-18 MeV electrons”, Review of Scientific Instruments **86**, 113304 (2015).

[Boy20] R. W. Boyd, in *Nonlinear optics (fourth edition)*, edited by R. W. Boyd, Fourth Edition (Academic Press, 2020), pp. 523–539.

[Bra+92] D. K. Bradley, P. M. Bell, J. D. Kilkenny, R. Hanks, O. Landen, P. A. Jaanimagi, P. W. McKenty, and C. P. Verdon, “High-speed gated x-ray imaging for ICF target experiments (invited)”, Review of Scientific Instruments **63**, 4813 (1992).

[Bra+95] D. K. Bradley, P. M. Bell, O. L. Landen, J. D. Kilkenny, and J. Oertel, “Development and characterization of a pair of 30-40 ps x-ray framing cameras”, Review of Scientific Instruments **66**, 716 (1995).

[Bru87] F. Brunel, “Not-so-resonant, resonant absorption”, Physical Review Letters **59**, 52 (1987).

[CM77] P. J. Catto and R. M. More, “Sheath inverse bremsstrahlung in laser produced plasmas”, The Physics of Fluids **20**, 704 (1977).

[Che16] F. Chen, *Introduction to Plasma Physics and Controlled Fusion*, 3rd ed. (Springer, Cham, Heidelberg New York Dordrecht London, 2016).

[Che+07] H. Chen, R. Shepherd, H. K. Chung, A. Kemp, S. B. Hansen, S. C. Wilks, Y. Ping, K. Widmann, K. B. Fournier, G. Dyer, A. Faenov, T. Pikuz, and P. Beiersdorfer, “Fast-electron-relaxation measurement for laser-solid interaction at relativistic laser intensities”, Physical Review E - Statistical, Nonlinear, and Soft Matter Physics **76**, 056402 (2007).

[Che+79] M. H. Chen, E. Laiman, B. Crasemann, M. Aoyagi, and H. Mark, “Relativistic L-shell Auger and Coster-Kronig rates and fluorescence yields”, Phys. Rev. A **19**, 2253 (1979).

[Che+09] S. N. Chen, P. K. Patel, H.-K. Chung, A. J. Kemp, S. Le Pape, B. R. Maddox, S. C. Wilks, R. B. Stephens, and F. N. Beg, “X-ray spectroscopy of buried layer foils irradiated at laser intensities in excess of 1020 W/cm2”, **16**, 062701 (2009).

[Cho+19] L. Chopineau, A. Leblanc, G. Blaclard, A. Denoeud, M. Thévenet, J.-L. Vay, G. Bonnaud, P. Martin, H. Vincenti, and F. Quéré, “Identification of Coupling Mechanisms between Ultraintense Laser Light and Dense Plasmas”, Physical Review X **9**, 011050 (2019).

[Chu+05] H.-K. Chung, M. Chen, W. Morgan, Y. Ralchenko, and R. Lee, "Flychk: generalized population kinetics and spectral model for rapid spectroscopic analysis for all elements", High Energy Density Physics **1**, 3 (2005).

[Chu+17] H.-K. Chung, B. I. Cho, O. Ciricosta, S. M. Vinko, J. S. Wark, and R. W. Lee, "Atomic processes modeling of X-ray free electron laser produced plasmas using SCFLY code", in Aip conference proceedings, Vol. 1811 (2017), p. 020001.

[Chu+08] H.-K. Chung, R. W. Lee, M. H. Chen, and Y. Ralchenko, *FLYCHK Manual* (2008), `https://nlte.nist.gov/FLY/Doc/Manual_FLYCHK_Nov08.pdf` (visited on 01/31/2022).

[Cro14] B. Crowley, "Continuum lowering – a new perspective", High Energy Density Physics **13**, 84 (2014).

[Cul+14] O. Culfa, G. J. Tallents, E. Wagenaars, C. P. Ridgers, R. J. Dance, A. K. Rossall, R. J. Gray, P. McKenna, C. D. R. Brown, S. F. James, D. J. Hoarty, N. Booth, A. P. L. Robinson, K. L. Lancaster, S. A. Pikuz, A. Y. Faenov, T. Kampfer, K. S. Schulze, I. Uschmann, and N. C. Woolsey, "Hot electron production in laser solid interactions with a controlled pre-pulse", Physics of Plasmas **21**, 043106 (2014).

[DNH14] C. Danson, D. Neely, and D. Hillier, "Pulse fidelity in ultra-high-power (petawatt class) laser systems", High Power Laser Science and Engineering **2**, e34 (2014).

[DAV06] J. DAVIES, "The alfvén limit revisited and its relevance to laser-plasma interactions", Laser and Particle Beams **24**, 299 (2006).

[Dem+11] H. Demers, N. Poirier-Demers, A. R. Couture, D. Joly, M. Guilmain, N. de Jonge, and D. Drouin, "Three-dimensional electron microscopy simulation with the casino monte carlo software", Scanning **33**, 135 (2011).

[Dem16] W. Demtröder, *Experimentalphysik 3*, 5th ed. (Springer Berlin Heidelberg, Berlin, Heidelberg, 2016).

[Din+21] F. Ding, X. Ouyang, X. Zhang, Y. Jiang, K. Hou, X. Jiang, H. Tao, B. Zhu, D. Liu, J. Zhu, and J. Zhu, "Universal nanosecond range pulse contrast measurement for a kj-class petawatt laser", Applied Optics **60**, 10016 (2021).

[Don+04] C. L. Dong, C. Persson, L. Vayssieres, A. Augustsson, T. Schmitt, M. Mattesini, R. Ahuja, C. L. Chang, and J.-H. Guo, "Electronic structure of nanostructured zno from x-ray absorption and emission spectroscopy and the local density approximation", Phys. Rev. B **70**, 195325 (2004).

[Dor+15a] F. Dorchies, F. Festa, V. Recoules, O. Peyrusse, A. Benuzzi-Mounaix, E. Brambrink, A. Levy, A. Ravasio, M. Koenig, T. Hall, and S. Mazevet, "X-ray absorption K edge as a diagnostic of the electronic temperature in warm dense aluminum", Physical Review B - Condensed Matter and Materials Physics **92**, 085117 (2015).

[Dor+15b] C. Dorrer, A. Consentino, D. Irwin, J. Qiao, and J. Zuegel, "Opcpa front end and contrast optimization for the omega ep kilojoule, picosecond laser", Journal of Optics **17**, 094007 (2015).

[Dra18] R. P. Drake, *High-Energy-Density Physics*, Graduate Texts in Physics (Springer International Publishing, Cham, 2018).

[Ebe+21] T. Ebert, R. Heber, T. Abel, J. Bieker, G. Schaumann, and M. Roth, "Targets with cone-shaped microstructures from various materials for enhanced high-intensity laser-matter interaction", High Power Laser Science and Engineering **9**, e24 (2021).

[Ebe+17] T. Ebert, N. W. Neumann, T. Abel, G. Schaumann, and M. Roth, “Laser-induced microstructures on silicon for laser-driven acceleration experiments”, High Power Laser Science and Engineering **5**, e13 (2017).

[Ebe+20] T. Ebert, N. W. Neumann, L. N. K. Döhl, J. Jarrett, C. Baird, R. Heathcote, M. Hesse, A. Hughes, P. McKenna, D. Neely, D. Rusby, G. Schaumann, C. Spindloe, A. Tebartz, N. Woolsey, and M. Roth, “Enhanced brightness of a laser-driven x-ray and particle source by microstructured surfaces of silicon targets”, Physics of Plasmas **27**, 043106 (2020).

[ESK95] E. Esarey, P. Sprangle, and J. Krall, “Laser acceleration of electrons in vacuum”, Physical Review E **52**, 5443 (1995).

[For+96] V. Fortov, G. Kanel, A. Utkin, O. Vorobiev, G. Kessler, H. Karow, K. Baumung, B. Goel, and V. Light, “Intense shock waves in hot dense matter generated by high-power light ion beams”, AIP Conference Proceedings **369**, 1060 (1996).

[FK16] S. Fourmaux and J. C. Kieffer, “Laser-based K α X-ray emission characterization using a high contrast ratio and high-power laser system”, Applied Physics B: Lasers and Optics **122**, 1 (2016).

[Fuj+03] S. Fujioka, H. Shiraga, M. Nishikino, K. Shigemori, A. Sunahara, M. Nakai, H. Azechi, K. Nishihara, and T. Yamanaka, “First observation of density profile in directly laser-driven polystyrene targets for ablative Rayleigh-Taylor instability research”, Physics of Plasmas **10**, 4784 (2003).

[Gam+11] E. J. Gamboa, D. S. Montgomery, I. M. Hall, and R. P. Drake, “Imaging X-ray crystal spectrometer for laser-produced plasmas”, Journal of Instrumentation **6**, P04004 (2011).

[Gib05] P. Gibbon, *Short pulse laser interactions with matter* (Imperial College Press, London, 2005).

[Gig14] M. A. Gigosos, “Stark broadening models for plasma diagnostics”, Journal of Physics D: Applied Physics **47**, 343001 (2014).

[Gir16] F. Girard, “Review of laser produced multi-keV X-ray sources from metallic foils, cylinders with liner, and low density aerogels”, Physics of Plasmas **23**, 040501 (2016).

[GR09] S. H. Glenzer and R. Redmer, “X-ray Thomson scattering in high energy density plasmas”, Reviews of Modern Physics **81**, 1625 (2009).

[GBA02] L. Gremillet, G. Bonnaud, and F. Amiranoff, “Filamented transport of laser-generated relativistic electrons penetrating a solid target”, Physics of Plasmas **9**, 941 (2002).

[Hab+16] H. Habara, S. Honda, M. Katayama, H. Sakagami, K. Nagai, and K. A. Tanaka, “Efficient energy absorption of intense ps-laser pulse into nanowire target”, Physics of Plasmas **23**, 063105 (2016).

[Har19] D. Hartnagel, “Entwicklung eines Röntgenspektrometers für Laser-Plasma-Experimente”, MA thesis (Technische Universität Darmstadt, 2019).

[Hen+84a] B. L. Henke, F. G. Fujiwara, M. A. Tester, C. H. Dittmore, and M. A. Palmer, “Low-energy x-ray response of photographic films. II. Experimental characterization”, J. Opt. Soc. Am. B **1**, 828 (1984).

[HGD93] B. L. Henke, E. M. Gullikson, and J. C. Davis, “X-ray interactions: photoabsorption, scattering, transmission, and reflection at E=50-30000 eV, Z=1-92”, Atomic Data and Nuclear Data Tables **52**, 181 (1993).

[Hen+84b] B. L. Henke, S. L. Kwok, J. Y. Uejio, H. T. Yamada, and G. C. Young, “Low-energy x-ray response of photographic films. I. Mathematical models”, J. Opt. Soc. Am. B **1**, 818 (1984).

[Her+98] T.-H. Her, R. J. Finlay, C. Wu, S. Deliwala, and E. Mazur, “Microstructuring of silicon with femtosecond laser pulses”, Applied Physics Letters **73**, 1673 (1998).

[Hol+17] W. M. Holden, O. R. Hoidn, A. S. Ditter, G. T. Seidler, J. Kas, J. L. Stein, B. M. Cossairt, S. A. Kozimor, J. Guo, Y. Ye, M. A. Marcus, and S. Fakra, “A compact dispersive refocusing Rowland circle X-ray emission spectrometer for laboratory, synchrotron, and XFEL applications”, Review of Scientific Instruments **88**, 073904 (2017).

[HWF98] G. Hölzer, O. Wehrhan, and E. Förster, “Characterization of Flat and Bent Crystals for X-ray Spectroscopy and Imaging”, Crystal Research and Technology **33**, 555 (1998).

[Hor+20] J. Hornung, Y. Zobus, P. Boller, C. Brabetz, U. Eisenbarth, T. Kühl, Z. Major, J. B. Ohland, M. Zepf, B. Zielbauer, and V. Bagnoud, “Enhancement of the laser-driven proton source at PHELIX”, High Power Laser Science and Engineering **8**, 1 (2020).

[How+06] J. Howe, D. M. Chambers, C. Courtois, E. Förster, C. D. Gregory, I. M. Hall, O. Renner, I. Uschmann, and N. C. Woolsey, “Comparison of film detectors, charged-coupled devices, and imaging plates in x-ray spectroscopy of hot dense plasma”, Review of Scientific Instruments **77**, 036105 (2006).

[Hua+76] K. N. Huang, M. Aoyagi, H. Mark, M. H. Chen, and B. Crasemann, “Neutral-atom electron binding energies from relaxed-orbital relativistic Hartree-Fock-Slater calculations for Z between 2 and 106”, in Atomic data and nuclear data tables, Vol. 18 (1976), pp. 243–291.

[IE00] A. Ichihara and J. Eichler, “Cross sections for radiative recombination and the photoelectric effect in the K, L, and M shells of one-electron systems with $1 \leq z \leq 112$ calculated within an exact relativistic description”, Atomic Data and Nuclear Data Tables **74**, 1 (2000).

[Izu+06] N. Izumi, R. Snavely, G. Gregori, J. A. Koch, H.-S. Park, and B. A. Remington, “Application of imaging plates to x-ray imaging and spectroscopy in laser plasma experiments (invited)”, Review of Scientific Instruments **77**, 10E325 (2006).

[Jar+14] L. C. Jarrott, A. J. Kemp, L. Divol, D. Mariscal, B. Westover, C. McGuffey, F. N. Beg, M. Suggit, C. Chen, D. Hey, B. Maddox, J. Hawreliak, H. S. Park, B. Remington, M. S. Wei, and A. Macphee, “Kα and bremsstrahlung x-ray radiation backlighter sources from short pulse laser driven silver targets as a function of laser pre-pulse energy”, Physics of Plasmas **21**, 031211 (2014).

[Jia+14] S. Jiang, A. G. Krygier, D. W. Schumacher, K. U. Akli, and R. R. Freeman, “Effects of front-surface target structures on properties of relativistic laser-plasma electrons”, Physical Review E - Statistical, Nonlinear, and Soft Matter Physics **89**, 1 (2014).

[Joh31] H. H. Johann, “Die Erzeugung lichtstarker Röntgenspektren mit Hilfe von Konkavkristallen”, Zeitschrift für Physik **69**, 185 (1931).

[Joh33] T. Johansson, “Über ein neuartiges, genau fokussierendes Röntgenspektrometer - Erste Mitteilung”, Zeitschrift für Physik **82**, 507 (1933).

[Kli+11] O. Klimo, J. Psikal, J. Limpouch, J. Proska, F. Novotny, T. Ceccotti, V. Floquet, and S. Kawata, “Short pulse laser interaction with micro-structured targets: Simulations of laser absorption and ion acceleration”, New Journal of Physics **13**, 053028 (2011).

[Kol03] R. Kolb, “Synthese und Eigenschaften keramischer Neutronenbildplatten auf der Basis von BaFBr:Eu2+ und Gd-Verbindungen”, PhD thesis (Technische Universität Darmstadt, 2003).

[KO79] M. O. Krause and J. H. Oliver, “Natural width of atomic K and L level Kα X-ray lines and several KLL Auger lines.”, J. Phys. Chem. Ref. Data **8**, 329 (1979).

[KE85] W. L. Kruer and K. Estabrook, "J×B heating by very intense laser light", Physics of Fluids **28**, 430 (1985).

[Kul+00] G. Kulcsár, D. AlMawlawi, F. W. Budnik, P. R. Herman, M. Moskovits, L. Zhao, and R. S. Marjoribanks, "Intense Picosecond X-Ray Pulses from Laser Plasmas by Use of Nanostructured "Velvet" Targets", Physical Review Letters **84**, 5149 (2000).

[Le +10] S. Le Pape, P. Neumayer, C. Fortmann, T. Döppner, P. Davis, A. Kritcher, O. Landen, and S. Glenzer, "X-ray radiography and scattering diagnosis of dense shock-compressed matter", Physics of Plasmas **17**, 056309 (2010).

[Leg+09] H. Legall, H. Stiel, M. Schnürer, M. Pagels, B. Kanngieer, M. Müller, B. Beckhoff, I. Grigorieva, A. Antonov, V. Arkadiev, and A. Bjeoumikhov, "An efficient X-ray spectrometer based on thin mosaic crystal films and its application in various fields of X-ray spectroscopy", Journal of Applied Crystallography **42**, 572 (2009).

[Llo+14] X. Llovet, C. J. Powell, F. Salvat, and A. Jablonski, "Cross Sections for Inner-Shell Ionization by Electron Impact", Journal of Physical and Chemical Reference Data **43**, 013102 (2014).

[Mac+01] A. Macchi, F. Cornolti, F. Pegoraro, T. V. Liseikina, H. Ruhl, and V. A. Vshivkov, "Surface oscillations in overdense plasmas irradiated by ultrashort laser pulses", Phys. Rev. Lett. **87**, 205004 (2001).

[Mac93] J. J. MacFarlane, *Collisional-Radiative Equilibrium (CRE) Model for the CONRAD Radiation-Hydrodynamics Code*, December (1993), UWFDM–937, `http://fti.neep.wisc.edu/pdf/fdm937.pdf`.

[Mac58] G. Mack, "Präzisionsmessung der Gitterkonstante an Germanium-Einkristallen nach Kossel und van Bergen", Zeitschrift für Physik **152**, 19 (1958).

[Mad+11] B. R. Maddox, H. S. Park, B. A. Remington, N. Izumi, S. Chen, C. Chen, G. Kimminau, Z. Ali, M. J. Haugh, and Q. Ma, "High-energy x-ray backlighter spectrum measurements using calibrated image plates", Review of Scientific Instruments **82**, 023111 (2011).

[MW06] W. Martin and W. Wiese, "Atomic spectroscopy", in *Springer handbook of atomic, molecular, and optical physics*, edited by G. Drake (Springer New York, New York, NY, 2006), pp. 175–198.

[McK+13] P. McKenna, D. Neely, R. Bingham, and D. A. Jaroszynski, *Laser-Plasma Interactions and Applications* (Springer International Publishing, Heidelberg, 2013).

[MBS08] A. L. Meadowcroft, C. D. Bentley, and E. N. Stott, "Evaluation of the sensitivity and fading characteristics of an image plate system for x-ray diagnostics", Review of Scientific Instruments **79**, 113102 (2008).

[Mor+14] A. Morace, L. Fedeli, D. Batani, S. Baton, F. N. Beg, S. Hulin, L. C. Jarrott, A. Margarit, M. Nakai, M. Nakatsutsumi, P. Nicolai, N. Piovella, M. S. Wei, X. Vaisseau, L. Volpe, and J. J. Santos, "Development of x-ray radiography for high energy density physics", Physics of Plasmas **21**, 102712 (2014).

[MB10] P. Mulser and D. Bauer, *High Power Laser-Matter Interaction* (Springer Berlin Heidelberg, Berlin, Heidelberg, 2010).

[MKF90] M. M. Murnane, H. C. Kapteyn, and R. W. Falcone, "X-ray streak camera with 2 ps response", Applied Physics Letters **56**, 1948 (1990).

[Neu+10] P. Neumayer, B. Aurand, M. Basko, B. Ecker, P. Gibbon, D. C. Hochhaus, A. Karmakar, E. Kazakov, T. Kühl, C. Labaune, O. Rosmej, A. Tauschwitz, B. Zielbauer, and D. Zimmer, "The role of hot electron refluxing in laser-generated K-alpha sources", Physics of Plasmas **17**, 103103 (2010).

[Nil+09] P. M. Nilson, W. Theobald, J. F. Myatt, C. Stoeckl, M. Storm, J. D. Zuegel, R. Betti, D. D. Meyerhofer, and T. C. Sangster, "Bulk heating of solid-density plasmas during high-intensity-laser plasma interactions", Physical Review E - Statistical, Nonlinear, and Soft Matter Physics **79**, 016406 (2009).

[Nil+08] P. M. Nilson, W. Theobald, J. Myatt, C. Stoeckl, M. Storm, O. V. Gotchev, J. D. Zuegel, R. Betti, D. D. Meyerhofer, and T. C. Sangster, "High-intensity laser-plasma interactions in the refluxing limit", Physics of Plasmas **15**, 056308 (2008).

[OY02] H. Ohuchi and A. Yamadera, "Dependence of fading patterns of photo-stimulated luminescence from imaging plates on radiation, energy, and image reader", Nuclear Instruments and Methods in Physics Research Section A: Accelerators, Spectrometers, Detectors and Associated Equipment **490**, 573 (2002).

[OYN00] H. Ohuchi, A. Yamadera, and T. Nakamura, "Functional equation for the fading correction of imaging plates", Nuclear Instruments and Methods in Physics Research, Section A: Accelerators, Spectrometers, Detectors and Associated Equipment **450**, 343 (2000).

[Par+06] H.-S. Park, D. M. Chambers, H.-K. Chung, R. J. Clarke, R. Eagleton, E. Giraldez, T. Goldsack, R. Heathcote, N. Izumi, M. H. Key, J. A. King, J. A. Koch, O. L. Landen, A. Nikroo, P. K. Patel, D. F. Price, B. A. Remington, H. F. Robey, R. A. Snavely, D. A. Steinman, R. B. Stephens, C. Stoeckl, M. Storm, M. Tabak, W. Theobald, R. P. J. Town, J. E. Wickersham, and B. B. Zhang, "High-energy Kα radiography using high-intensity, short-pulse lasers", Physics of Plasmas **13**, 056309 (2006).

[Pér+14] F. Pérez, J. R. Patterson, M. May, J. D. Colvin, M. M. Biener, A. Wittstock, S. O. Kucheyev, S. Charnvanichborikarn, J. H. Satcher, S. A. Gammon, J. F. Poco, S. Fujioka, Z. Zhang, K. Ishihara, N. Tanaka, T. Ikenouchi, H. Nishimura, and K. B. Fournier, "Bright x-ray sources from laser irradiation of foams with high concentration of Ti", Physics of Plasmas **21**, 023102 (2014).

[RR19] O. Renner and F. B. Rosmej, "Challenges of x-ray spectroscopy in investigations of matter under extreme conditions", Matter and Radiation at Extremes **4**, 024201 (2019).

[Rön95] C. W. Röntgen, *Über eine neue Art von Strahlen - Vorläufige Mittheilung*, 2nd ed. (Stahel'sche K. Hof- und Universitätsbuch- und Kunsthandlung, Würzburg, 1895).

[Rön96] C. W. Röntgen, *Über eine neue Art von Strahlen - Fortsetzung*, 1st ed. (Stahel'sche K. Hof- und Universitätsbuch- und Kunsthandlung, Würzburg, 1896).

[Rön97] C. W. Röntgen, *Weitere Beobachtungen über die Eigenschaften der X-Strahlen*, 1st ed. (Verl. d. Kgl. Akad. d. Wiss., Berlin, 1897).

[Sam+18] Z. Samsonova, S. Höfer, T. Kämpfer, I. Uschmann, R. Röder, L. Trefflich, O. Rosmej, E. Förster, C. Ronning, D. Kartashov, and C. Spielmann, "Hard X-ray Generation from ZnO Nanowire Targets in a Non-Relativistic Regime of Laser-Solid Interactions", Applied Sciences **8**, 1728 (2018).

[San+98] M. Sanchez del Rio, M. Gambaccini, G. Pareschi, A. Taibi, A. Tuffanelli, and A. K. Freund, "Focusing properties of mosaic crystals", in Crystal and multilayer optics, Vol. 3448 (1998), p. 246.

[Seg92] H. von Seggern, “X-ray imaging with photostimulable phosphors”, Nuclear Inst. and Methods in Physics Research, A **322**, 467 (1992).

[Sel20] I. Selyuzhenkov, “Status of the FAIR facility in darmstadt”, Journal of Physics: Conference Series **1685**, 012020 (2020).

[Šmí+19] M. Šmíd, O. Renner, A. Colaitis, V. T. Tikhonchuk, T. Schlegel, and F. B. Rosmej, “Characterization of suprathermal electrons inside a laser accelerated plasma via highly-resolved Kα-emission”, Nature Communications **10**, 1 (2019).

[ŠPF21] M. Šmíd, X. Pan, and K. Falk, “X-ray spectrometer simulation code with a detailed support of mosaic crystals”, Computer Physics Communications **9**, 107811 (2021).

[Sto+04] C. Stoeckl, W. Theobald, T. C. Sangster, M. H. Key, P. Patel, B. B. Zhang, R. Clarke, S. Karsch, and P. Norreys, “Operation of a single-photon–counting x-ray charge-coupled device camera spectrometer in a petawatt environment”, Review of Scientific Instruments **75**, 3705 (2004).

[SM85] D. Strickland and G. Mourou, “Compression of amplified chirped optical pulses”, Optics Communications **56**, 219 (1985).

[Tal+97] G. J. Tallents, J. Krishnan, L. Dwivedi, D. Neely, and I. C. E. Turcu, “Film calibration for soft x-ray wavelengths”, in Applications of x rays generated from lasers and other bright sources, Vol. 3157 (1997), p. 281.

[The+06] W. Theobald, K. Akli, R. Clarke, J. A. Delettrez, R. R. Freeman, S. Glenzer, J. Green, G. Gregori, R. Heathcote, N. Izumi, J. A. King, J. A. Koch, J. Kuba, K. Lancaster, A. J. MacKinnon, M. Key, C. Mileham, J. Myatt, D. Neely, P. A. Norreys, H.-S. Park, J. Pasley, P. Patel, S. P. Regan, H. Sawada, R. Shepherd, R. Snavely, R. B. Stephens, C. Stoeckl, M. Storm, B. Zhang, and T. C. Sangster, “Hot surface ionic line emission and cold K-inner shell emission from petawatt-laser-irradiated Cu foil targets”, Physics of Plasmas **13**, 043102 (2006).

[Tho+09] A. Thompson, I. Lindau, D. Attwood, Y. Liu, E. Gullikson, P. Pianetta, M. Howells, A. Robinson, K. Kim, J. Scofield, J. Kirz, J. Underwood, J. Kortright, G. Williams, and H. Winick, *X-Ray Data Booklet*, 3rd ed. (Lawrence Berkeley National Laboratory, Berkeley, 2009).

[Tom+11] R. Tommasini, S. P. Hatchett, D. S. Hey, C. Iglesias, N. Izumi, J. A. Koch, O. L. Landen, A. J. MacKinnon, C. Sorce, J. A. Delettrez, V. Y. Glebov, T. C. Sangster, and C. Stoeckl, “Development of compton radiography of inertial confinement fusion implosions”, Physics of Plasmas **18**, 056309 (2011).

[Tow+05] R. Town, C. Chen, L. Cottrill, M. Key, W. Kruer, A. Langdon, B. Lasinski, R. Snavely, C. Still, M. Tabak, D. Welch, and S. Wilks, “Simulations of electron transport for fast ignition using lsp”, Nuclear Instruments and Methods in Physics Research Section A: Accelerators, Spectrometers, Detectors and Associated Equipment **544**, 61 (2005).

[Ums03] D. Umstadter, “Relativistic laser plasma interactions”, Journal of Physics D: Applied Physics **36**, R151 (2003).

[Wag+14] F. Wagner, S. Bedacht, A. Ortner, M. Roth, A. Tauschwitz, B. Zielbauer, and V. Bagnoud, “Pre-plasma formation in experiments using petawatt lasers”, Optics Express **22**, 29505 (2014).

[WLC18] H. Wang, Z. Li, and Z. Chen, “High conversion efficiency and small spot size of Kα X-ray generated from nano-foam Cu targets irradiated by femtosecond laser pulses”, Applied Physics B **124**, 172 (2018).

[Wen+13] C. Weninger, M. Purvis, D. Ryan, R. A. London, J. D. Bozek, C. Bostedt, A. Graf, G. Brown, J. J. Rocca, and N. Rohringer, “Stimulated Electronic X-Ray Raman Scattering”, Physical Review Letters **111**, 233902 (2013).

[Wil+92] S. C. Wilks, W. L. Kruer, M. Tabak, and A. B. Langdon, “Absorption of ultra-intense laser pulses”, Phys. Rev. Lett. **69**, 1383 (1992).

[Yan+95] T.-Y. B. Yang, W. L. Kruer, R. M. More, and A. B. Langdon, “Absorption of laser light in overdense plasmas by sheath inverse bremsstrahlung”, Physics of Plasmas **2**, 3146 (1995).

[Ye +13] Y. T. Ye Tian, W. W. Wentao Wang, C. W. Cheng Wang, X. L. Xiaoming Lu, C. W. Cheng Wang, Y. L. Yuxin Leng, X. L. Xiaoyan Liang, J. L. Jiansheng Liu, R. L. Ruxin Li, and Z. X. Zhizhan Xu, “Experimental study of K-shell X-ray emission generated from nanowire target irradiated by relativistic laser pulses”, Chinese Optics Letters **11**, 033501 (2013).

[Yua+11] X. H. Yuan, D. C. Carroll, M. Coury, R. J. Gray, C. M. Brenner, X. X. Lin, Y. T. Li, M. N. Quinn, O. Tresca, B. Zielbauer, D. Neely, and P. McKenna, “Spatially resolved X-ray spectroscopy using a flat HOPG crystal”, Nuclear Instruments and Methods in Physics Research, Section A: Accelerators, Spectrometers, Detectors and Associated Equipment **653**, 145 (2011).

[ZF14] U. Zastrau and E. Förster, “Integrated reflectivity measurements of hydrogen phthalate crystals for high-resolution soft x-ray spectroscopy”, Journal of Instrumentation **9**, P09008 (2014).

[Zme+10] B. Zmerli, N. B. Nessib, M. S. Dimitrijević, and S. Sahal-Bréchot, “Stark broadening calculations of neutral copper spectral lines and temperature dependence”, Physica Scripta **82**, 055301 (2010).

Publications

W. Cayzac, A. Frank, A. Ortner, V. Bagnoud, M. M. Basko, S. Bedacht, C. Bläser, A. Blažević, S. Busold, O. Deppert, J. Ding, M. Ehret, P. Fiala, S. Frydrych, D. O. Gericke, L. Hallo, J. Helfrich, D. Jahn, E. Kjartansson, A. Knetsch, D. Kraus, G. Malka, N. W. Neumann, K. Pépitone, D. Pepler, **S. Sander**, G. Schaumann, T. Schlegel, N. Schroeter, D. Schumacher, M. Seibert, A. Tauschwitz, J. Vorberger, F. Wagner, S. Weih, Y. Zobus, and M. Roth, "Experimental Discrimination of Ion Stopping Models near the Bragg Peak in Highly Ionized Matter", Nature Communications **8**, 15693 (2017).

C. Stoeckl, M.J. Bonino, C. Mileham, S.P. Regan, W. Theobald, T. Ebert and **S. Sander**, "Optimization of a short-pulse-driven Si Heα soft x-ray backlighter", High Energy Density Physics **41**, 100973 (2021).

S. Sander, T. Ebert, D. Hartnagel, M. Hesse, X. Pan, G. Schaumann, M. Šmíd, K. Falk and M. Roth, "Microstructured layered targets for improved laser-induced x-ray backlighters", Physical Review E **104**, 065207 (2021).

Conferences

S. Sander,, J. Helfrich, D. Schumacher, G. Schaumann and M. Roth, "Two stage targets for hyper-velocity impact experiments", *Poster*, Target Fabrication Workshop 6 (2017), London, United Kingdom.

S. Sander, G. Schaumann and M. Roth, "First steps towards highly doped polyHIPEs", *Poster*, Target Fabrication Workshop 7 (2018), Darmstadt, Germany.

S. Sander, T. Ebert, M. Hesse, D. Hartnagel, M. Šmíd K. Falk, T. Abel, G. Schaumann, and M. Roth, "Enhancement of laser-driven, cold X-ray sources through front side modification", *Talk*, PHEDM Workshop (2020), Hirschegg, Austria.

S. Sander, T. Ebert, M. Hesse, D. Hartnagel, M. Šmíd K. Falk, T. Abel, G. Schaumann, and M. Roth, "Conversion efficiencies and source sizes for double-layered X-ray backlighter targets with front side modification", *Talk*, PHEDM Workshop (2021), Hirschegg, Austria.